GENERATING AND DETERMINING CHIRAL STRUCTURES IN NON-CHIRAL SYSTEMS

DISSERTATION

zur Erlangung des Doktorgrades der Naturwissenschaften

vorgelegt beim Fachbereich Physik der
Johann Wolfgang Goethe-Universität in Frankfurt am Main von

DIMITRIOS TSITSONIS
aus Kavala

Frankfurt 2024 (D30)

vom Fachbereich Physik der
Johann Wolfgang Goethe-Universität als Dissertation angenommen.

Dekan:
Prof. Dr. Roger Erb

Gutachter:
Prof. Dr. Reinhard Dörner
Prof. Dr. Till Jahnke

Datum der Disputation: 04/04/2024

Wir wollen zum Himmel hinaufblicken und auf die Erde hinunter und die Gesetze der Schöpfung erlernen
HI. Gregor der Theologe
(Let us look up to the sky and down to the earth and understand the laws of creation)
(St. Gregory the Theologian)

Dedicated to my lovely parents, Alkiviadis & Ioanna.
Dedicated to Father Gregorios

CONTENTS

I Introduction

II Background

III Experiment

IV Results

V Summary

VI Appendix

Part I

INTRODUCTION

1

INTRODUCTION

Chirality is an important concept in many fields of science. Chiral objects exist on all length scales, from spiral galaxies down to elementary particles carrying spin. The word chiral is derived from the Greek word "kheir" for hand, indicating that chiral objects have broken mirror symmetry as our hands have. They exist in two forms, as left or right handed species which are mirror images of each other. Ancient artist and architects already created chiral artifacts and used chiral forms. The Greeks where among the first to explicitly refer to chirality laying the foundation for its understanding in later centuries.

Stereoisomers are molecules that possess the same molecular formula and bonded atom sequence but differ in their three-dimensional orientations. Among these stereoisomers, enantiomers stand out — a pair of mirror images that are non-superimposable by translation and rotation. Enantiomers, a specific type of stereoisomer, are of particular interest in this thesis. While enantiomers possess the same physical properties such as binding energy or rotational spectra, they exhibit different behaviours regarding the rotation of polarised light and their interactions with other optical isomers of different compounds. These differences can lead to significant variations in their biological effects [1]. Usually, the two enantiomers are called R and S enantiomer [2].

From the intricate structures of biological molecules like DNA and proteins to the complex interactions of pharmaceutical compounds, chirality unveils its influence in remarkable ways and is ubiquitous in various fields, including biology, medicine, anatomy, and human development. In biology, DNA is chiral, and the amino acids used to construct proteins occur predominantly in the S form. In medicine, chirality plays a crucial role as drugs often exist as enantiomeric pairs, with each enantiomer exhibiting different therapeutic effects. For example, dextropropoxyphene [3] is a painkiller, while its enantiomer, levopropoxyphene [4], serves as an anti-cough agent. Similarly, penicillamine's [5] S-enantiomer is used to treat primary chronic arthritis, whereas the mirror image enantiomer of the S, called R-enantiomer lacks therapeutic efficacy and is toxic.

Chirality influences various aspects in people's life. Apart from the examples mentioned above, it is notable in the field of fragrance, where enantiomers of compounds like limonene, which naturally occur, exhibit distinct smells. One enantiomer may smell like lemon, while its mirror image compound smells like oranges. Humans distinguish these chiral molecules through their nasal receptors. Chirality also plays a historical role in the discovery of Vitamin C, which has chiral properties.

A powerful tool to study molecular chirality is the interaction with the light. Here are three different effects are notably. Firstly, optical activity which is a rotation of the polarisation plane of light upon transmission through a chiral medium such as a solution of one enantiomer. This very weak effect is routinely used in chemistry. Secondly, the related effect of circular dichroism (CD) in absorption which that the absorption strength of a chiral medium depends on the helicity of the light. This effect relies on the magnetic part of the light matter interaction is typically of the order of $10e^{-4}$. More recently the much stronger effect of Photoelectron circular dichroism (PECD) has been discovered for single and multiphoton ionisation. This technique deals with the emission pattern of a photoelectron by measuring the energy and most importantly the angular distribution of the photoelectron, providing information about the chiral nature of the molecules. A couple of strong evidence using the aforementioned techniques of circular dichroism and photoelectron circular dichroism can be found in references [6, 7].

CD and PECD can determine only the handedness of an ensemble of many molecules. An even more powerful technique for chiral sensing is Coulomb explosion imaging (CEI). This technique allows to determine the handedness of a single molecule. In CEI the molecule is charged up by interaction with light or by stripping off its electrons in a thin fold. The repulsion between the charges then drives the molecule into fragmentation and from the measured three dimensional momentum vectors of the fragments, the handedness can be determined. To achieve this, at least four fragments are needed. In this thesis, CEI is induced by absorption of a single high energy photon which creates an inner-shell hole. The subsequent cascade of Auger decays then leads to multiple fragmentation.

Two different kinds of experiments were conducted. The first experiment focused on exciting electrons to different energy states, while the second experiment involved direct photoionisation to measure the angular distribution of photoelectrons in the molecular frame. Excitation refers to promoting an electron from a lower energy state to a higher energy state, which was accomplished by absorbing energy from an accelerator beam. Photoionisation occurs when a molecule absorbs photons with sufficient energy to surpass its ionisation potential, resulting in the formation of positively charged ions. In this process, photons are absorbed, completely removing electrons from the molecule and leading to ion formation.

The primary question addressed in this thesis is whether a chiral signal can be detected from a purely achiral planar molecule with no chiral centre and a planar structure using an accelerator as a photon source. The results of the initial experiments prompted further exploration of applying these processes to other molecules. Two molecules were chosen for implementation: a simple diatomic molecule like oxygen and a more complex polyatomic molecule like isopropanol.

Part II

BACKGROUND

2

CHIRALITY

The initial question is what chirality is and how we can perceive this physical phenomenon as human beings. Handedness is an individual's preferential use of one hand, known as the dominant hand, in terms of strength, speed or in a general way ability. By definition, the other hand is weaker and less subjectively preferred and it is called non-dominant hand. Obviously, right-handedness is by far more common, closed to 90% in the population. However, due to genetics and biological reasons, we observe small percentage of the population which is left-hand dominant. In addition to that, we meet people with mixed-handedness mixed-handedness (<1% of the world population), who change their hand-preference between different tasks, and ambidextrous people, who are equally abled with both hands (about 1% of the world population).

In chemistry, a molecule or ion is called chiral if it cannot be super-disposed on its mirror image by any combination of rotations, translations and some conformational changes. A chiral molecule or ion exists in two stereoisomers that are mirror images of each other, called enantiomers; they are often distinguished by their absolute configuration or via the process of the circular dichroism of a photoelectron (PECD), which results in an asymmetry in the photoelectron angular distribution, which is a signature of chiral molecules, as either right- or left-handed. The absolute configuration refers to the spatial arrangement of the atoms within a chiral molecule. It is typically relevant in organic chemistry, in which the carbon is the centred atom and is connected with four other substituents. On the one hand, from the perspective of chemistry, the two enantiomers of a molecule have the same properties except for the interaction with other chiral substances. On the other hand, from the perspective of physics, both have the same physical properties, except for the optical activities, such as circular dichroism (CD) or photoelectron circular dichroism (PECD) described in the section 2.1. A sketch of the two enantiomers of a chiral molecule is given in the next Fig. 2.1 .

Chiral molecules will usually have a stereogenic element from which chirality arises. The most common type of stereogenic element is a stereogenic centre, or stereocenter. In the case of organic compounds, stereocenters most frequently take the form of a carbon atom with four distinct groups attached to it in a tetrahedral geometry. The phenomenon of optical activity or optical rotation arises because of the tetrahedral geometry with the carbon as the stereocenter. Optical rotation is the rotation of the orientation of the plane of polarisation about the optical axis of linearly polarised light as

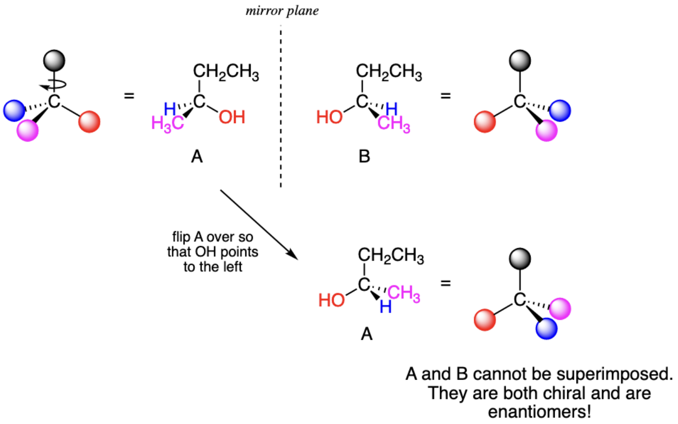

Figure 2.1: Two Enantiomers of a chiral molecule [9].

it travels through certain materials. Optical activity is a phenomenon that occurs only in chiral materials, those lacking microscopic mirror symmetry. It is already observed in several kinds of chiral molecules among liquids or gases like sugars and also chiral liquid crystals, i.e. a state of matter with properties between those of conventional liquids and solid crystals, flow like liquid but its molecules may be oriented in a crystal-like way [10]. Substantially, it is the ability of the molecules to rotate the plane of plane-polarised light as it passes through a sample. When plane-polarised light passes through a sample containing chiral molecules, the molecules interact with the light and cause it to rotate. The direction and the degree of rotation depends on the molecular structure of the chiral molecules. In that particular case with the chiral molecules, the enantiomers will rotate plane-polarised light in opposite directions but by the same degree. The optical activity, as shown in the next figure, is measured using a polarimeter, an instrument that detects the angle by which plane-polarised light is rotated by a chiral substance [11, 12]. The whole process of optical activity is presented further starting with unpolarised light, in the following figure 2.2.

Unpolarised light (1) and (2) in Fig. 2.2 becomes linearly polarised (4) by passing through a polarisation filter (3), as shown in Fig. 2.2. The polarised light passes through a polarimeter tube (5) in Fig. 2.2 containing optically active molecular compounds (6) in Fig. 2.2. Depending on the length of the tube and the density of compounds within it, the polarisation axis of the light rotates. The rotation is measured by an analyser unit (7) in Fig. 2.2. Switching enantiomers [13] in the polarimeter tube results in the change of rotation direction of the light's polarisation. For example, the R enantiomer is located at a specific angle clockwise and the S enantiomer anti-clockwise, or vice versa. The angle is called observer rotation, and the chiral molecules are optically active [14].

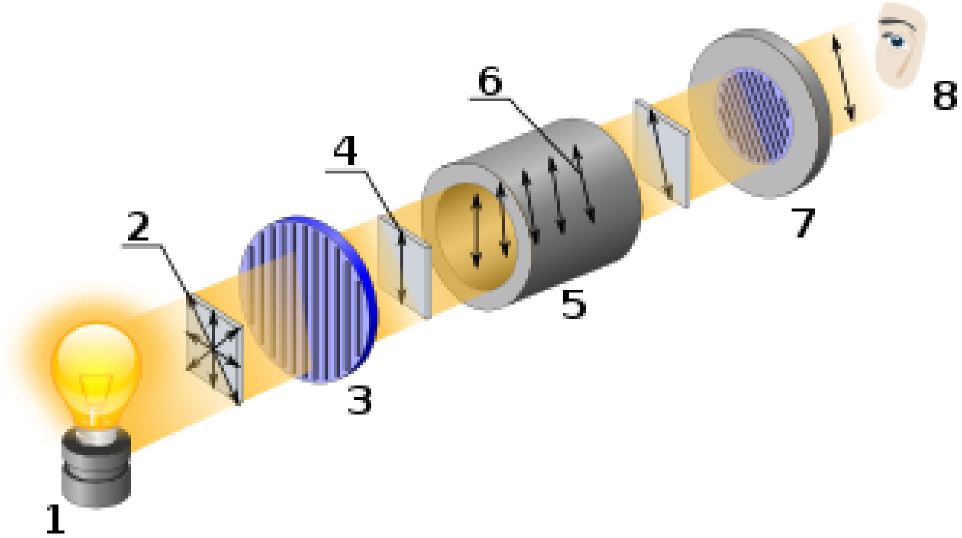

Figure 2.2: Sketch of an Optical Activity experiment [11].

2.1 CIRCULAR DICHROISM

In optics, a dichroic material is either one which causes visible light to be split up into distinct beams of different wavelengths or one in which light rays having different polarisations are absorbed by different amounts. As a continuation of that optical effect, cicular dichroism (CD) refers to a difference in absorption of left-hand circularly polarised (LCP) and right-hand circularly polarised (RCP) light [15, 16].

Since LCP and RCP photons have different spin angular momentum, CD is also referred to as a dichroism in spin angular momentum [17]. CD is used to give information about the chirality or handedness of molecular systems and is defined as $CD = A_{LCP} - A_{RCP}$, with A_{LCP} and A_{RCP} being the absorption coefficient of LCP and RCP light, respectively.

In general, the electromagnetic radiation consists of oscillating electric and magnetic fields perpendicular to the direction of propagation [18]. Linearly polarised light refers to an electric field that oscillates along a single axis. Circularly polarised light refers to an electric field that rotates around the light's propagation axis with a constant magnitude, that is, as the radiation propagates, the electric field vector executes a helical movement. Depending on the rotation direction, one refers to the radiation's polarisation as RCP or LCP [19]. The major difference between these two categories, is that the first the direction of the vector stays constant and the magnitude changes while for the latter the direction of the electric field vector changes and the magnitude changes.

Circular polarised light can be absorbed by a medium, leading to a unique optical activity for chiral objects. That means that an optical active chiral compound will absorb different amounts of LCP or RCP light [20]. In the scope of the present work, we focused on the Photoelectron Circular Dichroism (PECD).

2.2 PHOTOELECTRON CIRCULAR DICHROISM

The advent of second and third synchrotron radiation generators made high brilliance, high flux, highly monochromatic, and partially coherent X-ray photons available to a broader scientific community [21, 22]. The energy tenability of synchrotron radiation enables excitation and ionisation of molecules or atoms. It enables to target specifically, for instance, core-shell ale trans of atoms or molecules. PECD manifests itself as a forward/backward asymmetry of the photoelectron angular emission distribution with respect to the light propagation direction. It is observed when two chiral objects interact, which in our case is the interaction of circularly polarised photons with chiral molecules. The forward/backward asymmetry reverses when either the light's helicity or the molecule's handedness are switched [7]. At the beginning, B. Ritchie in 1976 [23] and N. A. Cherenkov in 1982 [24] established the PECD in dipole approximation, within a theoretical framework. Later, B. Ritchie [25] improved the theoretical description by including the magnetic/electric dipole (E1M1) and the electric dipole/electric quadrupole (E1E2) terms. According to the following descriptions, the PECD exhibits properties that make it a viable observable for a method that seeks to determine the absolute configuration of chiral molecules directly.

The PECD is a universal effect [26] that reveals the inherent chirality of the target in all ionisation regimes. It has been studied for one-photon [27] and multi-photon [28, 29] photoionisation, above threshold ionisation [30], and tunnel ionisation [26]. The majority of them were performed on valence electrons of randomly oriented molecules [31–34]. The different mechanisms of ionisation enable investigation of electronic and vibrational levels. Furthermore, a link between PECD and a fragmentation channel in strong field ionisation can also observed with the molecule of methyloxirane (MOX), by effectively selection of oriented non isotropic subsamples of molecules, as shown in the publication [35]. PECD has a strong sensitivity to electronic structure [36, 37], vibrational excitation [38] and conformation [39–41], clustering [42] and the energy of the outgoing photoelectron [37], using different light sources. Further, the high sensitivity of PECD made it also possible to study ultra-fast molecular dynamics, in particular time-resolved studies [43]. Combining the above-mentioned with more traditional chiroptical techniques, racemic mixtures can be resolved in real-time with the use of PECD, accessing their enantiomeric content [44]. Incidentally, only a few experiments have been conducted using core ionisation, for example, the pioneering study of V. Ulrich et al. [45].

2.3 ABSOLUTE CONFIGURATION OF POLYATOMIC MOLECULES

M. Pitzer et. al. [46] were first to directly measure (i.e. without reliance theoretical modelling) the absolute configuration of the chiral molecule bromochlorofluoromethane (CHBrClF) using Coulomb Explosion Imaging (CEI).

CHBrClF has carbon in the centre with four atomic substituents (H, Br, Cl, and F) in a tetrahedral arrangement. Using a COLTRIMS apparatus (extensively described in a following chapter), it was possible to resolve a racemic mixture of CHBrClF and assigning the absolute configuration (i.e., handedness) of each ionised molecule. Fig. 2.3 presents the complete breakup channel, where all ionic fragments are measured, for both enantiomers. Enantiomers are typically discriminated by $cos\theta$, defined as 2.1.

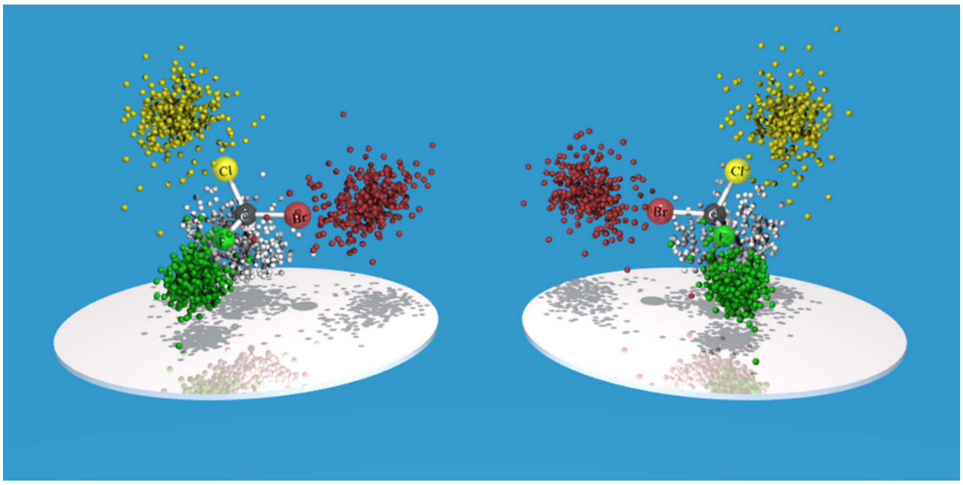

Figure 2.3: Linear momenta in five-fold fragmentation of both $CHBrClF$ enantiomers. Left: the measured momenta for $S - CHBrClF$ restricted to $cos\theta < -0.6$. Right the momenta of R-CHBrClF restricted to $cos\theta > 0.6$. In both images, the atoms are colour-coded as grey (C), white (H), green (F), yellow (Cl), and red (Br). Molecular Frame defined by the momentum of C atom and the momentum sum of the Br and Cl atoms, and the momenta projected in the molecular frame. H-atom momenta are expanded by a factor 2. The central C atom is also accelerated away from the centre of mass and ejected in the same direction as H.[46]

$$cos\theta = \boldsymbol{p_F} \cdot (\boldsymbol{p_{Cl}} \times \boldsymbol{p_{Br}})/(|\boldsymbol{p_F}| \cdot |\boldsymbol{p_{Cl}} \times \boldsymbol{p_{Br}}|) \tag{2.1}$$

With only four charged fragments or a mixture of three charged fragments and a neutral fragment, the approach could detect the spatial orientation of the molecule (momentum conservation). Due to the fact that the multi particle coincidence count rate is proportional to the single particle detection efficiency to the power of the number of detected particles, the latter could significantly increase the experimental yield as the detection efficiency declines with the growing number of fragments. The initial generation of high-charge states, the sharp decline in detection efficiency for the coincident detection of many particles, and uncertainties in the assignment of the various molecular fragments are among the difficulties when using pure CEI techniques to obtain structural information of larger molecules.

Part III

EXPERIMENT

3

OVERVIEW OF THE EXPERIMENTAL SETUP

As previously discussed in chapter 2.3, measuring the momenta of all ionic fragments of a photoreaction, one can determine the absolute configuration of a molecule. Indeed, in an ideal case where one measures the complete kinematics of a reaction (that is, all nuclear fragments and all electrons), one gains access to the full information of the system. For small molecular systems, this can be achieved using Cold Target Recoil Ion Momentum Spectroscopy (COLTRIMS) [47], which makes it a powerful technique to investigate atomic and molecular reactions.

In this chapter, we will provide all the necessary information regarding the methods and the critical components of the experimental setup for the purpose of scientific research that ensure reliable and reproducible results. Our aim is to present a detailed overview of the experimental procedures to provide a clear understanding of the research process, based on the performed experiments.

This chapter includes an overview of the COLTRIMS technique 3.1, as well as more detailed sections of the components involved in the experiment, as presented from 3.2 to 3.6.

3.1 COLD TARGET RECOIL ION MOMENTUM SPECTROSCOPY

Firstly, before the actual experiment, the necessary preparations must be made, including the preparation and testing of the experimental equipment. At the beginning, the preparation of the supersonic gas jet. The spectrometer and the detector-setup for the experiment are built. After that, several calibration measurements are performed to ensure the accuracy and functionality of the equipment.

The basic principles of the technique are the following as shown in figure 3.1. At its core, the COLTRIMS setup is a sophisticated apparatus designed to investigate the momenta and kinetic energies of charged particles, such as electrons and ions, emerging from atomic and molecular interactions. This technique has revolutionised the field of ion spectroscopy and has become an indispensable tool for studying photoionisation [48, 49], electron dynamics [50], and molecular fragmentation [51] processes with unprecedented precision and detail. Central to the COLTRIMS setup is a highly advanced spectrometer. The spectrometer employs ingenious principles of momentum imaging to measure the positions-of-impact of charged particles, providing the ability to reconstruct the momenta of the particles. Based on that, the spectrometer enables the observation of reaction dynamics with exceptional accuracy. The particles are captured by the two meticulously designed detectors. These detectors, strategically placed within the spectrometer, are calibrated to capture the charged particles within exceptional efficiency and sensitivity. They are shown in figure 3.1.

The charged ion(s) and electron(s) resulting from the interaction of the light with atoms or molecules are projected onto the respective detectors by electric and magnetic fields, as is depicted by the lines in Fig. 3.1. The spectrometer is housed in the reaction chamber. It is under ultra-high vacuum which ensures that no secondary collisions influence the trajectory of the charged particles and that the signal-to-background ration is sufficient. As a charged particle traverses within the spectrometer, it interacts with electric and magnetic fields, leaving its unique imprint onto the detectors. These signals, in the form of electronic pulses, carry valuable information about the particle's momentum, energy, and arrival time.

The COLTRIMS instrument is capable of measuring groups of those particles in coincidence. The copper plates of the spectrometer, indicated as the golden rings in Fig. 3.1, are responsible for the electric field. Large Helmholtz coils mounted around the reaction chamber (large brown circles in Fig. 3.1) are responsible for the production of the magnetic field.

The signals of the detectors are digitised and fed into a computer for on- and off-line analysis.

During the experiment, the experimental setup is carefully arranged according to the experimental design. This includes the alignment of beamlines, the placement of detectors and targets, and the configuration of data acquisition systems. In addition, safety protocols must be followed to ensure the protection of the experimenters and the equipment. More details about COLTRIMS reaction microscopes can be found in Reference [52].

The COLTRIMS instrument as part of the synchrotron source Petra III at DESY, Hamburg, Germany presented in figure 3.2. In this picture, an internal section of the main chamber is shown, which internally rests the spectrometer with the detectors. At the top of the image in figure 3.2, one of the two detectors is presented, including the anode holder (top), the delay-line anode (middle) and the micro channel plates (MCP) (bottom). After that, the brown metal surfaces are the copper plates, which are the vital part of the generation of the electric field. At the top of the main chamber, the LAN cables are located which transmit the electronic signal to the computer for further process through the data acquisition system (DAQ).

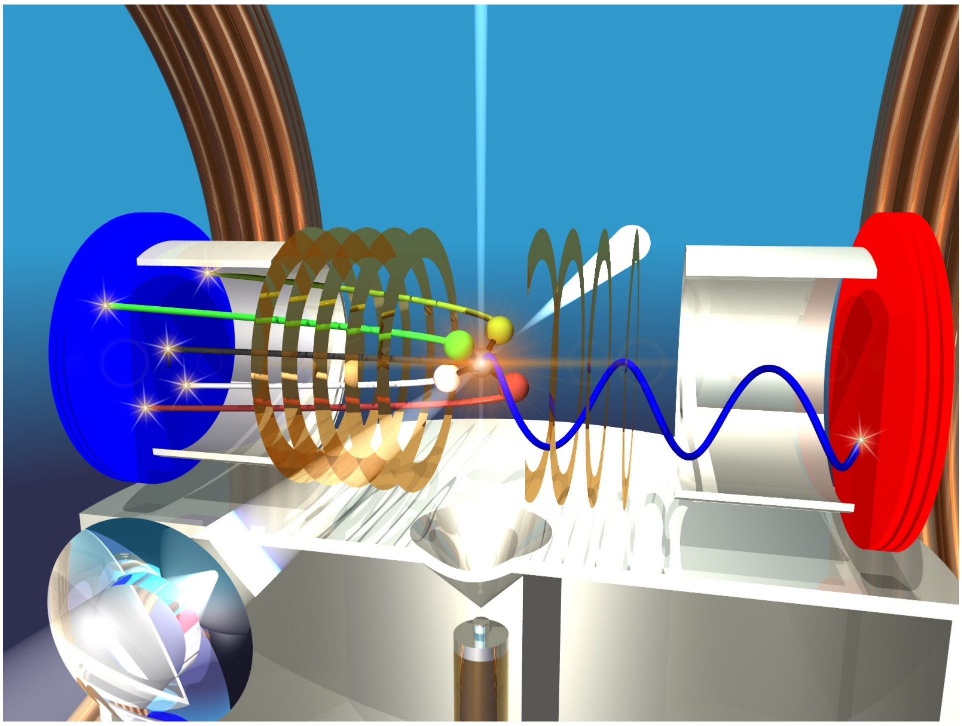

Figure 3.1: Concept of a COLTRIMS spectrometer. The blue and red circles are the ion and electron detectors, respectively. The thin line starting at the bottom of the figure and going towards is the supersonic gas jet. The small brown circles in the centre of the top figure are the copper plates, creating the electric field. The part of the large brown circles visible at the top edges of the figure are the Helmholtz coils, responsible for the creation of a magnetic field. The blue curved line towards the electron detector is the trajectory of an electron. The straight yellow, green, red and white lines towards the ion detector are the trajectories of ions.

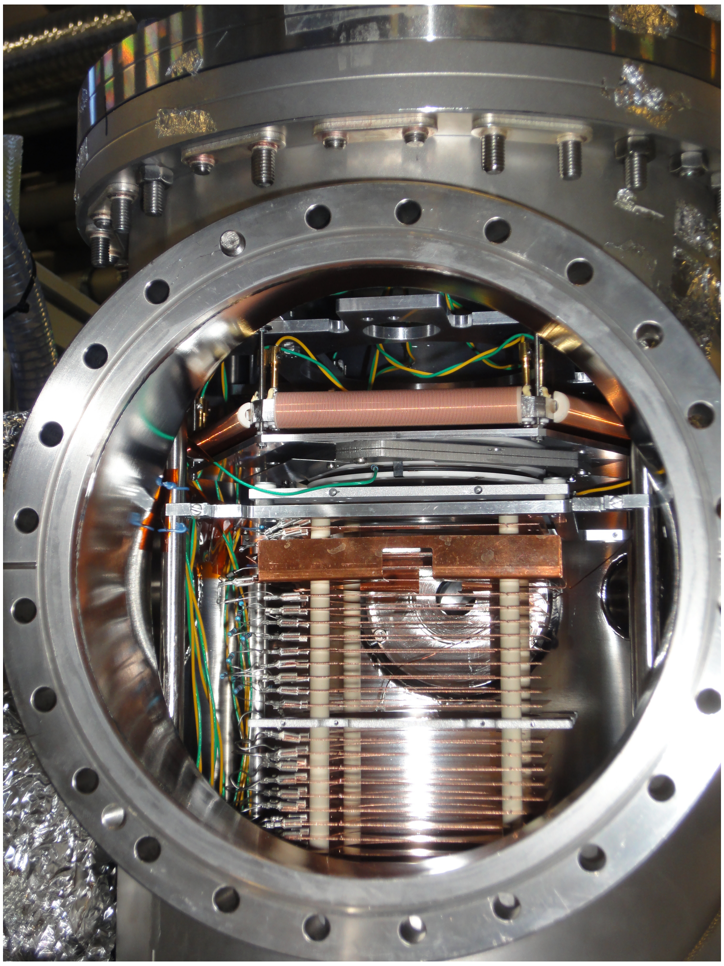

Figure 3.2: A section of the main chamber of a COLTRIMS setup.

3.2 PHOTON SOURCE

As already mentioned, synchrotron radiation is a form of electromagnetic radiation emitted by the acceleration of charged particles like electrons, protons, etc. In the cases related to this thesis, the radiation is produced by fast electrons moving through magnetic fields, which are created by strong magnets in the region of $5T$. Based on Maxwell's equations, an accelerated charged particle always emits electromagnetic radiation.

Synchrotron radiation is created in so-called wigglers or undulators, where a series of alternating magnetic fields force electrons onto undulating trajectories. At each turning point of the electrons' trajectories, synchrotron radiation is emitted. For electrons traveling with highly relativistic speeds through the undulators or wiggles, the emitted synchrotron radiation points along the longitudinal direction of the motion. The power carried by the radiation is found by the relativistic Larmor formula 3.1 [53].

$$P_\gamma = \frac{1}{6\pi\epsilon_0}\frac{q^2a^2}{c^3}\gamma^4 \tag{3.1}$$

where ϵ_0 is the vacuum permittivity, q is the particle's charge, a is the magnitude of the acceleration, c is the speed of light, and γ is the Lorentz factor.

Most of the experiments in this thesis have been performed at the beamline $P04$ [54] of the synchrotron light source PETRA III at DESY in Hamburg, Germany. The photon source used in the experimental hall of PETRA III consists of an electron storage ring of 2.3 km circumference and an electron linear accelerator (LINAC), which can produce high-energy electrons that are then sent through a series of undulators. As has already been described, synchrotron radiation can be produced by orbiting high-energy electrons, traveling close to the speed of light. At the PETRA III experiment, the light arrives at short pulses, repeating – depending on the fill pattern of the storage ring – every 8 ns (corresponding to 960 electron bunches in the storage ring) up to every 192 ns (40 electron bunches). The COLTRIMS setup is using the latter, i.e. 40 bunches. The 40 bunches are distributed equally along the circumference of the accelerator.

At beam line P04 of the PETRA III storage ring, a specific type of undulator called APPLE-2 is used, which is capable of producing an extremely high flux of X-ray photons, namely up to 10^{12} photons per second. The range of photon energy is between 200 and 3000 eV, for different polarisation properties. The APPLE-2 undulator operates using only the first harmonic of the undulator, which simplifies the experimental setup and enhances the coherence of the X-ray beam [55].

3.3 TARGET PREPARATION SYSTEM

Supersonic jets are often used to study the properties of gas-phase molecules and their interactions with other particles. A supersonic jet is a high-velocity gas stream that is created by expanding a gas through a small nozzle. Afterwards, the thin jet is directed towards a vacuum chamber by the usage of a specific cone-shaped aperture called a skimmer. A more detailed description of this target preparation procedure can be found in Reference [56]. The creation of a supersonic jet demands a precise gas handling system consisting of gas cylinders, pressure regulators, and valves that allow for precise control of the gas flow and pressure. The most important part of the whole system is the nozzle because it is responsible for expanding the gas and creating the supersonic jet. The diameter of the nozzle varies in all the experiments and tests of various diameters are performed before the beam-time. The diameter of the nozzle of all the following experiments in this thesis was 0.2 mm. Reference [57] provides a graphic representation of the system's geometry.

3.4 SPECTROMETER

One of the main parts of the COLTRIMS setup is the spectrometer, located inside the main chamber, as shown in figure 3.3. A position- and time-sensitive detector is placed at each end of the spectrometer, respectively, to detect the reaction ions and electrons. At the intersection volume of the light beam and the supersonic jet, reaction electrons and ions are produced. The produced charged particles are directed towards to the two detectors by electric and magnetic fields. In this thesis, with proper electric and magnetic field, we were able to capture ions, energy of a few eV and a detection of solid angle of 4π. We were also able to detect the full solid angle of emitted electrons with an energy up to 600 eV.

The electric field is generated by thin copper plates. The plates have a rectangular shape with a circular cutout in the centre. They are subsequently connected by resistors. Thus, by applying a constant voltage at each end of the spectrometer, a homogeneous electric field is generated inside the spectrometer. Achieving high resolution imaging is crucial for the purposes of this thesis. That leads to use of electrostatic lenses to achieve a focusing effect. By applying a different voltage drop due to different resistance between two copper plates, an inhomogeneous electric field is created. The electric field distribution within the lens is designed to converge the particle trajectories.

The magnetic field is created by Helmholtz pair coils, mounted outside of the main chamber, which creates a homogeneous magnetic field. The effect of the magnetic field on the ions is neglectable in comparison with the

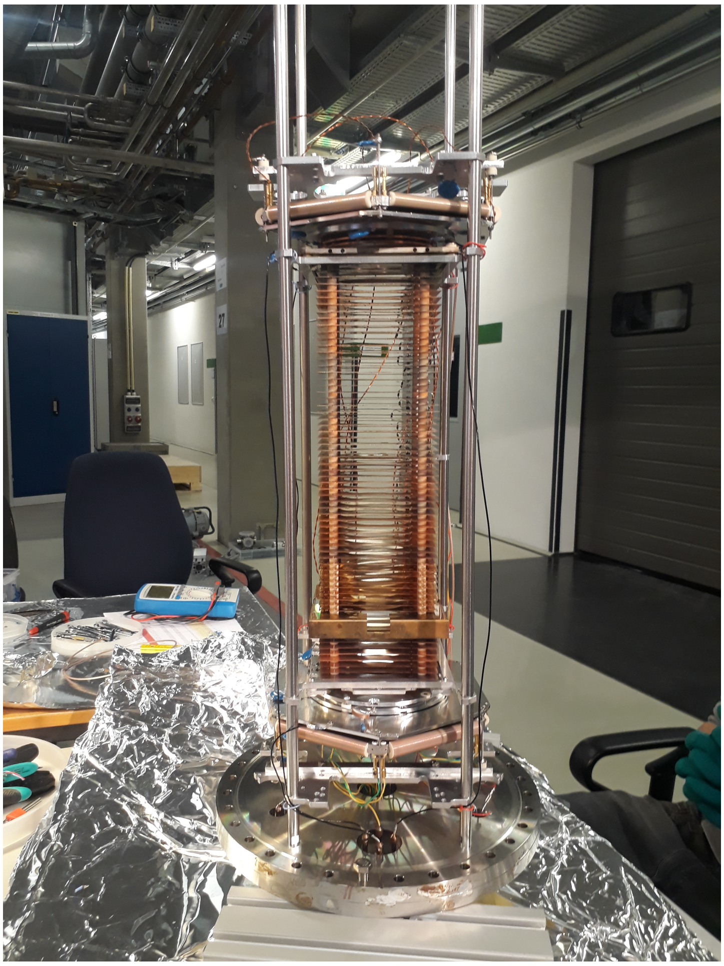

Figure 3.3: Overview of the spectrometer of cold target recoil ion momentum spectroscopy (COLTRIMS) instrument.

electrons, which interact with the magnetic field due to their lower mass. The magnetic field plays a crucial role in a typical COLTRIMS experiment by guiding electrons onto a gyrating trajectory. This allows for the detection of high-energy electrons with a large momentum perpendicular to the detection plane, which would otherwise not be captured on the finite detection surface. However, the gyrating trajectory eventually brings the electrons back to the spectrometer's centre axis where they originated from.

Increasing the magnetic field leads to a shortened gyration period and consequently leads to increase of the uncertainty in momentum close to infinite. For this thesis, electrons were contained within one gyration period. That means that there is also a limit of the maximum detectable electron energy with the COLTRIMS setup. In the scope of this thesis, three different strengths of magnetic fields are utilised. The exact values of the fields, used in the several runs of the experiments, are presented in the next chapter.

The two detectors define the two regions of the spectrometer, the so-called ion arm and electron arm, respectively. For the spectrometers employed in the experiments of this thesis, the ion arm was further split into an acceleration and a drift region. The latter is a region without an electric field resulting in a no-acceleration region. For an appropriately chosen length-ratio of acceleration and drift regions (namely, 2:1 [58]), the finite size of the reaction region is focused, resulting in equal times-of-flight for particles originating from different points within the reaction region along the time-of-flight direction.

3.5 DETECTORS

The endpoints of the electron and ion arms at the spectrometer are the detectors. An example of the COLTRIMS detector presented in figure 3.4. The detectors capture the electrons and ions after the interaction and estimates the time- and position- of their impact of them. This is the information that takes place in the calculation of the three-dimensional vector momentum of every particle. The detectors consist of two parts: the first part is the microchannel plate (MCP) and the second part is a three-layer delay line anode (DLA).

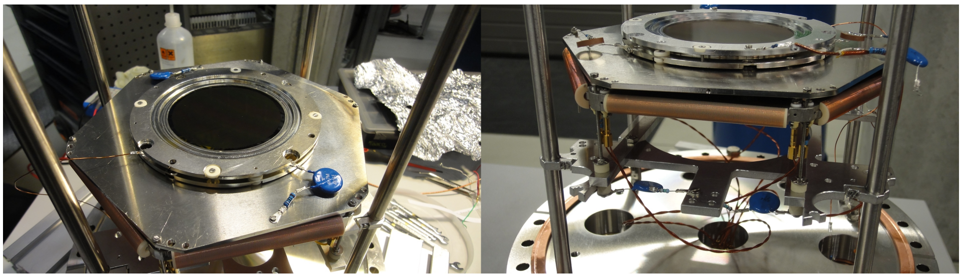

Figure 3.4: Overview of MCP attached to delay-line anode detectors of the COLTRIMS instrument.

MCPs are thin discs of a few centimetres in diameter and their thickness is around 1 mm. The MCP has a metal coating on its front and back surfaces that serve as input and output electrodes, while the inside of it uses a semiconducting layer that can emit secondary electrons when primary energetic particles like electrons bombard it. An MCP is a type of particle detector that can detect multiple particles within a short period of time. MCP is responsible for capturing and measuring the spatial and timing information of each particle [59]. In practice, two MCPs are stacked in a so-called Chevron configuration to increase the signal amplification even further [60].

The three-layer delay-line anode detectors (DLA) are a type of particle detector that is used to measure the positions-of-impact of particles that pass through them. TOF is calculated from the MCP signal. The signal continues

from the MCP and hits the DLA. The DLA used for this work consisted of three layers of wire, enclosing an angle of 60 degrees, respectively. This configuration is also called Hexanode [61]. The signal hits each wire at a specific point and travels to the ends of each wire. From the arrival times of the signal at each end of the layers, the position-of-impact along the direction of the anode wire can be detected. By recording the signals of at least two layers, one can determine the position-of-impact on the detector. The redundancy of the third layer improves the multi-hit capabilities of the Hexanode detector [59].
The detectors for all the experiments in this thesis are the same with a diameter of 80 mm [62].

3.6 SIGNAL PROCESSING AND RAW DATA ACQUISITION

The signals, one from the MCP and six from the Hexanode detector, are analog signals and thus, vary in height as a function of time. The analog signals are processed in such a way to eliminate this dependence and extract pure timing information. In order for this to be achieved and a bipolar signal to be produced, a Constant Fraction Discriminator circuit (CFD) is used. A representation of the whole process in the CFD circuits presented in figure 3.5. The CFD accepts a unipolar input signal and splits it into two parts via a resistor-divider. The first part is inverted and the second part is delayed and finally, both parts are superimposed to form the bipolar signal. The resistor divider is responsible for the ratio of the pulse height of the initial signal to the pulse height of the inverted signal. The signal is not in its final form since the Data Acquisition System (DAQ) of the computers needs to be fed by a digital signal. For that purpose, the signal is fed into a computer using Time-to-Digital Converter cards, which converts a time interval into a digital representation with high precision that can be further processed by the DAQ of the computers. For this thesis, the computer program COBOLD [63] was used as DAQ. It saves the acquired data as list-mode-files (lmf). These are processed further by the software package lmf2root, develop by A. Czasch and T. Jahnke [64].

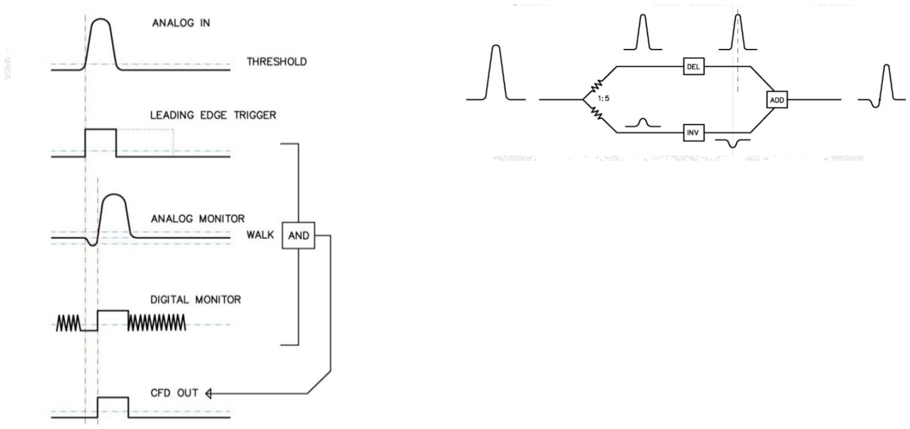

Figure 3.5: Overview of the CFD digital chain (left view) and overview of CFD analogue chain (right view) of the COLTRIMS instrument.

4

EXPERIMENTAL SESSIONS

The raw data sets used for the following thesis were recorded in four sessions at beamline P04 at DESY. The experimental parameters of each session are tuned for the particular experimental goal. The appropriate photon energy for the experimental runs were determined in commissioning runs. The section below offers an overview of the goals of each session, the different spectrometer settings and designs, and the experimental parameters for each run that are relevant to reproduce the raw data.

4.1 SESSION 1

The main research goal of this experimental session was to search for chirality effects at specific excited states. The chirality is observed solely through the fragmentation direction of the ions, removing the need to detect electrons. The ion arm of the spectrometer had a length of 17 cm. The electric field was fixed to 200 V/cm. The measurements are split into right- and left-handed polarised circular light. The idea was to explore effects related to chirality under the interaction of both polarisations of circular polarised light. For all the different photon energies, the calibration and the experimental parameters remained the same. The experiment targeted inner-shell ionisation as well as resonant Auger excitation. The latter was done by scanning the photon energy across the respective resonances.

- Formic acid and deuterated formic acid - November 2020
- Electron side: 12 cm and Ion side: 17 cm, B-Field: No, E-Field: 200 V/cm
- Using both helicity (left and right) of the light
- Run 1 - Formic acid scan C1s from 287.0 eV up to 291.6 eV
  - Calibration with N_2 with photon energy at 420 eV and at 428 eV
  - Calibration with Ar with photon energy at 247.4 eV, 248.4 eV, 248.7 eV, 249 eV, 250.4 eV, 252.4 eV, 256.4 eV, 260.4 eV, 266.4 eV
  - Scan around $\pi^*(C1s)$ resonance
  - Measurement in the whole range of the scan of $\pi^*(C1s)$
  - Manual scan around $3s/\sigma^*(C1s)$ and measured at 291.6 eV
  - Changing to DCOOH and measured only for the resonance at 287.9 eV

- Run 2 - Formic acid
  - Calibration with N_2 with photon energy at 420 eV
  - Calibration with Ar with photon energy at 247.4 eV, 248.4 eV, 250.4 eV, 252.4 eV, 255.4 eV, 258.4 eV, 263.4 eV, 273.4 eV and 288.4 eV
  - Photon Energy at 305.5eV -leading to 10 eV photoelectron
  - Scan around $\pi^*(O1s)$ resonance
  - Measurement at 531.7 eV and at 535.4 eV
  - Measurement at photon energy 317 eV corresponding to 21 eV above Ionisation potential (IP)

Further excited states of formic acid were investigated in a similar way in June 2021 in an effort to observe similar chiral effects in σ^* states as in the aforementioned for the π^* state in November 2020.

- Formic acid and deuterated formic acid - June 2021
- Electron side: 64 cm and Ion side: 11.9 cm[acceleration + lens(11.3 cm-11.9 cm)], 30.8 cm (drift), 0.7 cm (post)
- E-Field: 125 V/cm B-Field: 7.6 G
- Run 1 (DCOOH, HCOOH targeting $\pi^*(O1s)$, $\sigma^*(C1s)$, photoelectron at 15 eV)
- Calibration using CO (using the TOF of C,O for further online analysis)
- Scan for $\pi^*(O1s)$ from 530.0 to 535.0 eV
- Measurement of DCOOH at531 eV (π^*) and of HCOOH at 534 eV (σ^*)
- Scan for the $\sigma^*(C1s)$ of HCOOH and measured at 302.6 eV and 302.8 eV $(\sigma^*)(C = O)$
- Measurement at 296.8 eV (σ^*) and 296.4 eV and 297.2 eV $(C - OH)$

4.2 SESSION 2

The research goal of the following experiments was the electron interactions using a diatomic and a polyatomic molecule. This shifts the focus from ions to coincident electron detection. It was crucial to find the proper electric and magnetic fields to maximise the solid angle of the reaction electrons. At the same time, the electric field needed to be adjusted such that the different molecular breakup channels can be separated in the offline analysis.

This session was split into different experimental runs, because our goal was to compare our findings using data from different sources of light (such as free electron laser or synchrotron radiation) as well as differences in low-energy electrons and high-energy electrons, for both diatomic and polyatomic molecules.

- Isopropanol - August 2020
- Electron side: 17 cm and Ion side: 12 cm
- Using both left and right helicity of the light
    - Run 1 - Isopropanol 670 eV at 15 G
    - Calibration with N_2 at 420 eV
    - Calibration with Ar at 260 eV, 280 eV, 300 eV, 325 eV, 350 eV, 380 eV, 400 eV, 450 eV and 500 eV
    - Run 2 - Isopropanol in photon energies 670 eV, 600 eV, 563 eV, and O2 in photon energy 670 eV. Magnetic field at 40 G
    - Calibration with N_2 at 420 eV
    - Calibration with Ar at 260 eV, 280 eV, 300 eV, 325 eV, 350 eV, 380 eV, 400 eV, 450 eV, 500 eV and 600 eV
    - Run 3 - Isopropanol in photon energy 600 eV and magnetic field at 15 G
    - No calibration, same settings with Run 1

- Oxygen - April 2019
- Electron side: 64 cm and Ion side: 11.9 cm [acceleration + lens(11.3 cm-11.9 cm)], 30.8 cm (drift), 0.7 cm (post)
- E-Field: 50 V/cm, B-Field: 17,5 ns
    - Run 1 - Oxygen in photon energy 670 eV and 653 eV, B-Field: 17,5 ns
    - Run 2 - Oxygen in photon energy 638 eV and 573 eV, B-Field: 21,8 ns

5

DATA ANALYSIS

This part of the thesis describes the procedure of how to convert the raw data captured in list-mode (lmf) files (i.e., the timing information from the MCPs, the Anodes, and the bunchmarker) into 3D-momenta, from which all further physical observables are calculated. The first part includes the calculation of the time- and position-of-impact of every particle by using the raw data from the lmf files, the second the translation of times-of-flights and positions-of-impact into the three-dimensional vector momentum of every particle. A detector calibration is necessary before real momenta can be attained from the positions-of-impact. During this process, the detectors, the electric and magnetic field, the parameters of the spectrometer, and the calculated vector momenta of the particles are calibrated. All the before-mentioned steps are done in the software LMF2ROOT, which is based on the C++ programming language and the ROOT scientific software package.

5.1 TIMES-OF-FLIGHT AND POSITIONS-OF-IMPACT

The electron and ion detector each use a Hexanode detector with three layers, respectively. The signal travels in both directions of the wires. For each layer, named with the letters u, v, and w, the spatial information is encoded in the difference of arrival times at the wire ends, i.e. 5.1,

$$u = s_u \times (t_{u1} - t_{u2}) \quad v = s_v \times (t_{v1} - t_{v2}) \quad w = s_w \times (t_{w1} - t_{w2}) \tag{5.1}$$

where s_u, s_v and s_w are given in mm/ns. They represent the propagation speed of the signal perpendicular to the wire. The t_{u1}, t_{u2}, t_{v1}, t_{v2}, t_{w1}, and t_{w2} are the signal arriving times at the two ends of delay-line wire u, v, and w layer.

The x and y position in the laboratory frame are calculated by the arrival time of the u, v, and w layer. The laboratory frame is defined by the direction of the incident synchrotron light (x), the direction of the supersonic gas jet (y) and the principle axis of the spectrometer (z). The procedure includes a coordinate transformation based on the known geometry and orientation of the detector. The extra layer offers better stability and accuracy for the final calculation of the x and y coordinates [61].

The time-of-flight (TOF) of a particle is the time that passes between the moment of a reaction and the moment of the particle's impact on the detector. To achieve this, a reference signal that corresponds to the arrival time of a synchrotron-light bunch is necessary. Such a bunchmarker (BM) signal is provided by the synchrotron facility. As long as the spacing between two BM signals is constant and larger than the maximum electron time-of-flight TOF_e, TOF_e can be calculated via the equation 5.2 :

$$TOF_e = \mod (t_e - t_{BM}, T_{BM}) + \Delta t_{BM} \tag{5.2}$$

where t_e is the electron's recorded time-of-impact, t_{BM} is the arrival time of any one BM signal, T_{BM} is the time difference between two BM signals, and $\Delta\ t_{BM}$ is a global offset. $\mod$ is the modulo operator which returns the remainder of the division $t_e - t_{BM}$ by T_{BM}. $\Delta\ t_{BM}$ is a constant delay between t_{BM} and the actual instant of the reaction. $\Delta\ t_{BM}$ is determined experimentally.

Specifically, for the ions, on the other hand, the times of flight were much longer than T_{BM}. The significant point here is to ensure the calculation of the TOF of ions is performed in the same defined time window as the previous calculation regarding the electrons. That means that these calculations are implemented in every event where the corresponding electron and ions are detected simultaneously. The ion time of flight could be calculated as 5.3 :

$$TOF_i = t_i - t_e + TOF_e \tag{5.3}$$

5.2 PRESORTING

The raw data of a particle, that is, positions-of-impact and TOFs, do not provide direct insight into any physical observable, such as momenta, energies, emission angles, etc. From the raw data, positions-of-impact and times-of-flight are yielded by the procedure of transforming the information from the Hexanode system (u, v, w) to the laboratory frame (x, y). The gates for the ions are also applied during this procedure. This procedure is called presorting. The reason of the ion gates is to reduce all the unnecessary information of potential ions, which are not playing any role to our physics interests.

From the experimental parameters (such as, the length of the spectrometer, the electric (E) and magnetic (B) fields, as well as the particles' TOF and position-of-impact) one can calculate the full 3D-momentum vectors at reaction time. From these, all deduced physical quantities, such as kinetic energies, emission angles, etc, can be calculated. For all the different COLTRIMS setups in this thesis, the electric field was homogeneous. Then, the electron momenta are calculated using the following equations 5.4 and 5.5.

$$\begin{aligned} p_{x,e} &= m_e \times \frac{x \times b - a \times y}{a^2 + b^2} \\ p_{y,e} &= m_e \times \frac{-x \times a - b \times y}{a^2 + b^2} \\ p_{z,e} &= m_e \left(\frac{l}{TOF_e} - \frac{1}{2} \frac{eE}{m_e} \times TOF_e \right) \end{aligned} \tag{5.4}$$

$$\begin{aligned} a &= \frac{1 - cos\,(\omega \times TOF_e)}{\omega} \\ b &= \frac{sin\,(\omega \times TOF_e)}{\omega} \\ \omega &= \frac{q}{m \times B} \end{aligned} \tag{5.5}$$

m_e is the mass of the electron, l is the length of the acceleration region in the electron arm of the spectrometer, and TOF_e is the time-of-flight of the electrons.

In the case of the ions, the ions do not significantly interact with the magnetic field because of their large mass. All the experiments are performed with a homogeneous electric field E in the case of ions and only one acceleration region. That leads to the forward equations regarding the calculation of the $3D$ ion momenta, with the z component of the ion momentum calculated using the linear approximation 5.6.

$$\begin{aligned} p_{x,r} &= m_{ion} \times \frac{x}{TOF_{ion}} \\ p_{y,r} &= m_{ion} \times \frac{y}{TOF_{ion}} \\ p_{z,r} &= q_{ion} E \times (TOF_{ion} - TOF_0) \end{aligned} \tag{5.6}$$

TOF_{ion} is the time-of-flight of the ions, TOF_0 is the time-of-flight for ions with a momentum of $p_z = 0$ a.u., which, for all spectrometer settings of this thesis, equals the centre of the time-of-flight distribution. Equation 5.6 is only valid in the so-called linear approximation [65]. m_{ion} is the mass of the ion and q_{ion} its charge. x and y are position-of-impact. The electron(s) and the ion(s) are measured in coincidence.

In case of a molecular breakup into two fragments, the kinetic energy release (KER) is calculated via the equation 5.7.

$$KER = p_{rel}^2/2\mu \tag{5.7}$$

where $\mu = m_1 m_2/(m_1 + m_2)$ is the reduced mass and p_{rel} is the relative momentum, as shown in equation 5.8.

$$\vec{p}_{rel} = \vec{p}_1 - \vec{p}_0 \tag{5.8}$$

For calibration purposes, it is helpful to investigate so-called photoion-photoion coincidence (PIPICO) spectrum. There, the TOF of the first ionic fragment is plotted against the TOF of the second ionic fragment, as is shown, for instance, in Figure 5.1. Due to momentum conservation, the TOFs of ionic fragments resulting from one molecular breakup are correlated and visible as distinct features within a PIPICO spectrum. Data analysis involves identification of these features, consequentially identifying different fragmentation pathways of a particular molecular target. Based on this information, more focused subjects relating the behaviour of the ions and the correlation of the electrons can be processed further.

The PIPICO spectrum exposes correlations between particles from the same ionisation event, unlike a standard TOF spectrum. The lower part of a PIPICO spectrum is left vacant, as the TOF of the first ionic fragment is, as per definition, shorter than the TOF of the second ionic fragment.

Due to momentum conservation, a complete breakup channel (i.e., all molecular fragments were detected) is visible as a narrow line in a PIPICO spectrum. Opposingly, an incomplete breakup, where at least one molecular fragment is not detected, shows up as broad features in the PIPICO spectrum. Momentum conservation determines the lines' shape, with the ends corresponding to backward and forward emission with respect to the direction of the spectrometer's electric field. The Kinetic Energy Release (KER) of the breakup is inversely correlated with the length of the lines. The tilting phenomenon often reflects the mass-to-charge ratio of the fragment: A larger mass-to-charge ratio results in a larger deviation from the primary PIPICO diagonal line. A PIPICO example of our calibration data using the CO molecule is presented below in spectrum 5.1.

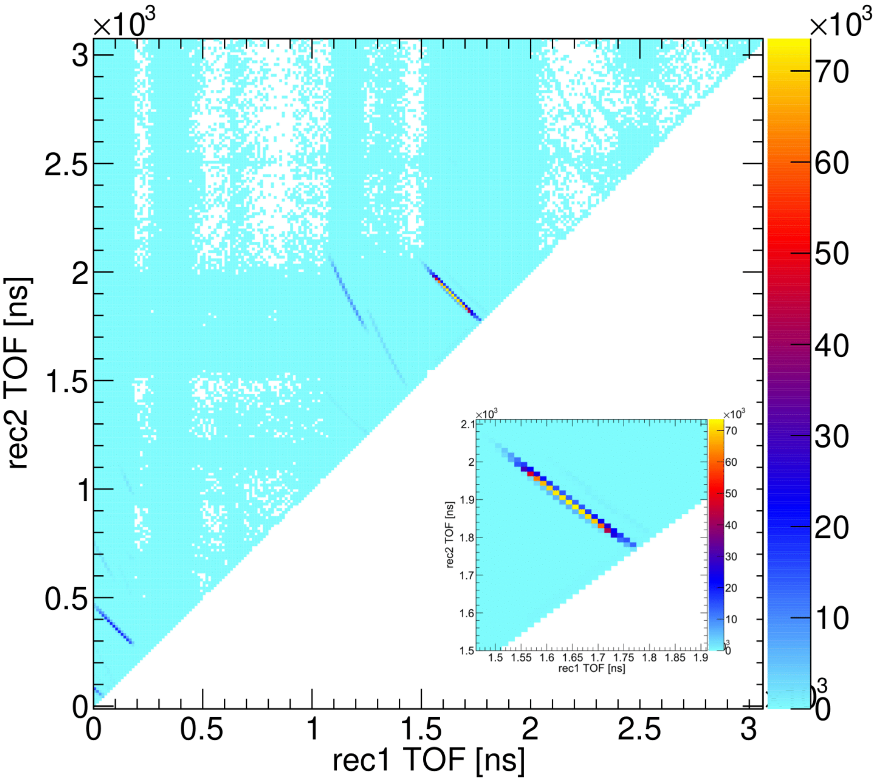

Figure 5.1: Pipico Spectrum of CO molecule. The insert spectrum is a zoom-in of the CO molecule to a breakup channel.

5.3 CALIBRATION

In the calibration step the exact values of the B-field, the E-field, the centre of the detectors, the time offset in equation 5.2, the relative rotation angle between the detectors, and a stretch parameter for the detectors, and the absolute values of the photoelectron and ion energies are inferred from the data.

The time delay is determined by extrapolating the constant term of a regression of the nodes of the electron gyration period T_g induced by a B-field. When no B-field is present, it is possible to retrieve the time delay either as the difference between the mean TOF of a measured electron and a simulated one or by looking at the TOF of photons.

In this analysis, three different molecules (CO, N_2, Ar) were used for the calibration of the data, each targeting different aspects of the overall experiment. The use of multiple calibration molecules is a common practice in

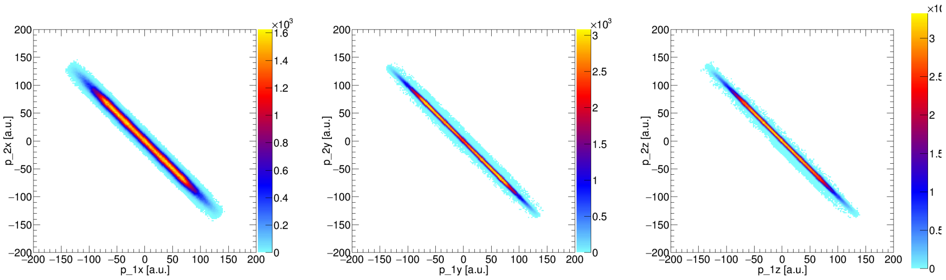

Figure 5.2: Sanity check of momentum conservation in $C^+ - O^+$ breakup channel. Left: horizontal axis is the momentum of the first ion in the x direction and the vertical axis is the momentum of the second ion in the x direction. Center: as left panel but for the y direction. Right: as center panel but for the z direction.

such kinds of experiments, as it allows for more accurate and precise characterisation of the experimental conditions. The calibration using the CO molecule was specifically aimed at defining the electric field, the ion arm, and the TOF of $C+$ and $O+$ under calibrating the experimental settings. This information was then used in the subsequent analysis of formic acid in the next chapter.

The calibration with CO was essential to ensure that the electric field, ion arm, and TOF were properly defined before analysing the formic acid sample. This ensured that any conclusions drawn from the analysis of formic acid were based on reliable and consistent data.

The second molecule used for the calibration was N_2. N_2 - a diatomic molecule - is the most throughly studied diatomic molecule and therefore, is well-suited to be used for detector calibration. To both calibrate the value of the E-field of the spectrometer and the relative orientation of the detector, the reaction $N_2 + e \rightarrow N^+ + N^+ + 2e$ is studied. The K-shell photoionisation of N_2 with a right circularly polarised photon of energy 420 eV produces a back-to-back fragmentation of two charged ion fragments. Every N atom has a mass of 14 atomic units. The PIPICO spectrum in figure 5.3 shows the expected breakup channel.

According to the linear approximation 5.2, the momentum calculated in TOF-direction is directly proportional to the TOF as shown in equation 5.6; therefore the E-field can be calibrated using the KER of the N_2 spectra. The KER spectrum of the latter molecule is shown in figure 5.4 and shows a sharp peak around $KER = 9$ eV that was used to scale the E-field to the final experimental value of $E = 48\ V/cm$.

The relative rotation angle between the electron and the ion detector can be deduced from molecular-frame photoelectron angular distributions (MF-

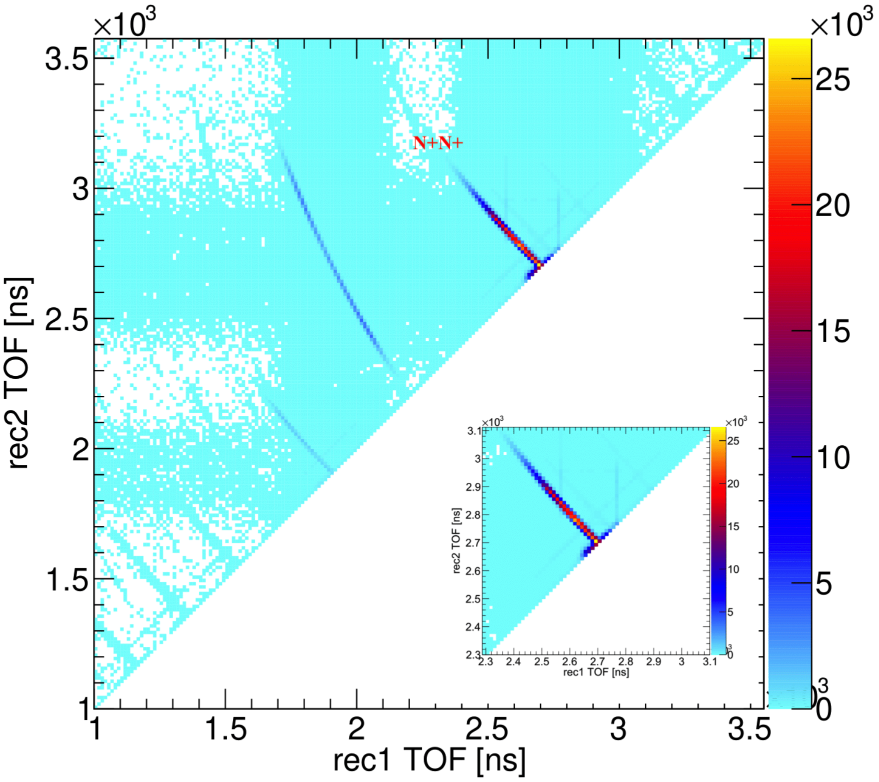

Figure 5.3: PIPICO spectrum of N^+N^+ ions from photoionisation of N_2 at a photon energy of $420eV$. The two narrow lines correspond to N^+N^+ and N^+N^{++} fragment coincidences accordingly itself.

PADs) of the $N^+ - N^+$ breakup channel. These MFPADs are well-known from literature (e.g., ref. [67, 68]) and are only obtained for a correct relative rotation angle. The MFPAD is obtained by transforming the electron momentum vectors from laboratory frame to the molecular frame and selecting molecules, whose orientation coincides with the polarisation plane. The molecular frame is defined as 5.9.

$$
\begin{aligned}
\hat{z} &= \vec{p}_{rel}/\|\vec{p}_{rel}\| \\
\hat{y} &= \vec{p}_{rel} \times \vec{\gamma}/(\|\vec{p}_{rel}\|\|\vec{\gamma}\|) \\
\hat{x} &= \hat{z} \times \hat{y}
\end{aligned}
\tag{5.9}
$$

Where $\vec{p}_{rel}$ is the difference of the two ion momentum vectors and $\vec{\gamma}$ is along the light's propagation direction (i.e., the x-direction of the laboratory frame).

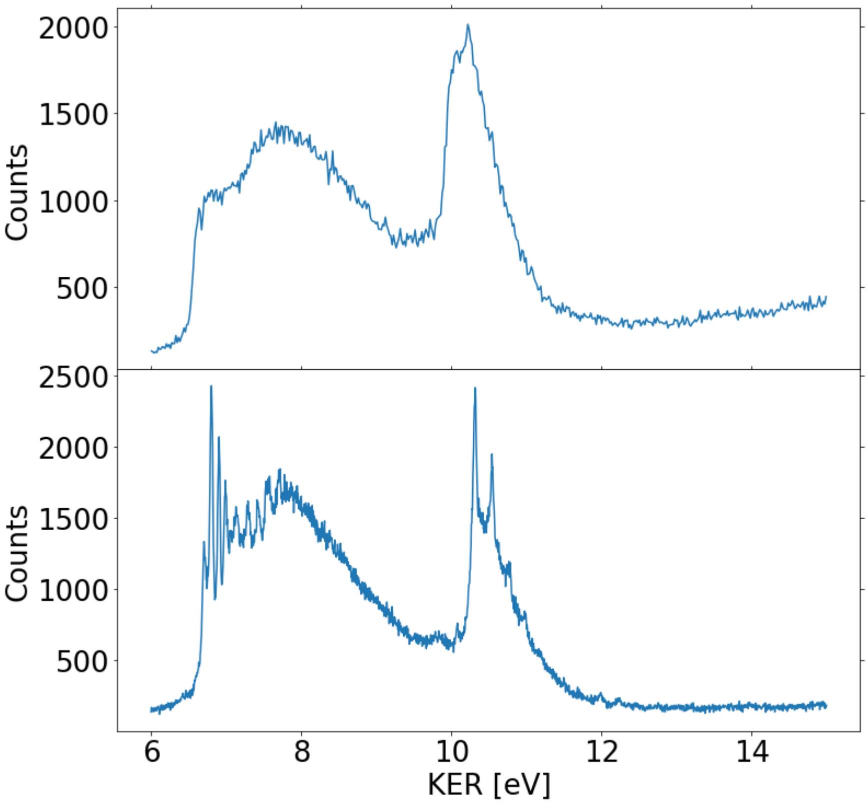

Figure 5.4: KER spectrum of N^+N^+ fragments of N_2 after K-shell ionisation at a photon energy of $420eV$. The upper plot refers to the data 4.2. The lower plot refers to the data from reference [66].

The molecular frame normalised vectors are used to project the electron momentum vectors $\vec{p_{el}}$ from the Laboratory Frame onto the Molecular Frame. The polar (θ) and azimuthal (ϕ) angles of a spherical coordinate system are defined as follows, as see in equation 5.10 :

$$\begin{aligned} \phi &= \arctan^2\left(\vec{p_{e,y}}, \vec{p_{e,x}}\right) \\ \theta &= \arccos\left(\frac{p_{e,z}}{\sqrt{p_{e,x} + p_{e,y} + p_{e,z}}}\right) \end{aligned} \tag{5.10}$$

The MFPAD of figure 5.5 and the polar MFPAD in figure 5.6 are obtained by calculating the spherical coordinates of $\vec{p_e}$ using equations 5.10. Two different magnetic fields of 13 and 42 Gauss have been used in this project.

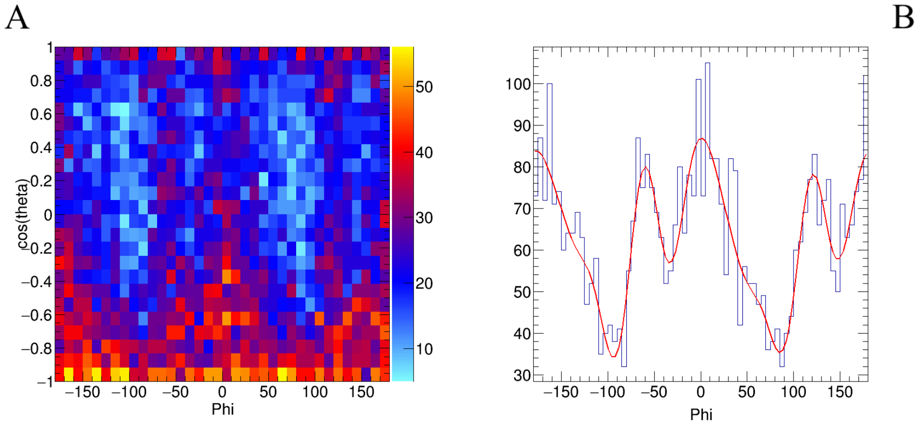

Figure 5.5: Single MFPAD restricted to the polarisation plane for N_2. Left (A): MFPAD in spherical coordinates defined by equation 5.10. Right (B): MFPAD integrated over the laboratory azimuthal angle ϕ; the red curve is a B-spline fit. The magnetic field is 42 Gauss.

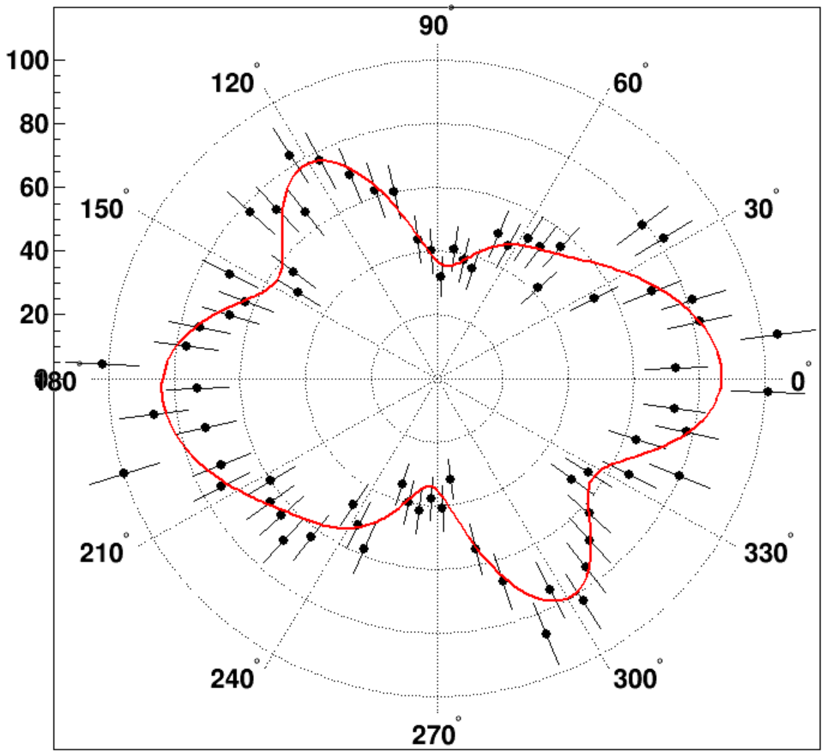

Figure 5.6: Polar representation of data (points) from Figure 5.5(B). Line: Fit using a sum of spherical harmonics up to l=4. The error bars represent the standard statistical error.

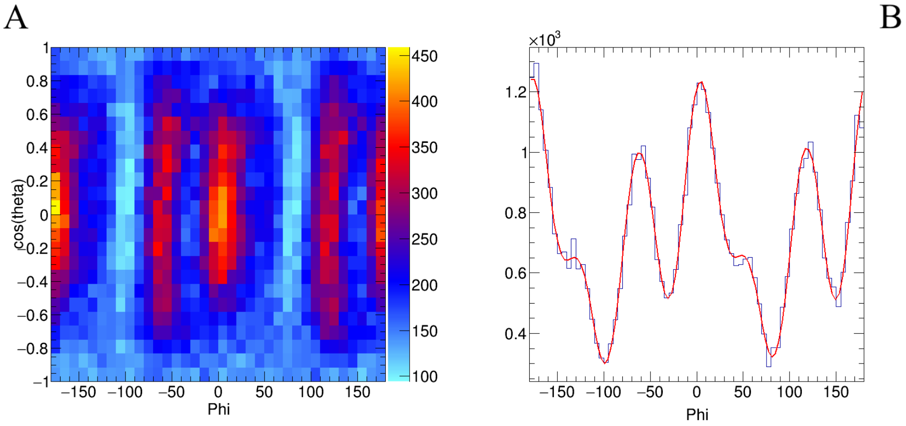

Figure 5.7: Single MFPAD restricted to the polarisation plane for N_2. Left (A): MFPAD in spherical coordinates defined by equation 5.10. Right (B): MFPAD integrated over the laboratory azimuthal angle ϕ; the red curve is a B-spline fit. The magnetic field is 13 Gauss.

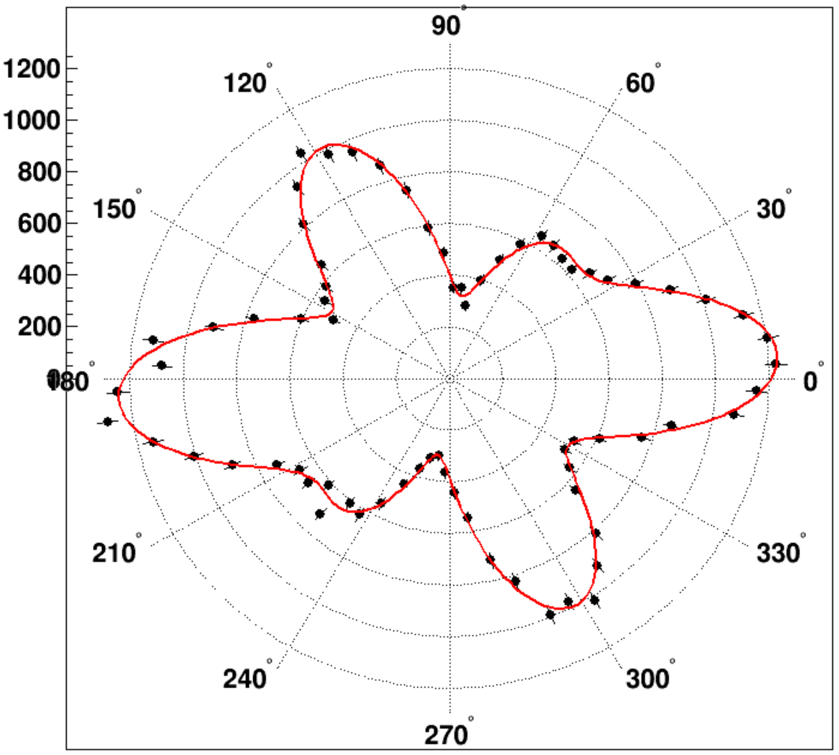

Figure 5.8: Polar representation of data (points) from Figure 5.7 (B). Line: Fit using a sum of spherical harmonics up to l=4. The error bars represent the standard statistical error.

5.4 ELECTRON CALIBRATION

Photoionisation of the Argon Ar targeting the L shell and M shell as well, at photon energies 260, 280, 300, 325, 350, 380, 400, 450, and 500 eV were used for a more precise calibration of the electron arm of the spectrometer. We used photoionisation to create electrons with well-defined kinetic energies for the calibration experiments without changing the spectrometer settings. The Ar(2p) electrons have binding energies of 250.6 eV $(2p_{1/2})$ and 248.8 eV $(2p_{3/2})$ and the photon energies were chosen so that the excess energies covered the whole spectrum of electron energies that were expected in the corresponding main measurements. An example is presented in the next figure 5.9 and shows the results of the calibration measurements conducted during Session 2, that is, during the Isopropanol Run as calculated with the final parameters. Here, the electron energy is shown as a function of the spherical coordinates with respect to the electric field axis of the spectrometer. For the electron, calibration is used the low magnetic field, close to 13 Gauss and the first results correspond to the low magnetic field. In addition to the necessities of the specific session, the calibration was also taken place in a high magnetic field, close to 42 Gauss. In the second presentation 5.10 is shown the results of the high magnetic field. There are two spectrometer settings, the first one in a magnetic field of 42 Gauss, and the second one in a magnetic field of 13 Gauss. For both calibrations runs were used Argon ($2s$ and $2p$) at photon energies 260, 280, 300, 325, 350, 380, 400, 450 and 500 eV. The results are shown in figures 5.9 and 5.10. In both representations, all the different electron energies used during the calibration process are added together, for the sake of simplicity. The results are presented as a function of the spherical polar and azimuthal angle coordinates.

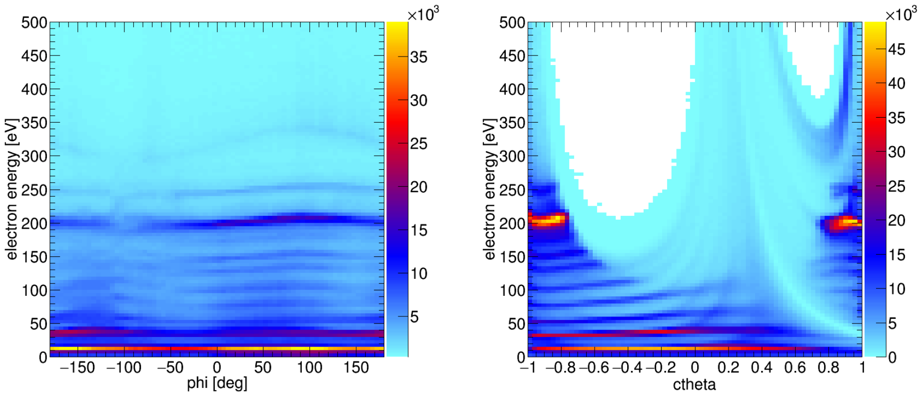

Figure 5.9: Results of the calibration measurements conducted during Session 2 (studying photoionization of isopropanol): Photoionisation of Ar($2p$) electrons at photon energies of 260.0 eV, 280.0 eV, 300.0 eV, 325.0 eV, 350.0 eV, 380.0 eV, 400.0 eV, 450.0 eV and 500.0 eV. Electron kinetic energies as a function to angle ϕ (left)and as a function of the cosine of angle θ concerning the electric field of the spectrometer (right).

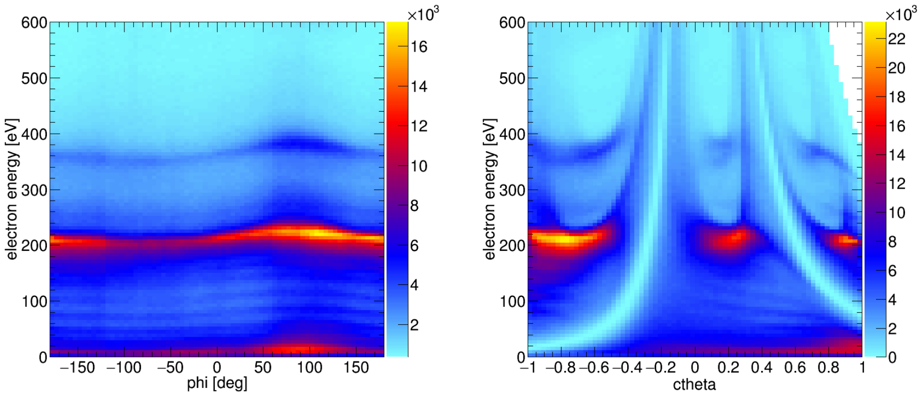

Figure 5.10: Results of the calibration measurements conducted during Session 2 (studying photoionization of isopropanol): Photoionisation of Ar($2p$) electrons at photon energies of 260.0 eV, 280.0 eV, 300.0 eV, 325.0 eV, 350.0 eV, 380.0 eV, 400.0 eV, 450.0 eV, 500.0 eV and 600.0 eV. Electron kinetic energies as a function to angle ϕ (left)and as a function of the cosine of angle θ concerning the electric field of the spectrometer (right).

Part IV

RESULTS

6

FORMIC ACID AND CHIRALITY

In the ensuing chapters, the findings of experiments, conducted at the PIPE *III* beamline at the Deutsches Elektronen-Synchrotron (DESY) facility in Hamburg will be presented. These experiments were designed to explore to which extent of Molecular Frame Photoelectron Angular Distribution (MFPAD) can help to reveal the structure of prochiral molecules, with a focus on formic acid.

Prochiral molecules are planar, but as the face of a clock they allow to define a sense of rotation when looked at from one side. Such prochiral molecules can transform into a chiral structure by bending into the third dimension.

We present experiments at photon energies below the 1s ionisation threshold where the molecule is excited and explore how this excitation triggers a conformational change. Furthermore, by augmenting our understanding of the spatial orientation of the molecules, the results for molecules that are fully fixed in space, or derived from polyatomic breakup, are presented.

We exploited the data recording architecture of the Cold Target Recoil Ion Momentum Spectroscopy (COLTRIMS) apparatus, allowing us to gate the raw data during the analysis phase and selectively isolate the events of interest. For each molecular breakup channel, we gated the Kinetic Energy Release (KER), relative and sum momenta. With regards to the formic acid breakups, additional restrictions were imposed on Newton plots.

In the following sections, the analyses and implications of these experimental findings are discussed in depth, furthering our understanding of the molecular dynamics and potential chirality of formic acid.

The motivation for the investigation on the chirality properties of the molecule of formic acid comes from the fact that the equilibrium structure of the molecule is planar in its ground state. As a consequence the expectation value of any angle defining α out of plane bending is zero. Due to the quantum nature however the square of the wave function shows a continuous distribution of geometries for which the set of exact planar ones has measured zero, which means that every single measurement will find a non planar geometry. Based on this idea, two different types of measurements were performed.

In the first set of the experiments, we excite the molecule and then the molecule is exploded via the Coulomb explosion mechanism. In these excitation based experiments, a chiral signal was measured. Most likely this is a dynamical induced chirality since the core excited states have a nonplanar equilibrium geometry and the molecule lives for a short time in this excited neutral state so that it can be deformed.

In a second set of experiments, a photoionisation measurement is performed, in which the electron from the inner shell of an atom leaves the molecular system instantly. On its way out of the molecule the photoelectron is diffracted at the instantaneous molecular structure. Through this process, the interaction between the electrons and the atoms of the molecule causes the electrons to scatter in different directions. The diffraction pattern of the electrons is a powerful tool for studying the structure as well as the physical and chemical properties of materials at atomic and molecular levels. According to this second measurement, a direct chiral signal also occured in the photoelectron diffraction pattern. This diffraction pattern is given by Molecular Frame Photoelectron Angular Distribution (MFPAD), which provides a useful insight into the molecular dynamics and structure of the molecule. Literally, the angular distribution of the photoelectron is measured in the molecular or fragmentation frame, which is defined by the molecular axis or a specific reference direction. The angular distribution is recorded in terms of azimuthal and polar angles, providing information about the shape of the molecule and the electronic states involved in the ionisation process.

The reaction channels measured in this part of the experiment are presented in 6.1 in the case of the excitation of an electron from carbon, in 6.2 in the case of the excitation of an electron from oxygen and in 6.3 in the case of full photoionisation, targeting an electron from the K shell of carbon.

$$HCOOH + \gamma \rightarrow HC^{*}OOH \rightarrow H^{+} + C^{+} + O^{+} \tag{6.1}$$

$$HCOOH + \gamma \rightarrow HCO^{*}OH \rightarrow H^{+} + C^{+} + O^{+} \tag{6.2}$$

$$HCOOH + \gamma \rightarrow HC^{*}OOH \rightarrow H^{+} + C^{+} + O^{+} + e^{-}_{\gamma} \tag{6.3}$$

In the following part of the formic acid results, the results of the excitation states are presented first, and the results of the photoionisation are presented second, identifying every time the necessary fragments for the analysis.

6.1 EXCITATION STATES OF FORMIC ACID

6.1.1 *Theoretical Description of Formic Acid for the Excitation case*

Formic acid, inherently an achiral molecule, consists of an $sp2$ hybridised carbon atom linked to three bonding partners, thus forming a planar structure in its electronic ground state. In the standard notion of chemistry, a chiral molecule involves the existence of two distinct enantiomers, each serving as the mirror image of the other. These enantiomers, while identical in terms of their physical and chemical properties, interact differently with circular polarised light. Our present study has two main goals. Firstly we aim to electronically excited the molecule to a state for which the potential energy surface has two distinct minima for a non-planar geometry, forming a double well potential and induce molecular motion. This will drive the molecule into a chiral configuration. Secondly, we aim to perform single molecule measurement of the ground state geometry with the goal to show that the molecule is planar only for an ensemble average while each individual measurement shows an out of plane chiral geometry.

Our methodology entails the use of Near Edge X-ray Absorption Fine Structure (NEXAFS) spectroscopy. This technique provides immediate insights into the molecular configuration by exciting an electron from its ground state to an excited state. The NEXAFS method involves exposing the sample to X-ray radiation, which subsequently leads to absorption. If the photon energy surpasses the core ionisation energy, a core electron, such as the $1s$ electron, can escape to the continuum, detectable via X-ray photoelectron spectroscopy.

However, by selecting photon energies proximate to, yet slightly below the core ionisation threshold, the electron remains bound. Still, an excitation to unoccupied states is possible. As NEXAFS studies require tuneable X-ray radiation they are performed at synchrotron radiation facilities.

NEXAFS yields information about the unoccupied target states and aids in determining the molecular structures using synchrotron radiation facilities. The subsequent sections of this dissertation will elaborate on the findings derived from applying these methodologies to formic acid, focusing on various excited states and specifically targeting the carbon and oxygen constituents within the molecule.

The subsequent table 6.1 presents a list of the first relevant excited states, alongside the corresponding binding energies and the final orbitals that can be occupied upon the excitation of a core electron from the formic acid molecule, considering both the carbon atom and the two oxygen atoms present in the molecule.

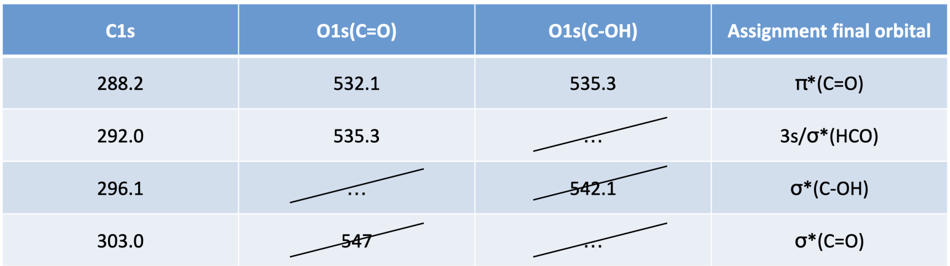

C1s	O1s(C=O)	O1s(C-OH)	Assignment final orbital
288.2	532.1	535.3	π*(C=O)
292.0	535.3	~~...~~	3s/σ*(HCO)
296.1	~~...~~	~~542.1~~	σ*(C-OH)
303.0	~~547~~	~~...~~	σ*(C=O)

Figure 6.1: Binding energies and state assignments targeted the K-shell of several atoms consisting of the molecule HCOOH. The energies with a black diagonal line are related to some excited state but there are no measurements in this analysis [69].

It is known that the excitation from the ground state to the π^* state, with a vertical transition energy of 5.9 eV, leads to pyramidalization, creating a chiral equilibrium geometry [70–72]. In a more simplified picture, an electron from the bonding orbital at the carbonyl oxygen atom is transferred upon excitation to the anti-bonding π^* orbital of the carbonyl group [71]. In the equilibrium structure of this electronically excited state, the carbonyl oxygen is moved out of the plane relative to the nearly coplanar other four atoms. If we use the three heavy atoms as reference, the hydrogen at the carbonyl group is bent on average 32 degrees out of the plane [72], which is spanned by the carbonyl oxygen, the hydroxyl oxygen and the carbon atom. This displacement of the hydrogen is accompanied by a torsional motion of the acidic hydrogen in the opposite direction.

To quantify the degree of handedness it is helpful to define triple products, like equations 6.4 and 6.5. Since coulomb explosion imaging measures the fragment momentum vectors, the triple product uses these momentum vectors, by a normalised triple product with the letter as shown in the equation 6.4, containing the linear momentum vectors of the three ions bound to the carbon centre, in the case of a four body breakup channel [73, 74]. In the case of a three body breakup channel, one of the oxygen atoms is substituted with the carbon atom, as shown in the equation 6.5. The numbers are an indication of distinction of the different atoms from the molecule. Defining with $O1$, the oxygen connected with the double bond to carbon, named carboxyl oxygen, and $O2$ the oxygen connected with single bond to carbon, named hydroxyl oxygen. Proportionally, the $H1$ is the hydrogen connected directly to carbon, named carboxyl proton and $H2$ the hydrogen connected to the hydroxyl oxygen $O2$.

$$\text{chiral angle}\quad cos(\alpha) = (\vec{O}2 \times \vec{O}1) \cdot \vec{H}1/(|\vec{O}2 \times \vec{O}1| \cdot |\vec{H}1|) \tag{6.4}$$

$$\text{chiral angle}\quad cos(\alpha) = (\vec{O}2 \times \vec{C}) \cdot \vec{H}2/(|\vec{O}2 \times \vec{C}| \cdot |\vec{H}2|) \tag{6.5}$$

In the case of a four body breakup channel, it provides the emission angle of the $H1$ ion with respect to the normal of the plane defined by the momenta of the two oxygen atoms. According to both cases, the triple product is zero for a planar break-up, and positive values indicate that the molecule breaks up as the R enantiomer and negative values indicate the breakup as the S enantiomer. $\cos\alpha$ varies from $(-1\ ,\ 1)$, where the maximum absolute values correspond to the linear momentum vector of $H1$ being normal to the plane spanned by the linear momenta of $O2$ and $O1$ [51].

6.1.2 *Selection of Proper Channels*

As in the previous chapter 5.3, the PIPICO spectrum with two or more ions includes a rich information on the fragmentation of polyatomic molecules. The corresponding spectrum in the case of formic acid or simply HCOOH is shown in Figure 6.2, and the expected times-of-flight of the most relevant fragments are listed in Table 6.1. The total mass of formic acid is $m = 46$ a.u., and the breakup channel for the analysis belongs to the area marked with a pink rectangular frame in Figure 6.2. In addition to that, using the information from the $3PICO$ histogram and the time-of-flights from table 6.1, a secondary breakup channel defined with 4 ions. Both definitions are incomplete channels, which means that further fragments have not been detected. This could result from non unity of our detection efficiency or from those fragments being neutral. The time-of-flight of the ions in the table 6.1 is coming from the calibration measurements using the $C\ O$ molecule, taking into account the breakup channel $C^+\ O^+$.

Ion	m/q	tof(p=0) [ns]
H^+	1	500
C^+	12	1650
O^+	16	1900

Table 6.1: The time of flight corresponds to ion born with zero energy in our spectrometer (noted as p=0).

For most of our analysis we used events in which three or four particles have been detected. The corresponding 3pico and 4pico spectra are shown in Figure 6.3. We also recorded a small number of events with 5 detected fragments. This was used for calibration, since in this case adding the momenta of all particles should result in a distribution centred at zero. The main channel for the analysis is the 3 body breakup channel because of the higher statistics in comparison with all the others.

We conclude this subsection by showing some raw histograms which are helpful in the course of the data analysis. In Fig 6.3 we show several zoomed in regions of the 3pico, 4pico and 5pico. Here the regions of interest which are set to select the HCO, HCOO and HCOOH or full

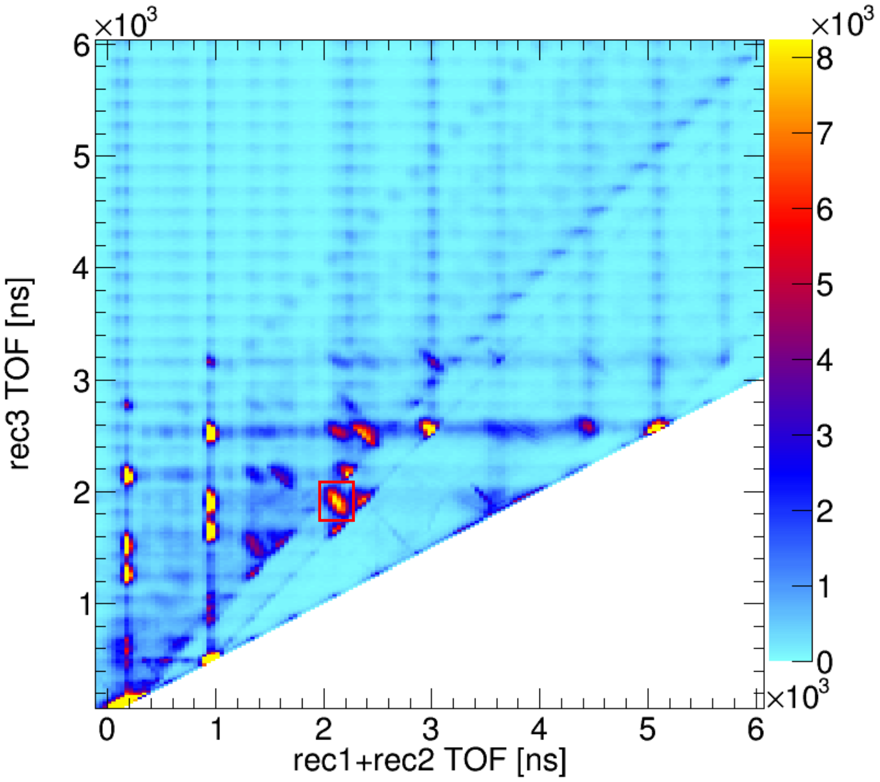

Figure 6.2: 3PICO spectra: Horizontal axis: sum of time-of-flights of 1^{st} and 2^{nd} ion. Vertical axis: time-of-flight of 3^{rd} ion. The red square identify the 3 body breakup channel of interest, consisting of H, C and O. The time-of-flight of the particles are found by the initial calibration with the CO molecule and the $C^{+}O^{+}$ breakup channel. The colour bar shows the counts of the plot.

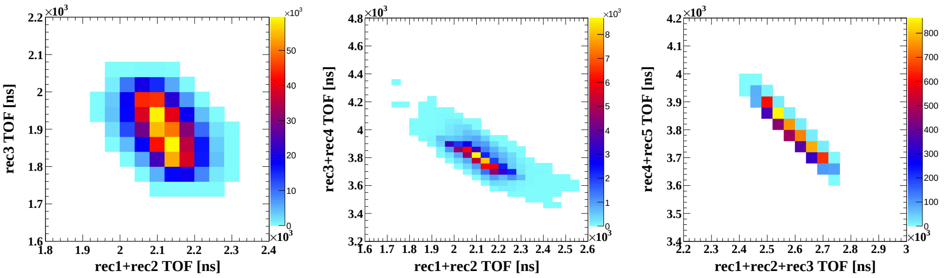

(a)

(b)

(c)

Figure 6.3: By zooming in different ion islands from figure 6.2, different breakup channels of formic acid are presented. Left: Three body breakup channel including the H, C and O. Centre: Four body breakup channel including the H, C, O and O. Right: Full breakup channel, formatted a straight line.

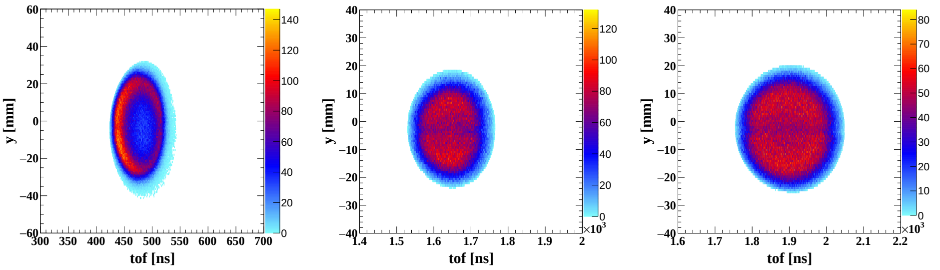

(a)

(b)

(c)

Figure 6.4: Time-of-flight versus y-direction position-of-impact. The proton H (left), the carbon C (centre) and the oxygen O (right). The histograms show the measured time-of-flight of the particles according to the experimental settings of the experiment, in consistency with the above mentioned table. The sum momenta was gated between -150 and 150. In addition to that, gates in momentum space for every particle are applied to keep only the unique information of its particle. H: $|\vec{P}| < 60$, C: $|\vec{P}| < 120$, and O: $|\vec{P}| < 150$.

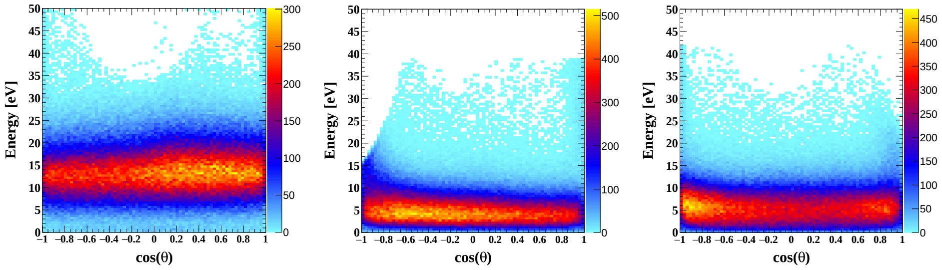

(a) (b) (c)

Figure 6.5: Ion energy distribution from figure 6.4 as a function the angle θ. The θ angle is defined as the angle between the fragment's momentum in the direction to the time-of-flight and the magnitude momentum of every fragment, in the Laboratory Frame. Left: Ion energy of H. Centre: Ion energy of C. Right: Ion energy of O

fragmentation channel are shown. In addition to the inspection of the correlations of times-of-flight and positions-of-impact or the individual ions are helpful to search for potential anomalies in the data or to spot potential backgrounds. Corresponding histograms are shown in Figure 6.4.

The histogram discussed so far show flight times and positions-of-impact. From those quantities the components of the momentum vector of each detected ion can be calculated 5.3. These calculation require spectrometer geometries and fields. Those can most precisely be inferred from the data itself. To this end we inspected histograms shown in figure 6.5. The approximate angle independence of the ion energy shows the quality of the calibration procedure. Figure 6.5 also show high energy regions where no events are detected as ions with this energy and respective angle miss the ion detector.

6.1.3 *Results of Excitation*

In the first experimental session focusing on excitation we used a high electric field at 160 V/cm. This is the best setting for identifying the different ionisation channels and clearly separating masses. We used no magnetic field. During this first experimental session, the goal was the excitation of an electron from carbon or oxygen 1s shell of the ground state of the molecule to different excited states such as the π^*, the σ^*, etc. The photon helicity was switched every four hours between left circularly polarised light LCP and right circularly polarised light RCP. The rate was roughly 28 kHz for the recoils and 24 kHz for the electrons.

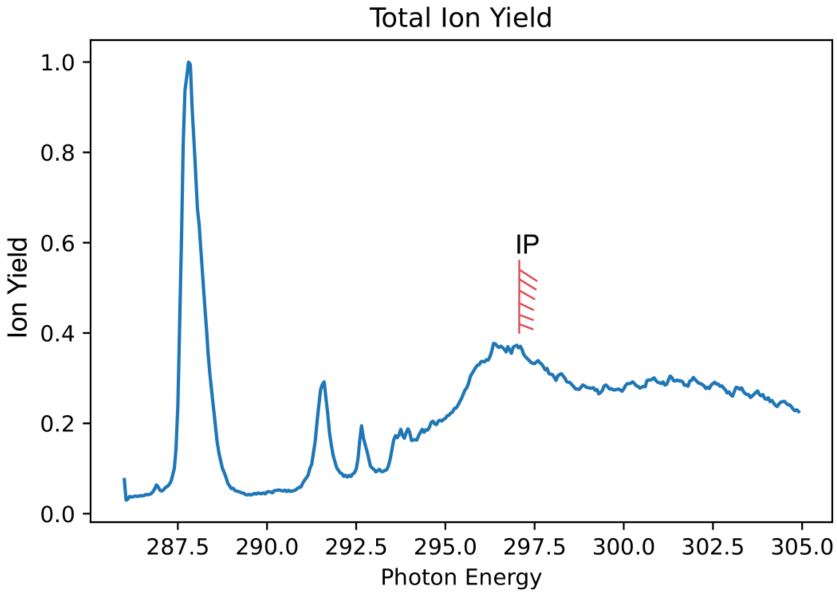

Figure 6.6: Excitations of electron from $C(1s)$ state. The ionisation potential is located at photon energy 296.0 eV [75].

For all the resonances corresponding to the excited states, manual energy scans are performed around the resonances of the states in order to be compared with the theoretical values from the literature [69]. The manual scan in case of excitation of an electron from the K shell of carbon are presented in figure 6.6. The photon energy at 287.9 eV belongs to π^* excited state, with which we hope to trigger the pyramidalization and thus to reach a chiral configuration. The photon energy at 291.6 eV refers to the σ^* state between the carbonyl hydrogen and the carbon. The literature refers to that as $3s\sigma^*$. Another possibility is the excitation from the K shell of an oxygen. The photon energy 535.3 eV has a dual nature and belongs to two different excited orbitals. This photon energy leads to an excitation either to the π^* state from the single bonded oxygen to carbon or the σ^* between the carbon and the double bonded oxygen, connected to carbon. The 532.1 eV photon energy is addressing the π^* state, created by the carbon and the double bonded oxygen [69]. A full energy scan of C(1s) shell (ionisation potential 296.0eV) is shown in Figure 6.6.

The handedness or the chiral angle $cos(\alpha)$ defined as the emission angle of the H ion with respect to the normal of the plane defined by the momenta of the C and the O atoms. A value of zero of $cos(\alpha)$ suggests the planar structure of the molecule, while positive values indicate that the molecule breaks as the R enantiomer and negative values indicate that the molecule breaks as the S enantiomer. An example of the R and S enantiomers from the achiral formic acid are shown in figure 6.23. In the laboratory frame the angles θ and ϕ are the direction of the incoming photon beam, as shown in figure 6.22. The calculation of the chiral angle are based on equation 6.5.

For this calculation used only the momenta of the fragments of the three body breakup channel, i.e. H, C and O. The calculation of the true mean value of the chiral angle $cos(\alpha)$ was performed by calculating the chiral angle for different ranges of the angle $cos(\theta)$ and the azimuthal angle ϕ and normalised the calculations to zero. In this case, the angles θ and ϕ are the projection of the incoming photon beam to the molecular frame, defined by the momenta of the carbon and oxygen atoms. The position of the atoms within the three body breakup channel as a function of the angle θ and ϕ are presented in figure 6.7.

The calculation of the mean value of chiral angle based on the equations 6.5 included the definition of the molecular frame (MF). The results are presented as a function of $cos(\theta)$ and ϕ. The participated ions in the three body breakup channel were the H, C, and O. The molecule consists of two protons and two oxygens, making the ions indistinguishable. For the proper assignment of the ions, the technique from the reference [72] was used. All linear momentum vectors of the atoms were rotated in space such that the momentum of the carbon ion, which was identified by its time-of-flight, points in the direction of the x axis, and the linear momenta of the two oxygen ions define the xy plane. The proton whose momentum is pointing in the same direction as the carbon's momentum was assigned as H1 and the other H atom as H2. The oxygen atom being on the same side of the xz plane as H2 is the O2 atom. The angle between the x axis and the H1 momentum vector was required to be smaller than $acos(0.4)$, and for the H2 momentum vector, the angle was gated to be between $acos(0.4)$ and $acos(-0.8)$. In this work, we retained the same assignment as in the paper [51].

The very first step for the analysis is the definition of the molecular frame, based on the participated ions within the breakup channel. Our combination ensures the highest statistics for the results. The desired combination includes the carbon with one proton and one oxygen attached to the carbon. The molecular frame requires the definition of three axes with the last one produced by the cross product of the two first ones. The z axis is defined by the cross product of the carbon and the oxygen, or $\hat{z} = C \times O2$. The x axis is defined by the cross product of the z axis with the carbon, or $\hat{y} = \hat{z} \times C \times \hat{z}$. By definition the third axis is the cross product of the latter ones, or $\hat{x} = \hat{z} \times \hat{y}$. The photon is travelling in the x direction as the direction of the light. Based on that definition, the projection of the θ angle and the ϕ angle of every participated ion under the above mentioned molecular frame is presented in the figure 6.7 as function of the ϕ angle in the x axis and the $cos(\theta)$ angle in the y axis. This molecular frame is also used on the calculation of the mean value of the chiral angle, shown in 6.5.

In the following, we discuss how much out-of-plane the molecule fragments when it is cores exited. To quantify the degree of out-of-plane fragmenta-

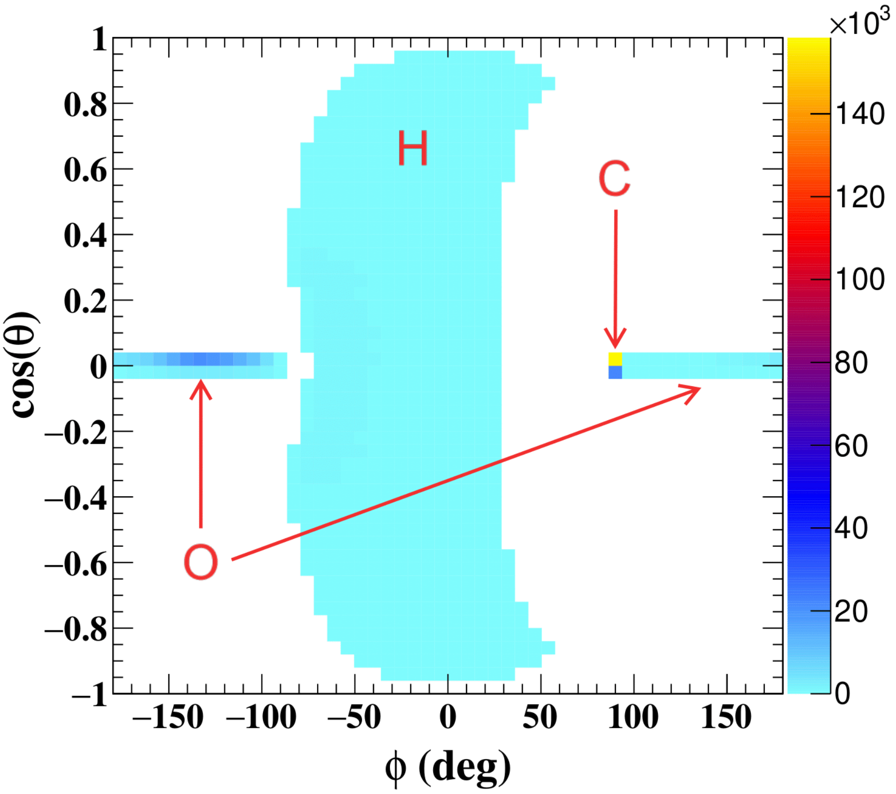

Figure 6.7: Projection of all the participated ions into the Molecular Frame (MF) as a function of the angles ϕ and $cos(\theta)$ in the x and y axes, respectively. The carbon lies in $cos(\theta)$ equals zero and ϕ equals 90 degrees. The oxygen O belongs to the hydroxyl group, connected with the proton H, named O2. The mentioned proton named H2.

tion we examine the cosine of the chiral angle α as defined in equation 6.5. Here $cos(\alpha) = 0$ corresponds to the planar configuration, $cos(\alpha) > 0$ (< 0) to a left (right) handed fragmentation pattern [51]. We use the data from the three body fragment for the analysis, as this dataset has the highest statistics. The four body channel breakup channels show qualitatively similar behaviour.

The first excited state which is of great interest for this work is $\pi^{\star}$. A representation of this state using the molecule of formic acid in a chiral structure within a theoretical framework is presented in Fig. 6.8b. A representation of the transition from the ground state to the excited state $\pi^{\star}$ is also presented in Fig. 6.8a. In this figure the upper excited state shows the chiral configuration, which is distinguished to a left-(R enantiomer) or right-handed equilibrium configuration (S enantiomer), depending on the bending coordinate. An electronic excitation, marked by a dashed red arrow, indicates a transition between these states. The matrix element, denoted as M(R,θ,ϕ), depends on the light direction in the molecular frame of reference. This dependency changes for each configuration. A detailed definition of θ and ϕ can be found in Fig. 6.9. Fig. 6.11 a, d show the distribution of $cos(\alpha)$ for C(1s) excitation to the π^{*} state at photon energy of 287.8 eV (a-c) and 287.9 eV (d-f). Panels (a) and (d) show the distribution of $cos(\alpha) = 0$ integrated over all molecular orientations with respect to the light propagation direction. We observe a broad distribution of fragmentation geometries with a significant minimum for the planar configuration. This clearly indicates that the excitation to the π^{*} state leads to an out of plane deformation of the molecular structure. This is in agreement with the non planar equilibrium structure predicted in paper [51]. As the data in panels a and d of Fig. 6.11 are integrated over all orientations of the polarisation plane, the distribution of $cos(\alpha)$ is symmetric, and R,S enantiomer are populated with equal probability.

To search for a potential break of the symmetry of racemic population of R and S configuration by the excitation process we inspect the fragmentation in the coordinate system introduced in Fig. 6.7. In panels (b, c, e, f) of Fig. 6.11 the expectation value of $cos(\alpha)$ is colour coded. For a racemate one would find $< cos(\alpha) >= 0$. The key result to be taken from these panels is that the direction from which the light impinges onto the planar molecules allows to select whether the excited molecule will bend into the R or S enantiomer. Panels (b, c, e, f) show the expected symmetry that the sign of $cos(\alpha)$ inverts upon inverting $cos(\theta)$. This is expected since $cos(\theta) = 0$ corresponds to the geometry that the polarisation plane is perpendicular to molecular plane in the initial state. This symmetry is in agreement with the observation in the multi photon multiple ionisation regime [51]. The plots presented the mean value of $cos(\alpha)$ obtained by calculating the chiral angle to possible molecular orientations with regard to the angles ϕ and θ. The one-dimensional plots of the $cos(\alpha)$ are presented in the figure 6.10. On

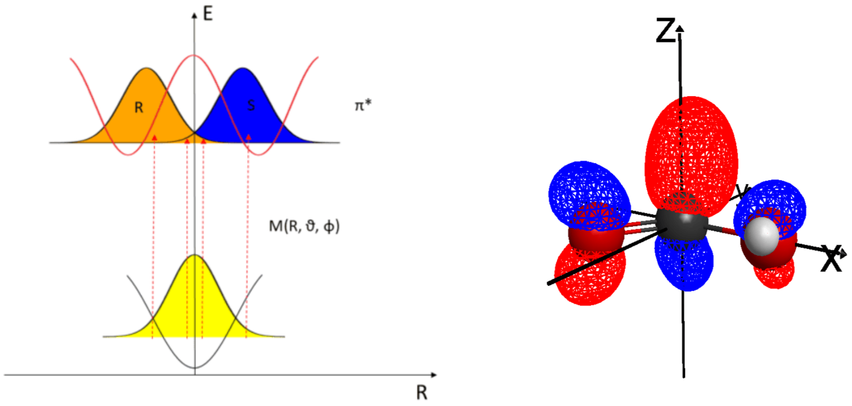

Figure 6.8: Modelling of symmetry breaking: (a) horizontal axis: generalised bending coordinate of formic acid, $R = 0$ corresponds to the planar configuration, $\Psi > 0$ to the S geometry, $\Psi < 0$ to the S geometry. Lowest potential surface shows the ground electronic state, upper double well surface shows the $\pi^\star$ excited state with a left or right-handed equilibrium configuration. The dashed red arrow indicate the electronic excitation. The matrix element $M(R, \vartheta, \phi)$ depends for each configuration R differently on the light direction in the molecular frame of reference (for definition of ϑ, ϕ see Fig 6.9). (b) $\pi^\star$ orbital for a chiral geometry in which the $H1$ atom is bent by 20 deg out of plane.

those plots (a-d), some random combinations of the molecular orientations are used, showing the existence of two potential enantiomers.

All values of $< cos(\alpha) >$ unequal to 0 show that for the respective direction of the impinging photon the part of the π^* orbital situated above the molecular plane is populated with a different probability than the part below the molecular plane. This unequal electron density then leads to a bending of the molecule. What is the mechanism by which a single colour light pulse, whose electric field is inversion symmetric, can lead to a symmetry broken electron density? A schematic answer is given in Fig 6.8b. The dipolar matrix element is maximal when the highest value of the initial and final state of the electron are along the polarisation axis. This allows to break the symmetry between transferring population to one versus the other half sphere above or below the molecular plane.

Panels b,c, e,f in Fig 6.11 differ by the light helicity and by 0.1 eV of photon energy difference. Qualitatively they are very similar indicating that the light helicity does not play a major role for the symmetry breaking. As a consequence a similar effect can be also expected for linearly polarised light.

In the ground state of formic acid, the equilibrium configuration is planar, where its potential energy curve, when mapped against the generalised bending coordinate Ψ, has its local minimum at $\Psi = 0$ and exhibits symme-

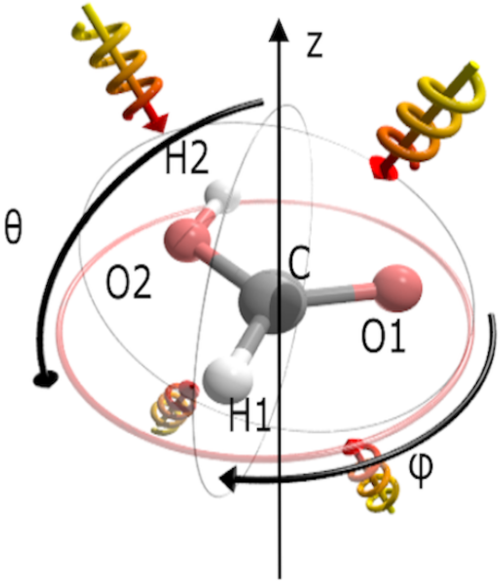

Figure 6.9: Definition of angles from which the photon approaches the formic acid in its prochiral ground state. θ is the angle between the photon direction and the normal to the plane spanned by the $O1^+$ and C^+ momentum vectors. The azimuthal angle ϕ is defined with respect to the C^+ momentum.

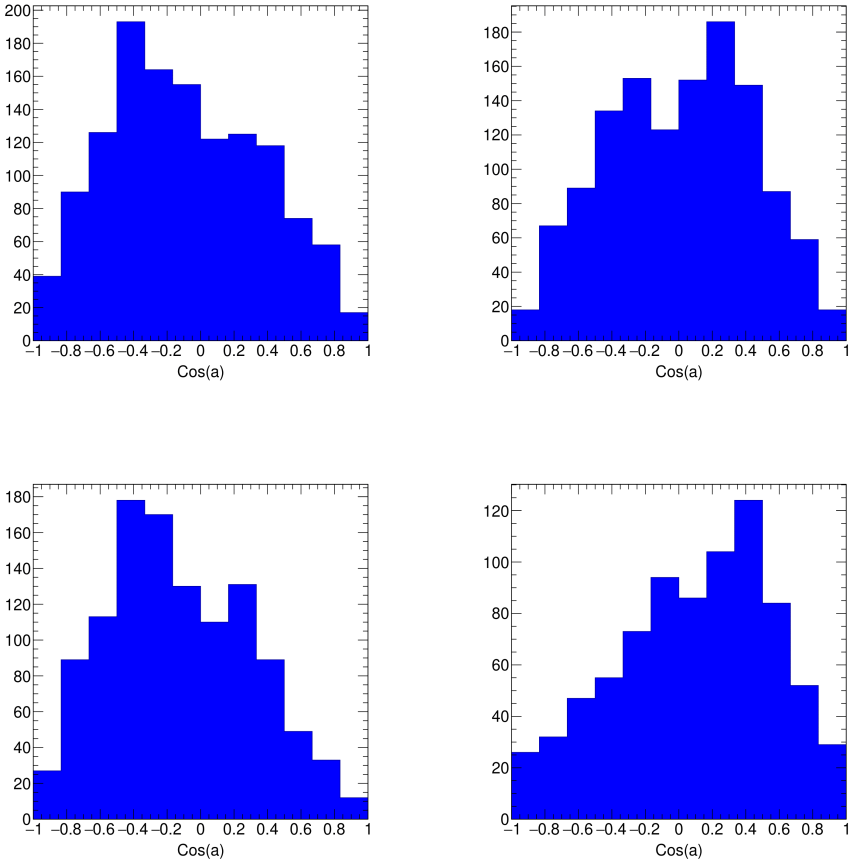

Figure 6.10: Calculation of handedness for different molecular orientations regarding the $cos(\theta)$ and ϕ in the molecular frame in the case of excitation to the π^* orbital by a circular polarised light at photon energy 287.8 eV. A: $\phi = [60, 120]$ and $cos(\theta) = [-0.6, -0.466667]$, B: $\phi = [-60, 0]$ and $cos(\theta) = [-0.066667, 0.066667]$, C: $\phi = [-120, -60]$ and $cos(\theta) = [0.466667, 0.6]$, D: $\phi = [60, 120]$ and $cos(\theta) = [0.733333, 0.866667]$

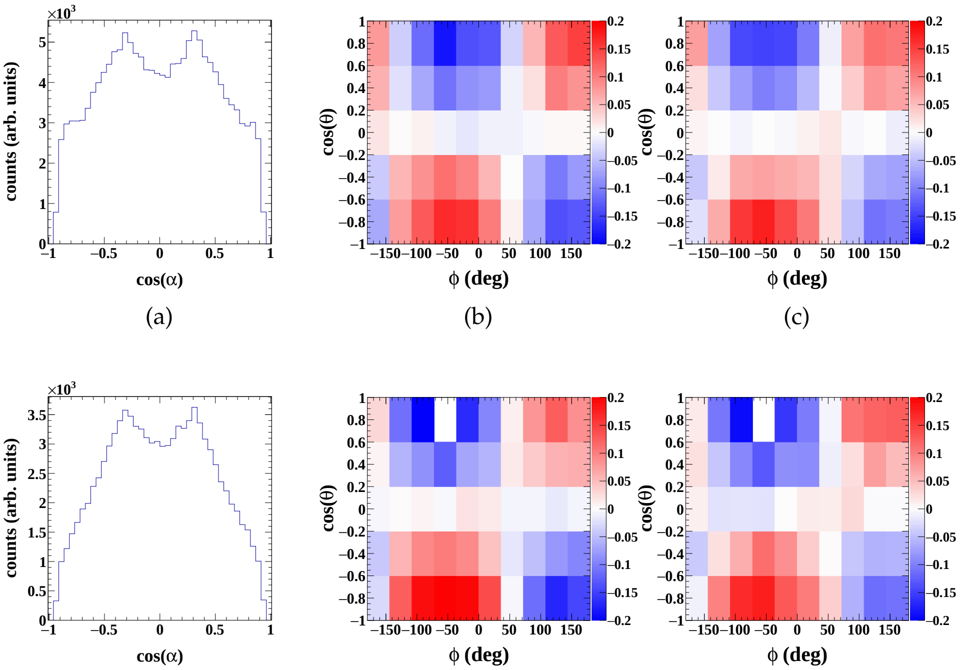

(a) (b) (c)

(d) (e) (f)

Figure 6.11: Handedness or chiral angle: Excitation of formic acid π^* at photon energy 287.8 eV (top) and 287.9 eV (bottom) by circular polarised light. Calculation of the chiral angle integrated over all directions (left). Mean value of chiral angle in the MF as a function of $cos(\theta)$ and ϕ, using LCP (centre) and RCP (right).

try, as shown in the lower potential line of 6.8a. This can be visualised by the depicted yellow Gaussian representing the wave function. Given this, any hypothetical single-molecule measurement would likely identify a chiral configuration because the probability of encountering a perfectly planar molecule is essentially zero. Hence, planar prochiral molecules manifest a phenomenon known as dynamic chirality, as discussed by Kitamura in 2001 [76].

Conversely, the $\pi^\star$ excited state is distinguished by a double-well potential, evident in the upper curve of Fig. 6.8a. This potential has its minima at either left or right-handed configurations. The vertical transitions between these states are highlighted by the dotted arrows. A critical component of this process is the transition matrix element $M(R, \vartheta, \phi)$. For a given molecular geometry R, this matrix element's value changes based on the light's polarisation direction in the molecular frame or, more specifically, the angles θ and ϕ, determining the light's incidence on the molecule. The core of the symmetry-breaking mechanism lies in the fact that, for specific values of θ and ϕ, this matrix element differs for positive and negative R, leading to the preferential population of either left or right-handed pyramidalised configurations.

Fig. 6.12a illustrates why this is indeed the case. It shows the $\pi^\star$ orbital for a configuration where the H1 bond is artificially tilted upward ($R > 0$) by 20 deg from the plane. This bend configuration brings larger fraction of the $\pi^\star$ orbital above as compared to below the molecular plane. Note that the upper and lower side of a prochiral molecule are as distinguishable as the top and bottom side of the face of a clock. The initial C(1s) orbital from which the electron is promoted is not centered with respect to the $\pi^\star$ orbital. The transition matrix element will maximise when the polarisation vector points from the C centre to the maximum of the $\pi^\star$ orbital. This intuitive expectation is confirmed by our calculation of the transition matrix element as function of θ and ϕ shown in Fig. 6.12a,b. It shows how the handedness of the $\pi^\star$ for the pyramidalised structure makes the transition matrix element to non trivially depend on θ and ϕ. Fig. 6.12c show the normalised differences between the matrix elements depicted in panels a,b.

This simple estimate of the matrix element shows the same features as we observe in the experiment, with the biggest surplus of R enantiomers at $\theta = 30$, $\phi = -30$ and equal population of both enantiomers at $\theta = 90$ and along lines $\phi = -110$ and $\phi = 70$. This qualitative agreement shows the validity of the proposed mechanism.

Fig. 6.13, shows the equivalent to Fig. 6.11, but for the σ^* state, consisted of the mutual participation of the carbon atom and the carbonyl proton, which is the proton connected directly to the centre atom. This state is also referred as a $3s\sigma^*$ state in the literature and the binding energy is given at

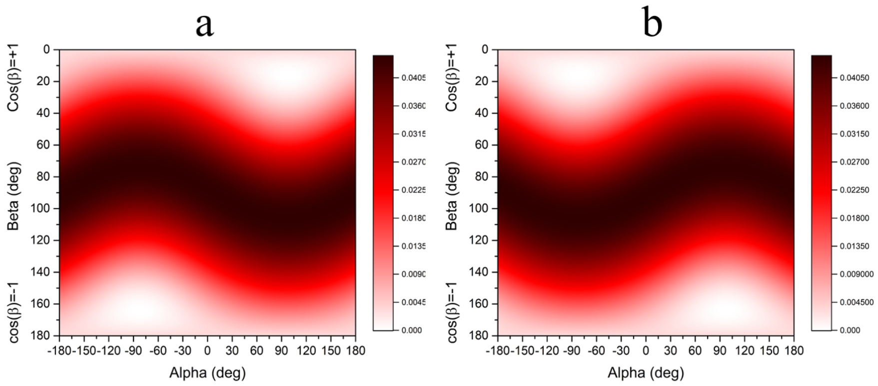

(a)

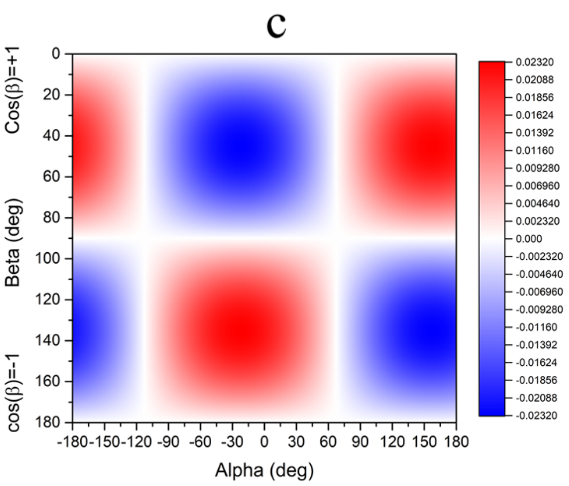

(b)

Figure 6.12: Modelling of symmetry breaking: (a)(b) transition matrix $M^s(R, \vartheta, \phi)$ element for the vertical transition C(1s) to the orbital shown in Fig. 6.8(b) as function of ϑ, ϕ and (b) to its mirror image $M^R(R, \vartheta, \phi)$. (c) normalised difference $(M^R - M^S)/(M^R + M^S)$.

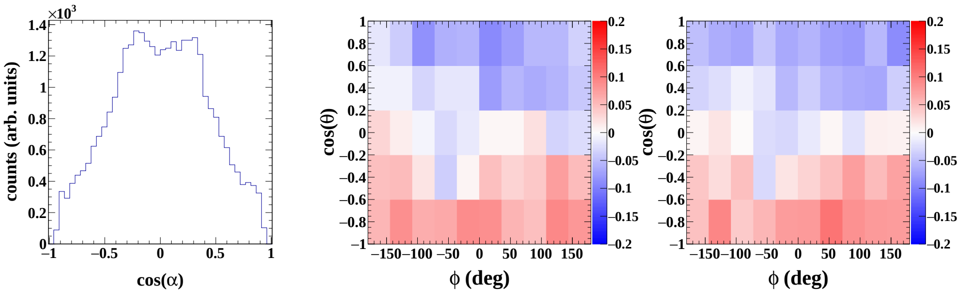

(a) (b) (c)

Figure 6.13: Handedness or chiral angle: Excitation of formic acid $3s\sigma^*$ at photon energy 291.6 eV by circular polarised light. Calculation of the chiral angle integrated over all directions (left). Mean value of chiral angle in the MF as a function of $cos(\theta)$ and ϕ, using LCP (centre) and RCP (right).

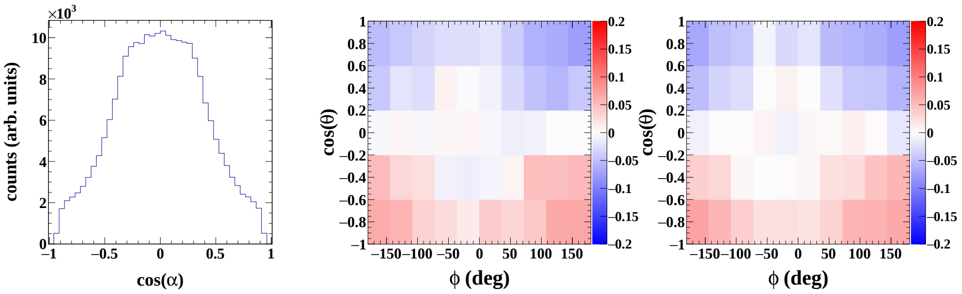

(a) (b) (c)

Figure 6.14: Handedness or chiral angle: Excitation of formic acid σ^* at photon energy 296.8 eV by circular polarised light. Calculation of the chiral angle integrated over all directions (left). Mean value of chiral angle in the MF as a function of $cos(\theta)$ and ϕ, using LCP (centre) and RCP (right).

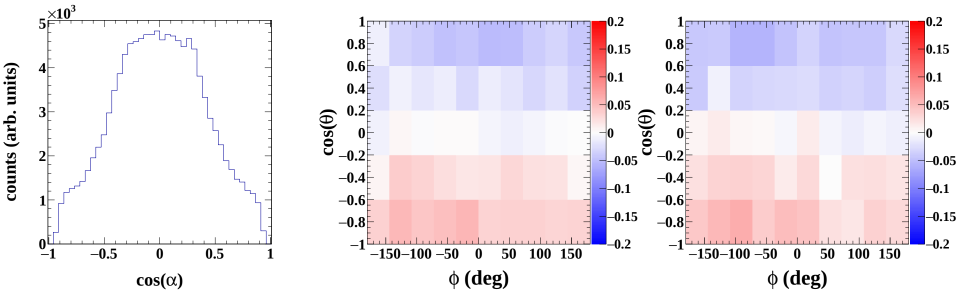

(a) (b) (c)

Figure 6.15: Handedness or chiral angle: Excitation of formic acid σ^* at photon energy 302.8 eV by circular polarised light. Calculation of the chiral angle integrated over all directions (left). Mean value of chiral angle in the MF as a function of $cos(\theta)$ and ϕ, using LCP (centre) and RCP (right).

296.1 eV. The manual scan confirmed this value, as shown in Fig. 6.6.

Comparing Fig. 6.11 panel a with Fig. 6.13 panel a shows strikingly that the fragmentation occurs much more pronounced in the plane of molecule when the sigma state is excited. In particular there is no minimum at $cos(\alpha) = 0$ visible. This is confirmed when the direction of the light is taken into account in the colour panels of Fig. 6.13. There is no significant deviation of the mean value of $cos(\alpha)$ from 0, highlighting that no three dimensional deformation of the molecule occurs for the excitation of the sigma state. This is in agreement with the calculated planar equilibrium configuration of this state [75].

The same sigma state can also be populated by excitation of the 1s orbital of the other Carbon at an energy of 302.8 eV. The results are shown in Fig 6.15. There is no qualitative difference from the pattern in Fig. 6.14.

No chiral formation is visible in figures 6.14 and 6.15. The literature mentions 296.1 eV and 303.0 eV. The manual scan gave 296.8 eV and 302.8 eV for the mentioning excited states. In the latter cases, the binding energies are referring to the contribution of the carbon atom with the carboxyl oxygen at the binding energy of 296.8 eV, and the other one yielded from the interaction between the carbon and the hydroxyl oxygen, at the binding energy 302.8 eV. Looking the calculation of the mean value of the handedness in comparison with the case of the π^* state, there is no clear structure, as a result an indication of the formation of two enantiomers.

So far the excitations from an electron of the ground state 1s of carbon were presented, and a couple of more excitations from an electron of the ground state 1s of carbonyl oxygen are further presented. In figure 6.16, the calculation of handedness for the π^* state was performed. The depiction of

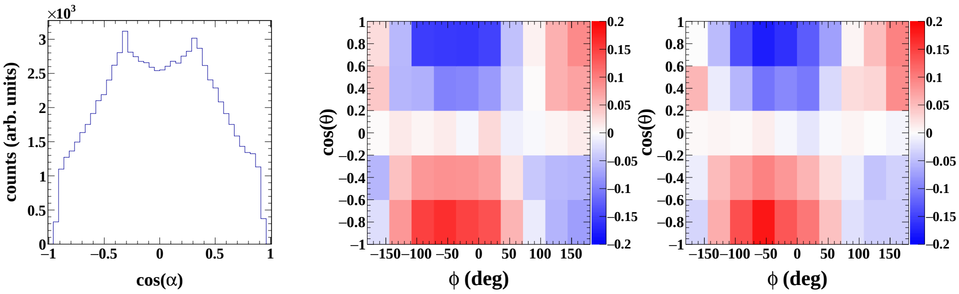

(a) (b) (c)

Figure 6.16: Handedness or chiral angle: Excitation of formic acid π^* at photon energy 531.7 eV by circular polarised light. Calculation of the chiral angle integrated over all directions (left). Mean value of chiral angle in the MF as a function of $cos(\theta)$ and ϕ, using LCP (centre) and RCP (right).

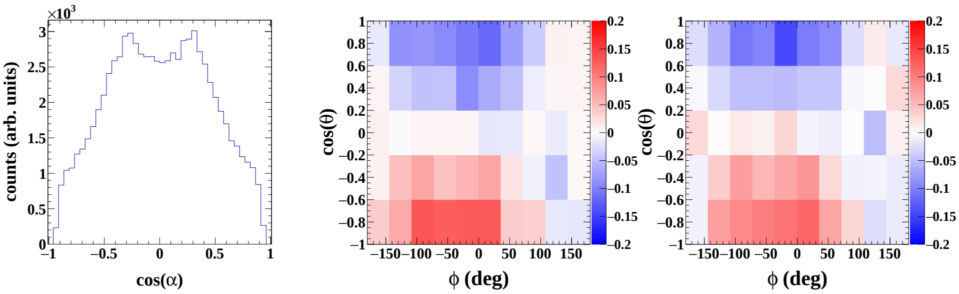

(a) (b) (c)

Figure 6.17: Handedness or chiral angle: Excitation of formic acid σ^* of O1 or π^* of O2 at photon energy 535.4 eV by circular polarised light. Calculation of the chiral angle integrated over all directions (left). Mean value of chiral angle in the MF as a function of $cos(\theta)$ and ϕ, using LCP (centre) and RCP (right). Both states exist according to the literature, with the proper excited state seems to be the π^* from the O2, due to formation of two enantiomers in the calculation of the handedness.

the chiral angle, as on the case of the extraction of the electron from carbon, shows the existence of chirality and the formation of two enantiomers, since the calculation of the chiral angle in this case show a similar structure with the π^* state at the binding energy of 287.9 eV. That reaches at a conclusion that the π^* excited state leads to chiral phenomena, in the case of the achiral formic acid molecule, in contrast, with the σ^* excited states. Finally, the calculation of one more excited state from O occurred, as shown in figure 6.17. On that scenario it is not clear which state is populated since the π^* state of the hydroxyl oxygen O2 and the σ^* of the carbonyl oxygen have the same binding energy. However, the results of the handedness show a clear signal of the formation of the two enantiomers, since the structure is similar with all the π^* states have so far been investigated, leading to the conclusion that this is the π^* excitation of the hydroxyl oxygen.

6.2 PHOTOIONISATION OF FORMIC ACID

6.2.1 *Formic Acid for the Photoionisation case*

Photoionisation is the process by which an electron is ejected from an atom or molecule by the absorption of a photon of sufficient energy. In the case of formic acid, the ionisation of a K shell electron from carbon can be achieved by irradiating the molecule with a high-energy photon, such as an X-ray or a gamma ray. When a high-energy photon is absorbed by the carbon atom in formic acid, it can excite an electron from the K shell to a higher energy level or completely remove it from the atom. The energy of the absorbed photon must be greater than the binding energy of the K shell electron, which is the energy required to hold the electron in its orbit around the nucleus. If the absorbed photon has enough energy to completely remove the K shell electron from the carbon atom, the ionisation of the formic acid molecule occurs, resulting in the formation of a positively charged molecular ions and a free electron.

In this sub-chapter, the photoionisation is employed. The ionisation potential is located at energy 296 eV, in the case of an electron extraction from the K shell of carbon. Two photon energies are used, 305.5 eV and 311 eV. That leads to a photoelectron of either 10 eV or 16 eV, respectively. Measuring a photoelectron in those cases, it opens a new door in the analysis to exploit the powerful technique of Molecular Frame Photoelectron Angular Distribution (MFPAD). See equation 6.3 for all relevant breakup channels. The breakup channel remains the same as in the excitation case, measuring three ion fragments and the photoelectron. The three body breakup channel includes the central atom of the molecule, which is the carbon, along with the hydroxyl oxygen and the proton. The indication names remain the same as in the analysis of the excitation states, meaning C, O2, and H2, respectively. The O2 and H2 are just indexes, implying the

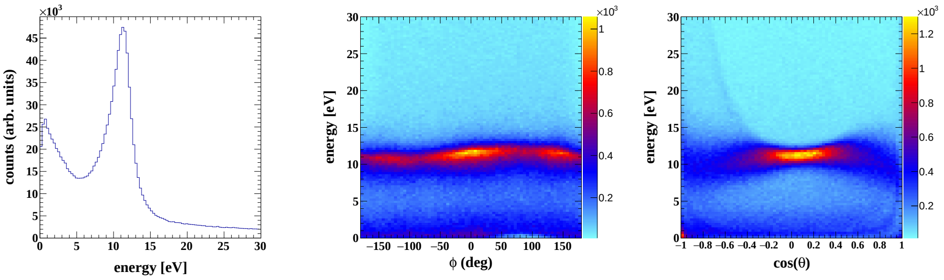

(a) (b) (c)

Figure 6.18: Calibrated electron measurement at photon energy 305.5 eV in the case of photoionisation by a circular polarised light. The kinetic energy of the photoelectron is 10 eV. Left: Electron energy. Centre: electron energy versus the angle ϕ in the laboratory frame. Right: electron energy vs the cosine θ angle in the laboratory frame.

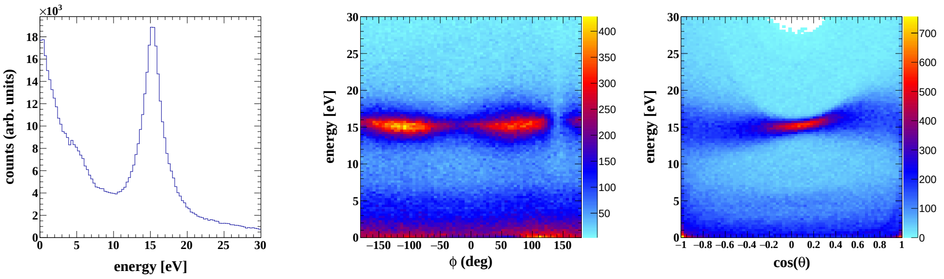

(a) (b) (c)

Figure 6.19: Calibrated electron measurement at photon energy 311.0 eV in the case of photoionisation by a circular polarised light. The kinetic energy of the photoelectron is 16 eV. Left: Electron energy. Centre: electron energy versus the angle ϕ in the laboratory frame. Right: electron energy vs the cosine θ angle in the laboratory frame.

choice of the hydroxyl oxygen with the attached proton on it.

At this time, our data also includes an electron. The calibration of the photoelectron at photon energy 305.5 eV is presented in the figure 6.18. The expected electron energy of the photoelectron is estimated around 10 eV. For the calibrated measurements it is expected a photoelectron kinetic energy around 10 eV. In a similar way, the calibration of the photoelectron at photon energy 311.0 eV is presented in the figure 6.19. The expected kinetic energy of the photoelectron is 16 eV.

6.2.2 *Results of Photoionisation*

Based on the description above about the photoionisation cases, the results are presented in this subchapter. A photoelectron of 10 eV and a photoelectron of 16 eV is presented, since the ionisation potential is located at the energy of 295 eV. At this point, the calculation of the chiral angle emerges the unique effect of the chiral formation and the two enantiomers appear in figure 6.21. Later, in the analysis, the photoelectron was exploited to acquire access to the structure of the molecule, under the powerful technique of Molecular Frame Photoelectron Angular Distribution or MFPAD. A difference at the photon energy 311 eV appears in comparison with the data at photon energy 305.5 eV by calculating the chiral angle because the two measurements are coming from different experimental settings and sessions. That means that there were also differences in the electromagnetic field, resulting a discrepancy in the calculation of the chiral angle at the photon energy 311 eV, as shown in the following figures.

In figure 6.20, the calculation of the handedness was performed for different molecular orientations. The procedure was to define the Molecular Frame in the same way as in the case of the excitation of the molecule HCOOH. For all the different molecular orientations, the handedness was calculated based on equation 6.5. Some indicative results are presented in figure 6.20 for some specific orientations. In figure 6.21, there are two different things. The left part of the figure is the calculation of the chiral angle integrated over all molecular orientations. The middle part and the right part of the figure 6.21 show the calculation of the handedness taking into account the different molecular orientations for the negative and the positive helicity, respectively. It seems that both helicities tend to agree with each other, producing similar results.

The figures 6.20 and the more general ones according to different molecular orientations as maps 6.21 connect the distributions of $cos(\alpha)$ and the mean value of it with the direction from which the light encounters the molecular system. The generalised picture of the achiral formic acid and the direction of the light are presented in figure 6.22 [51].

The observed emission angles subsequent to the Coulomb explosion provide evidence that, under certain molecular orientations relative to the plane of polarisation of the incident light, the H_1 and H_2 atoms are deflected from the molecular plane. Visual evidence of this deflection is demonstrated through the following diagrams 6.23 depicting the complete breakup pathway. These illustrations affirm that, in the pyramidalization configuration, both the H1 and H2 atoms are deviated from the plane. This observation aligns well with the molecular equilibrium structure predicted through quantum chemical computations when the molecule undergoes

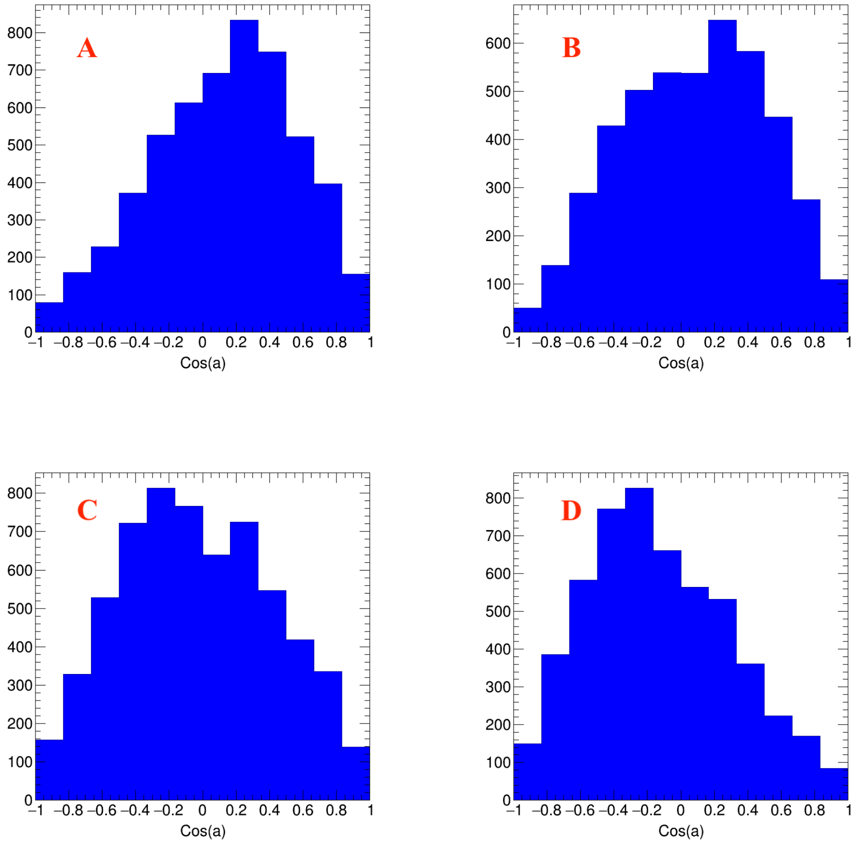

Figure 6.20: Calculation of handedness for different molecular orientations regarding the $cos(\theta)$ and ϕ in the molecular frame in the case of photoionisation by a circular polarised light at photon energy 305.5 eV. A: $\phi = [0, 36]$ and $cos(\theta) = [-1.0, -0.6]$, B: $\phi = [-36, 0]$ and $cos(\theta) = [-0.6, -0.2]$, C: $\phi = [-180, -144]$ and $cos(\theta) = [0.6, 1.0]$, D: $\phi = [-72, -36]$ and $cos(\theta) = [0.6, 1.0]$

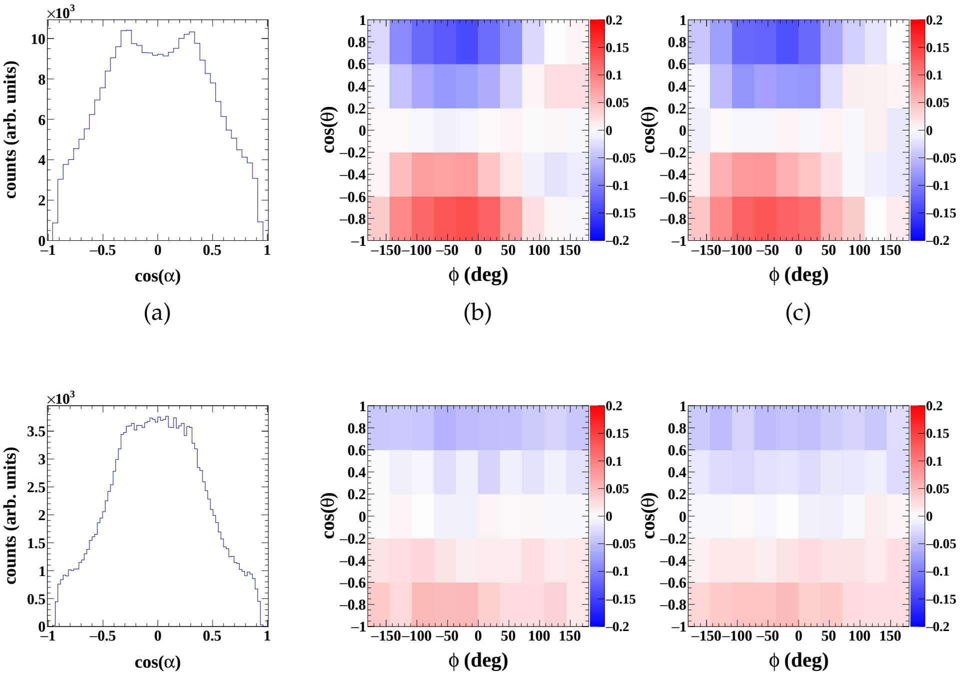

(a) (b) (c)

(d) (e) (f)

Figure 6.21: Handedness or chiral angle in the case of photoionisation by circular polarised light: photon energy at 305.5 eV (first row) leading to a photoelectron of 10 eV and photo energy at 311.0 eV (second row), leading to a photoelectron of 16 eV. Left column: calculation of chiral angle integrated over all directions. Centre: mean value of chiral angle in the MF as a function of $cos(\theta)$ and ϕ by LCP. Right: mean value of chiral angle in the MF as a function of $cos(\theta)$ and ϕ by RCP.

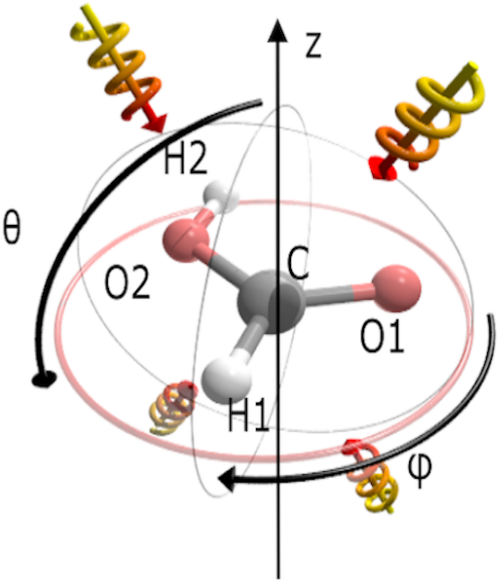

Figure 6.22: Enantioselective fragmentation of formic acid. Center: Achiral formic acid in syn-conformation. The arrows in the figure represent the different directions of the incoming light. The angles $cos(\theta)$ and ϕ are calculated in the molecular frame [51].

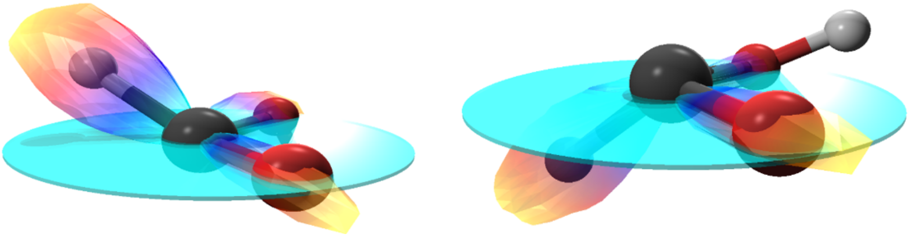

Figure 6.23: Chiral structures of formic acid. The ball-and-stick model indicates the direction of the linear momentum vectors, and the transparent lobes represent the measured data; the distance from the C atom and colour shows the count rate in the respective direction. The $O - C = O$ plane is highlighted in turquoise. Left: R enantiomer. Right: S enantiomer. The achiral structure of the molecule is presented in figure6.22. [51]

excitation from the n state to π^* excited state [51].

For the case of producing a photoelectron with a kinetic energy of 10 eV, the photoelectron was projected at the fragmentation frame of the three body breakup channel. The MFPAD technique helps us to gain access in the structure of the molecule by this projection. Below the results of the two enantiomers are presented, while for an increase of the statistics the results for the different helicity were added. The figure 6.24 shows the structure of the molecule, which confirms the chirality formation of it. The finding, with taking also into account the results from the calculation of the handedness, shows that the molecule has a chiral structure at the instance of ionisation. The very similar procedure was also followed by the photon energy at 311.0 eV with a photoelectron of kinetic energy 16 eV. Therefore, the results of two enantiomers are presented in figure 6.25, showing the structure of the molecule.

For the calculation of the MFPADs, several things were taken into account. Firstly, a condition in the energy of the electron was established. The reason was to exclude any other possible electron and focus only on the photoelectron. That means that at photon energy 305.5 eV, a range in the electron kinetic energy from 5 eV up to 15 eV was used. At photon energy 311 eV, a range in the electron kinetic energy from 10 eV up to 21 eV was used. The next step was to distinguish the enantiomers based on the handedness. For that purpose, a condition in the chiral angle larger than 0.25 or $cos(\alpha) > 0.25$ led to the R enantiomer and a condition in the chiral angle smaller than -0.25 or $cos(\alpha) < -0.25$ led to the S enantiomer. For every enantiomer, the final results include both helicities of the circular polarised light. Every enantiomer is the mirror image of the other one.

In figure 6.26, the calculation of the chiral angle is presented. The left panel belongs to the photon energy 305.5 eV and the right panel belongs to the photon energy 311 eV. The applied condition for the chiral angle is between -0.2 and 0.2. The expected result is symmetrical around zero since this

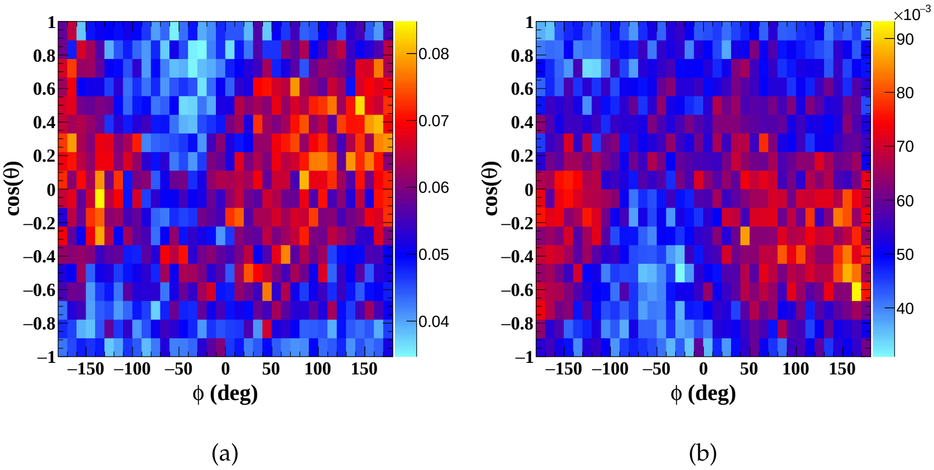

(a)

(b)

Figure 6.24: MFPAD histograms for the R (left) and S (right) enantiomer at photon energy 305.5 eV and photoelectron 10 eV. The S enantiomer is the mirror image of the R enantiomer, and vice versa. A condition for the choice of the enantiomers is applied based on the chiral angle. R enantiomer (left): $cos(\alpha) < -0.25$ and S enantiomer (right): $cos(\alpha) > 0.25$. Both helicities are presented at every enantiomer.

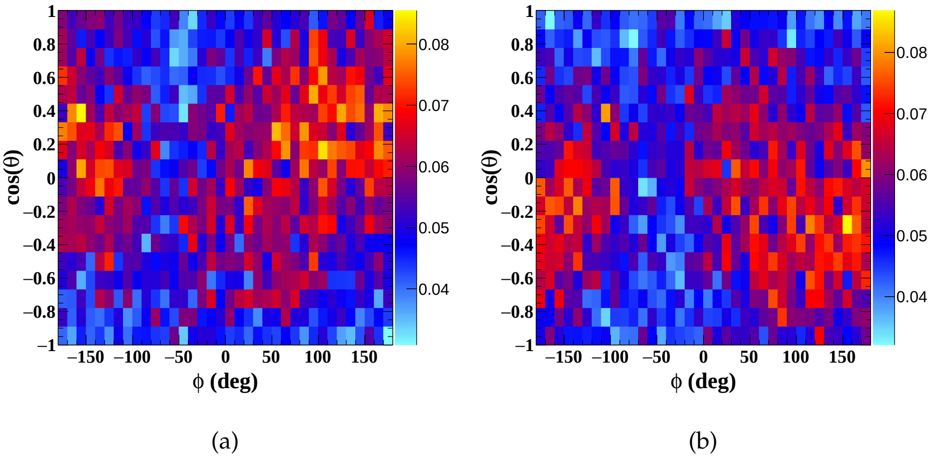

(a)

(b)

Figure 6.25: MFPAD histograms for the R (left) and S (right) enantiomer at photon energy 311.0 eV and photoelectron 16 eV. The S enantiomer is the mirror image of the R enantiomer, and vice versa. A condition for the choice of the enantiomers is applied based on the chiral angle. R enantiomer (left): $cos(\alpha) < -0.25$ and S enantiomer (right): $cos(\alpha) > 0.25$. Both helicities are presented at every enantiomer.

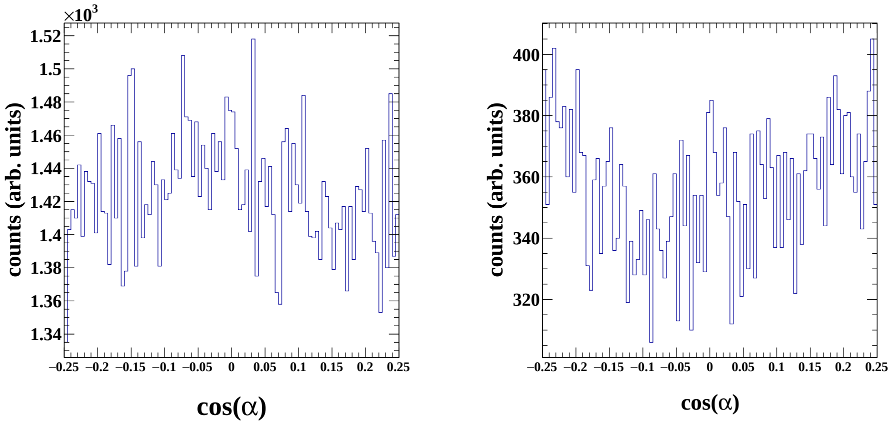

(a)

(b)

Figure 6.26: Calculation of handedness at photon energy 305.5 eV (Left) and 311.0 eV (Right) by circular polarised light. Selection of events by gating the handedness between −0.25 and 0.25.

region belongs to no preferable enantiomer.

6.3 CALIBRATION OF FORMIC ACID

The analysis of the formic acid was performed after the calibration with the use of the CO molecule. In addition to that, the electric field and the detector calibration also yielded based on the CO molecule. The process was a photoionisation with a photon energy 311.0 eV, as shown in equation 6.6,

$$\gamma + CO \rightarrow C^{*}O \rightarrow C^{+} + O^{+} + e^{-}_{\gamma} \tag{6.6}$$

$$\tag{6.7}$$

The binding energy of the 1s orbital of carbon is 311.0 eV, which leads to a photoelectron of 15 eV. The corresponding spectra for the photoelectron are shown in Figure 6.27. The calibrated spectra for the ions are shown in Figure 6.28.

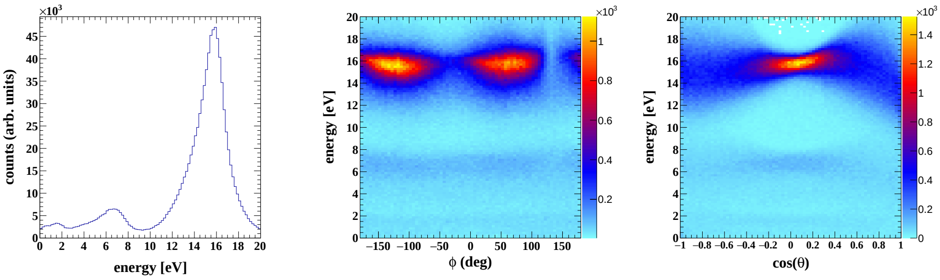

(a) (b) (c)

Figure 6.27: Calibrated electron spectra for the molecule CO at photon energy 311.0 eV.

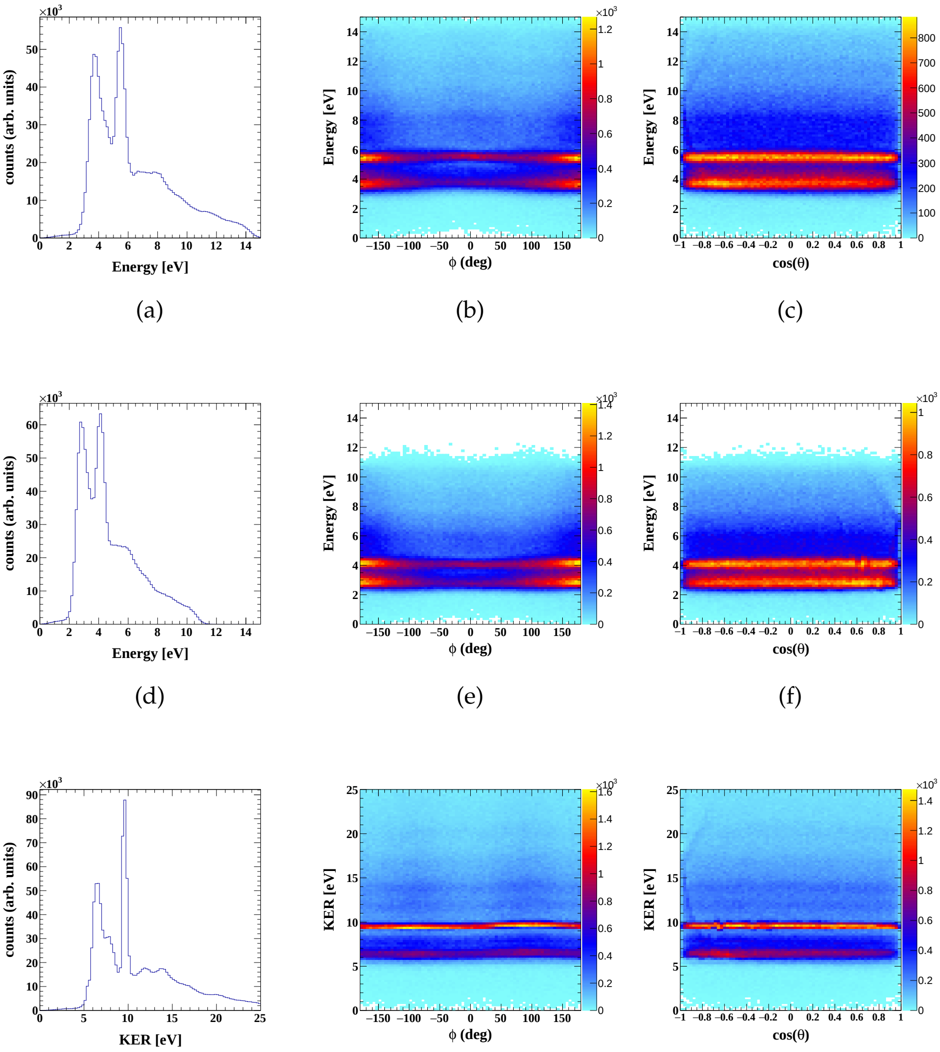

(a) (b) (c)

(d) (e) (f)

(g) (h) (i)

Figure 6.28: Calibrated ion and KER spectra for the molecule CO at photon energy 311.0 eV.

6.4 EXPERIMENTAL PARAMETERS OF FORMIC ACID

In this part, the basic parameters of the experimental setup are presented for convenience, based on the information in chapter 4, describing all the necessary parameters in the different experiments. The measurements were performed at the permanent COLTRIMS Endstation of beamline *P*04 of the PETRA *III* Synchrotron at DESY, Hamburg in October 2020 and June 2021. The synchrotron ring was operated in 40 bunch timing mode, which corresponds to a time spacing of 192 ns between photon bunches. The full information is presented in the following tables 6.2 and 6.3.

Spectrometer		
Electron arm	12cm	
Ion arm	17cm	
E-field	160 V/cm	
B-field	0	
Voltages		
Electron Detector	+1015V(front)	+3242V(anode)
Ion Detector	-3715V(front)	-1208V(anode)
Spectrometer	+1039V(electron side)	-3665V(ion side)
Detectors		
Electron	80mm	
Electron MCP	regular	
Ion	80mm	
Ion MCP	regular	
Rates		
Electron	33.5 kHz	
Ion	35 kHz	

Table 6.2: Experimental Setup November 2020 for the molecule formic acid.

Spectrometer		
Electron arm	7.0cm (acceleration), 12.0cm (drift)	
Ion arm	13.0cm (acceleration)	
E-field	125 V/cm	
B-field	7.6 G	
Voltages		
Electron Detector	+564V(front)	+2916V(anode)
Ion Detector	-2401V(front)	+93V(anode)
Spectrometer	+813V(electron side)	-1624V(ion side)
Detectors		
Electron	80mm	
Electron MCP	regular	
Ion	80mm	
Ion MCP	regular	
Rates		
Electron	14.8 kHz	
Ion	18 kHz	

Table 6.3: Experimental Setup June 2021 for the molecule formic acid.

7

PHOTOIONISATION OF OXYGEN

7.1 PHOTOIONISATION OF OXYGEN

In the next chapters of the analysis, we present experiments at high photon energies, by targeting the core shell of a diatomic and a polyatomic molecule in order to understand the origin (i.e., the underlying process) of multiple ionisation of these molecules after absorption of a single photon. In the following analysis, oxygen O_2 was chosen as the diatomic molecule, and the isopropanol C_3H_8O as the polyatomic one. In more detail, the goal was to extract electron energy coincidence maps from the measured data, which allow to identify the different ionisation mechanisms occurring under interaction of the molecule with circularly polarized light. Furthermore, a comparison among three different experimental scenarios was performed by collecting data using a synchrotron facility as well as an X-ray free-electron laser. In the first and second case, data from the PETRA III synchrotron facility recorded using a high magnetic field, and at a low magnetic field was recorded. Last but not least, data from an X-ray free-electron laser facility, the European X-ray free-electron laser was also analysed.

Building on the methods presented in the previous chapters on formic acid, i.e., structure determination via Coulomb explosion of the molecule and/or via measuring electron angular distributions in the molecular frame of reference, we target in this part of the thesis as a first step a simpler molecule, namely O_2.

The above-mentioned methods require both the generation of several charges inside the molecule under study. The measurement of MFPADs requires in addition the occurrence of a clean and energetically well-defined photoelectron. Previous studies have shown, that these prerequisites are in many cases not easy to fulfil when using a synchrotron (and thus single photon ionisation of the molecule) for the measurements.

In order to create several charges in a single photoionisation event, the following mechanisms are available:

A) As a core shell is ionised, an Auger decay may happen leading to the generation of one more charge. This is the most probable channel occurring in O_2. It is summarised in Eq. 7.1. Less probable, but along the line of Eq. 7.1 is the occurrence of an Auger cascade. Here more than one Auger electron is emitted in the deexcitation process.

B) A direct double ionisation can occur, in which two electron are emitted after the absorption of a single photon. At high energies the underlying process is typically that of a shake-off (but binary encounter-like double ionisation (typically called TS1) is possible, as well). The single photon double ionisation is shown in Eq. 7.2.

Combinations of A) and B) are possible, as well. In this case even higher charge is generated, as for example, an Auger decay occurs subsequent to a direct double ionisation, as indicated in Eq. 7.3. It is, as well, possible that the Auger electron ejection triggers the emission of a further electron along the shake-off and TS1 concept.

$$O_2 + \gamma \rightarrow O_2^{+*} + e_\gamma \rightarrow O_2^{2+} + e_\gamma + e_A \tag{7.1}$$

$$O_2 + \gamma \rightarrow O_2^{2+} + 2e_\gamma \tag{7.2}$$

$$O_2 + \gamma \rightarrow O_2^{3+} + 2e_\gamma + e_A \tag{7.3}$$

e_γ indicates the photoelectron and e_A is the Auger electron. The above-mentioned processes involve interactions of the formation of double- and triple-charged ionisation of the diatomic molecule. In the case of employing a synchrotron, the generation of high charged states of the diatomic molecule of oxygen result in a scenario which is problematic for the measurement of MFPADs. In direct double ionisation the two emitted electrons share the available kinetic energy. Thus, a double ionisation event does not yield a photoelectron with a distinct, well-defined kinetic energy, but rather a broad energy distribution. Such electrons cannot be used for the extraction of structural features of a molecule, as this extraction requires a well-defined electron wave length.

In comparison, when using a XFEL which provides photons at much higher intensity, the higher charged channels can produce energetically well-defined photoelectrons via the process of multi-photon absorption and ionisation. The multi-photon processes from FELs can enable the measurement of MFPADs even for much higher charge states as compared to the single-photon processes. This is particularly intriguing feature when considering a study of even larger molecules using the Coulomb explosion and MFPAD-approach.

The PIPICO spectra for the high magnetic field measurement is presented in figure 7.1, showing various breakup channels used in the following analysis. A corresponding PIPICO spectrum was obtained for the low magnetic field measurement, as well, using the respective experimental parameters, as presented in section 7.2. As shown in figure 7.1, the main breakup channel with the highest statistics belongs to the formation of

O^+O^+, which was also used for the calibration of the oxygen data. The second most abundant channel was the O^+O^{++}, located next to the first channel O^+O^+, the further channels ($O^{++}O^{++}$, O^+O^{+++} and $O^{++}O^{+++}$) were identified, as well, using the knowledge of the times-of-flight of the first channels, using the O^+ and O^{++} ions, and making a mass-charge ratio calibration.

The calibrated results are presented below for both measurements including fully high and low energy electrons. At the beginning, the ions are presented, and after that the electrons, which played a significant role in this analysis. In figure 7.2, the corrected ion data are presented for the high-magnetic-field dataset. Furthermore, the calibrated results for the low-magnetic-field campaign are presented in figure 7.3, as well.

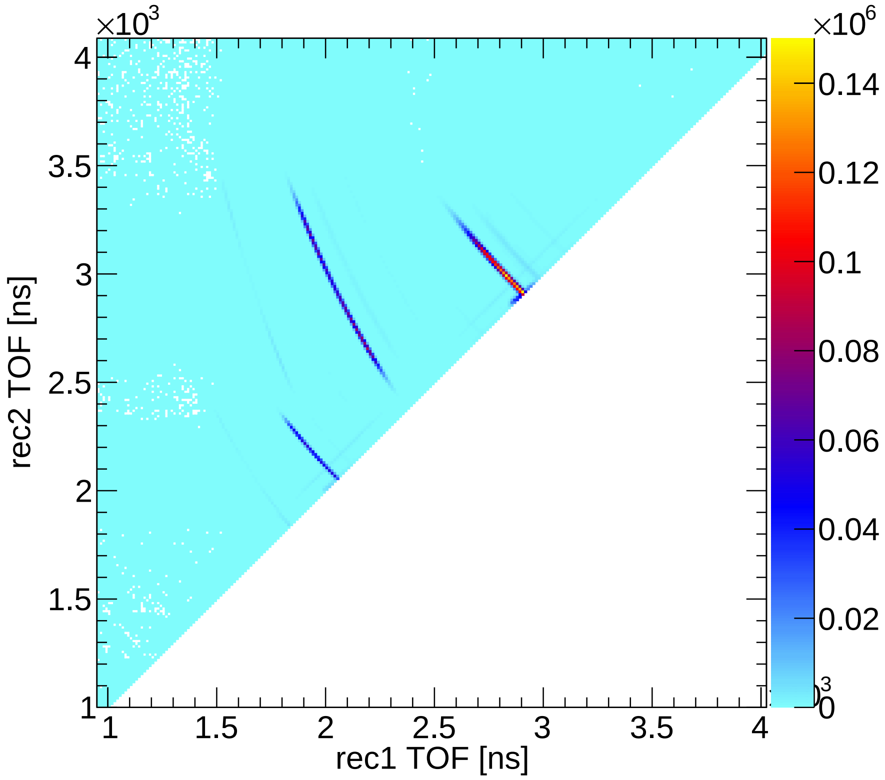

Figure 7.1: PIPICO spectrum of the O_2 molecule after the interaction with a photon of an energy of 670 eV. The data shown was recorded with the high magnetic field setting with $B = 42$ Gauss. The strongest contribution at TOF 2905 ns for both the first and the second ion, belongs to the O^+O^+ channel. Going forward the second line at TOF1 2905 ns and TOF2 around 2100 ns is identified as the O^+O^{++}. The third one at TOF1 and TOF2 around 2100 ns is $O^{++}O^{++}$. The fourth one with TOF1 at 2905 ns and TOF2 1665 ns is O^+O^{+++}. The last one, which is not very clear in the pipico spectrum, is a breakup into $O^{++}O^{+++}$ with TOF1 at 2100 ns and TOF2 at 1665 ns.

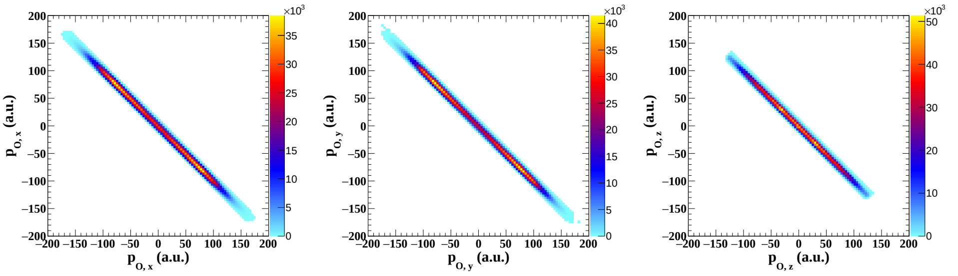

(a) (b) (c)

Figure 7.2: High magnetic field: the final correlations between the measured moment of the two ions of the strong breakup channel O^+O^+. As expected, the shape of the plot shows a diagonal line for all three momentum components of ion1 and ion2, after the calibration of the ion detector as well as extra corrections to the momentum.

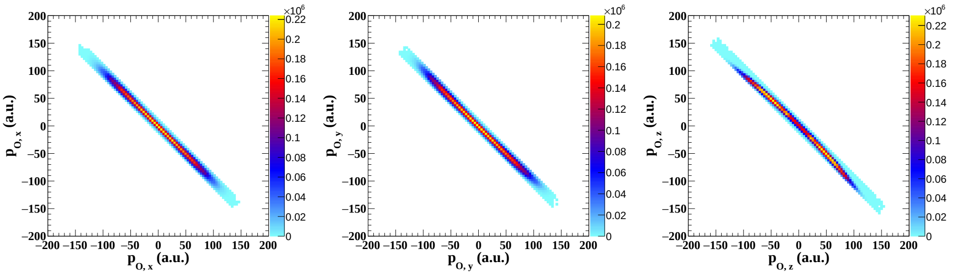

(a) (b) (c)

Figure 7.3: Low magnetic field: the final correlations between the measured moment of the two ions of the strong breakup channel O^+O^+. As expected, the shape of the plot shows a diagonal line for all three momentum components of ion1 and ion2, after the calibration of the ion detector as well as extra corrections to the momentum.

The main point of this analysis is the inspection of electrons, which were measured in coincidence, as is already mentioned above. The next plots present the electron calibration measurement along with some basic electron plots to identify the measured electrons for both magnetic field settings. In figure 7.4, the spectrum of the photoelectron recorded using a photon energy of 670 eV along with the Auger electron energy distribution belonging to a decay of the ionised $1s$ orbital is presented. The dataset shown here was acquired using the high magnetic field setting.

The expected photoelectron energy can be calculated as based on the formula $E_e = PhotonBeam - BindingEnergy$, leading to a photoelectron of kinetic energy of 127 eV. In figure 7.5, the corresponding spectra are shown, which were obtained from low magnetic field dataset. The photoelectron occurs in both cases (as expected) at the same kinetic energy. The big difference is the elimination of the Auger electron due to the low magnetic field. Nevertheless, in comparison with the high magnetic field case, there is a significant gain in resolution. Another interesting phenomenon is the extra feature in the electron energy spectrum of figure 7.5 at energy 100 eV. This extra distribution belongs to a shake-up process, in which the original photoelectron loses some of its energy, approximately 25 eV, and this energy was used to excite another electron. In general, this process leads to extra peaks, which take place in lower kinetic energies of a peak of a photoelectron.

The same calibration processes of the electron side of the spectrometer are applied to all the different ionic break-up channels. The results are consistent with the main breakup channel O^+O^+, as it has already been presented in the above figures 7.4 and 7.5, for the two different cases of the magnetic field.

The motivation is to obtain a detailed understanding how higher charge states (i.e., the break-up channel beyond O^+O^+) are generated in case of the single photon-ionisation using the synchrotron. Based on that concept, the idea was to construct electron coincidence maps.

The coincidence maps depict the energy of one of the measured electrons in dependence of the energy of another detected electrons. These maps were generated for all the aforementioned break-up channels. In the case that more than two electrons were detected, all combinations of electrons are sorted in the corresponding coincidence maps. In the case of the low B-field, the high energy Auger electron was not detected. Therefore, only one electron was measured for the O^+O^+ break-up channel and correspondingly the electron coincidence map is omitted for this case.

In the next figures, the electron maps are presented for both cases, detection of high-and low-energy electrons, which were recorded in the synchrotron

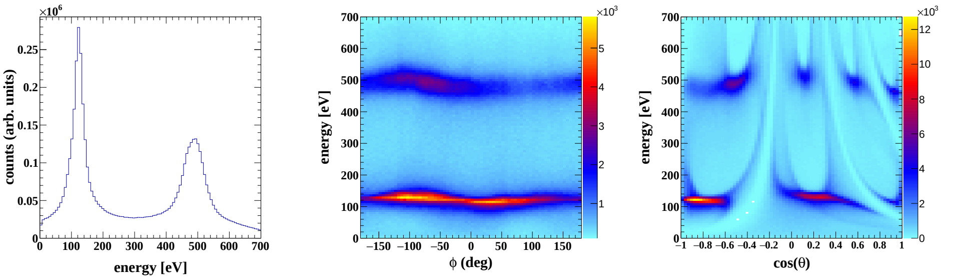

(a) (b) (c)

Figure 7.4: Measured photoelectron energy (high B-field dataset). The plots show the photoelectron at 127 eV kinetic energy, after targeting the K shell of the oxygen and the Auger electron at a mean kinetic energy of 497 eV. The examined channel is the O^+O^+.

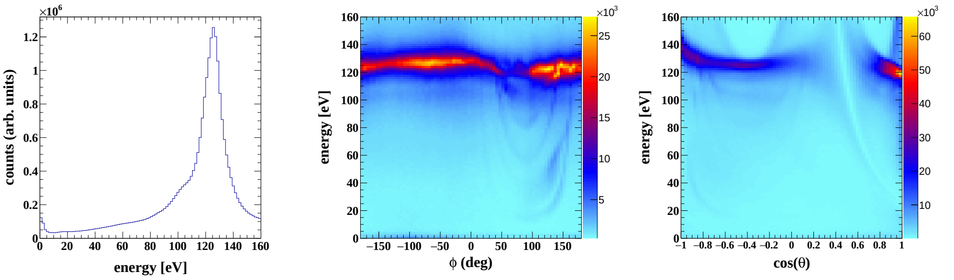

(a) (b) (c)

Figure 7.5: Measured photoelectron energy (low B-field dataset). The plots show the photoelectron at 127 eV kinetic energy, after targeting the K shell of the oxygen. The examined channel is the O^+O^+. The low B-field offers a better resolution in the detection of low energy electrons.

experiment at DESY. These are followed by a comparison with the data acquired at the X-ray free-electron laser. The analysis consists of different breakup channels of the O_2 diatomic molecule. The breakup channels for this specific analysis were the O^+O^+, O^+O^{++}, $O^{++}O^{++}$, O^+O^{+++}, and $O^{++}O^{+++}$, with the last two ones suffering from low statistics. The $O^{++}O^{+++}$ breakup channel was excluded from the comparison between the two magnetic fields. Figure 7.5 presents the comparison between high-magnetic-field and low-magnetic-field measurements, covering the above-mentioned breakup channels.

In Figure 7.5a, the electron coincidence map for the break-up channel of the molecule into $O^{+}O^{+}$ is shown. The strongest contribution belongs to the coincident detection of an O - K shell photoelectron and its corresponding K-Auger electron, yielding the two peaks at energies 127 eV and 490 eV, respectively. They are not in addition to that faint features which belong to false coincidences, most prominently at an energy pairing of 490 eV and 490 eV. The comparably strong horizontal and vertical lines are most probably caused in many cases by a combination of a real photoelectron with random background electrons.

As the overall charge state of the molecule increases (from the top part to the bottom part of figure 7.5), a general trend is visible. The intensity of the distinct photoelectron line at 127 eV decreases (see right column of figure 7.5, i.e. the low energy results) and more low energy electrons are created. Accordingly, the high energy measurements (left column of figure 7.5) shows a decrease of K-electron/Auger-electron pairs. This is a clear indication, that either Auger cascades or direct double ionisation processes become more dominant. As mentioned above, the latter decrease the clean K-photoline signal, as (in case of direct photo double ionisation) the excess energy is shared between the two emitted electrons. In case of Auger cascades or double ionisation events from the Auger decay, an enhancement of low energy electrons is a very probable behaviour. The low energy measurement belonging to the $O^{+}O^{++}$ break-up channel (7.5c) depicts directly the occurrence of direct photo double ionisation: a faint diagonal line is visible at a sum energy of close to 100 eV. If the two emitted electrons share the excess energy, the coincidence-events will appear at a sum energy of $E_{sum} = hv - E_{bind1} - E_{bind2}$, with E_{bind1} and E_{bind2} being the binding energy of the two electrons. In this case, a K-electron was emitted together with an electron from the valence shell, as the decrease of the sum energy by approximately 20 eV to 40 eV indicates.

In particular, figure 7.5 demonstrates for a simple, small molecule the common trend that the generation of high charge states by means of absorption of a simple photon yields a loss of the primary photoelectron in the electron energy spectrum. While Coulomb explosion imaging approaches are still possible in this scenario, the measurements of distinct MFPADs for photoelectron diffraction imaging cannot be performed anymore under these conditions.

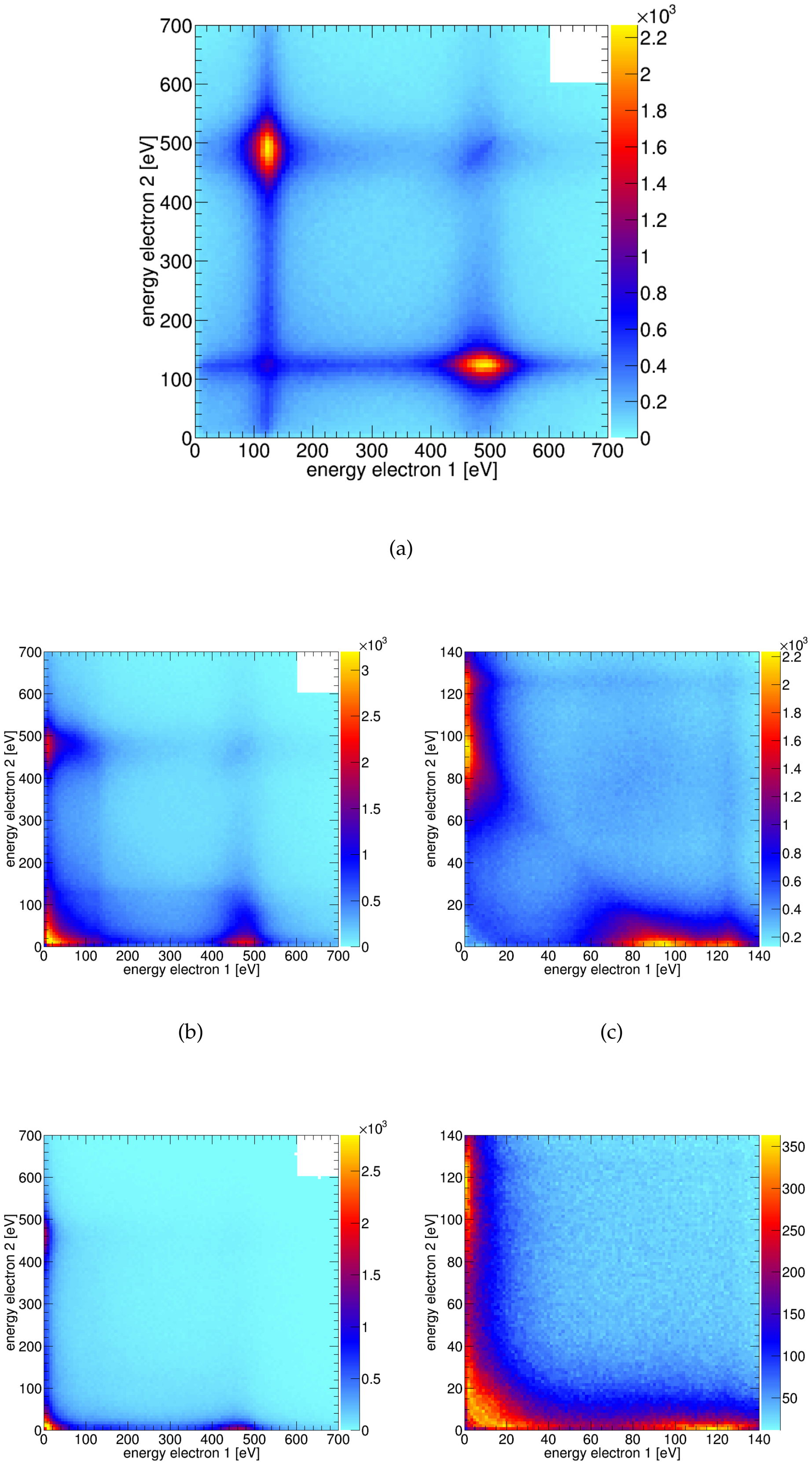
energy electron 1 [eV]
energy electron 2 [eV]
0
100
200
300
400
500
600
700
×10³
0
0.2
0.4
0.6
0.8
1
1.2
1.4
1.6
1.8
2
2.2
0.5
1.5
2.5
3
20
40
60
80
120
140
50
150
250
350

(a)

(b)

(c)

(d)

(e)

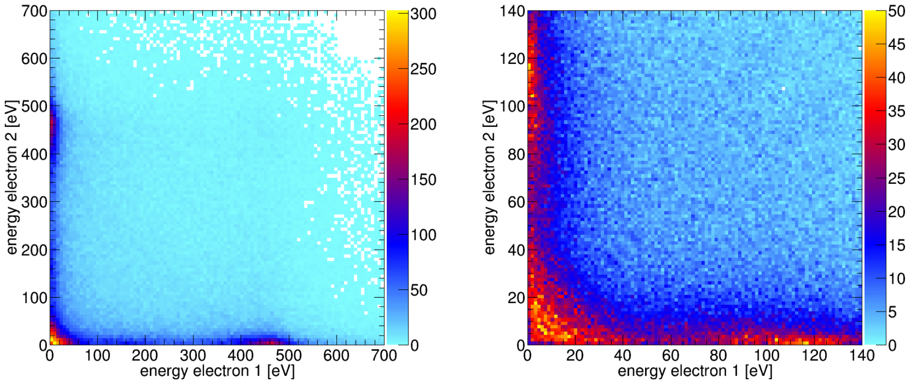

(f) (g)

Figure 7.5: Coincidence maps of the measured electrons at photon energy 670 eV: Left: Data recorded at PETRA III at $B = 42$ Gs (Auger electron at 500 eV). Right: Data recorded at PETRA III at $B = 20$ Gs (no Auger electron). Top - Bottom: Increase in total charge of the break-up channels: panel b and c : $O^{+}O^{++}$, panel d and e : $O^{++}O^{++}$, panel f and g : $O^{+}O^{+++}$. The first row shows the $O^{+}O^{+}$ breakup channel with a photoelectron at 127 eV (Auger electron at 500 eV) as recorded in the case of high magnetic field.

Furthermore, a comparison between synchrotron and free electron laser light sources for the ionisation of the molecule using photons of the same photon energy of 670 eV was performed. The major difference is that the synchrotron produces a less intense photon beam, which allows only for the absorption of a single photon (i.e., multi-photon processes can be neglected). In figure 7.5, the final results after the calibration processes are presented. As indicated in the figures, I think it makes more sense to use the low energy measurement here instead of the combined datasets. (The XFEL data covers the same energy range as the low magnetic field measurement.)

Figure 7.5 shows in the left panels the coincidence maps obtained at Petra III, while in the right panels the corresponding results from the European XFEL are shown. The rows depict the coincidence electron maps for the break-up channels $O^{+}O^{++}$, $O^{++}O^{++}$, $O^{+}O^{+++}$, and $O^{++}O^{+++}$ (top to bottom). The results obtained for a break-up channel into $O^{+}O^{++}$ seem to look very similar at first glimpse. Looking at the two panels in more detail reveals that the K-photoelectron peak is more pronounced in the dataset recorder at the XFEL. This could be a first indication of a multi-photon absorption process (i.e., the absorption of two photons) in combination with only a single Auger decay (in order to yield the total charge of three in the end). As the total charge increases, it becomes more evident, that the higher charge states are created indeed by absorption of more than

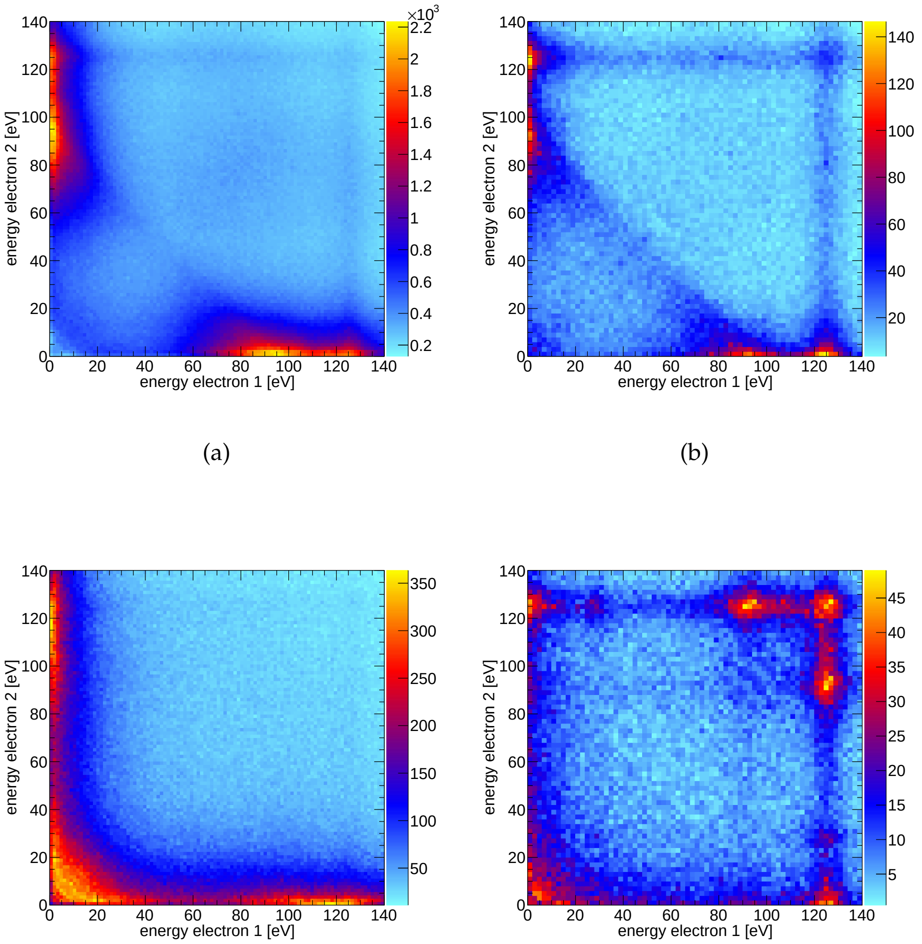
energy electron 1 [eV]
energy electron 2 [eV]
0
20
40
60
80
100
120
140
×10^3
0.2
0.4
0.6
0.8
1
1.2
1.4
1.6
1.8
2
2.2
20
40
60
80
100
120
140
50
100
150
200
250
300
350
5
10
15
20
25
30
35
40
45

(a)

(b)

(c)

(d)

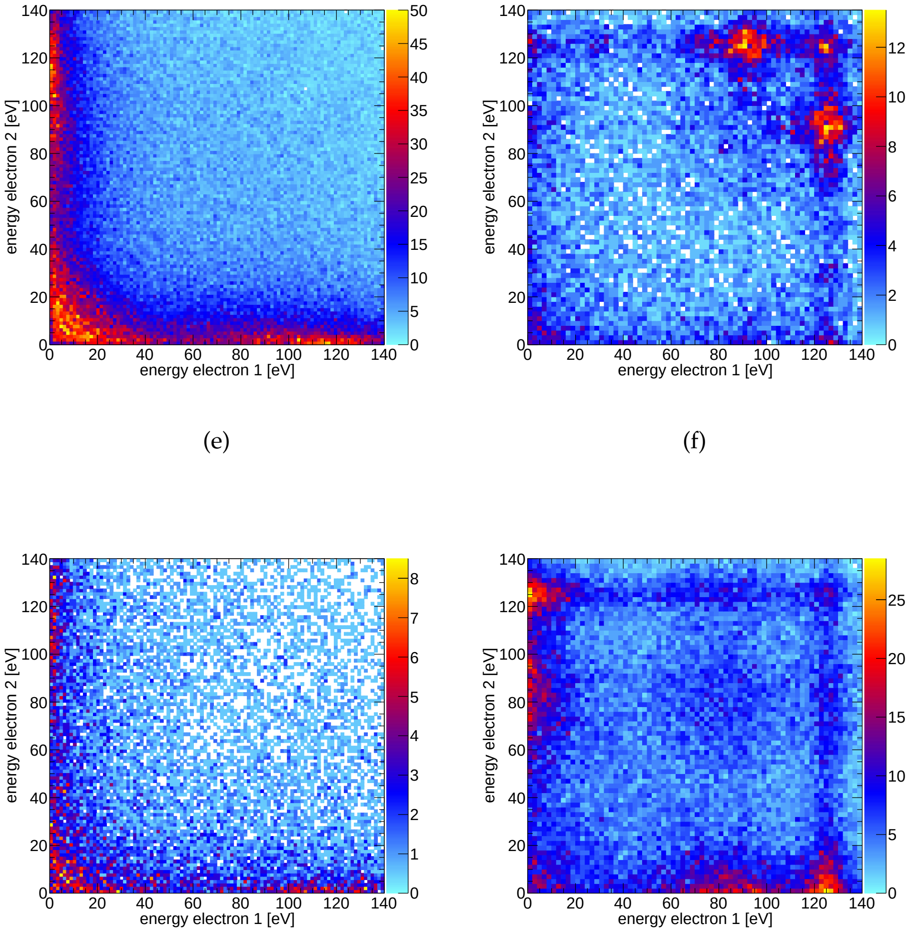

(e)

(f)

(g)

(h)

Figure 7.5: Coincidence maps of the measured electrons: Left: Data recorded at the PETRA III. Right: Data recorded at the EU-XFEL. Top - Bottom: Increase in total charge of the break-up channels: panels a and b: $O^{+}O^{++}$, panels c and d: $O^{++}O^{++}$, panels e and f: $O^{+}O^{+++}$ and panels g and h: $O^{++}O^{+++}$.

one photons when using the XFEL light for the ionisation. The panels belonging to a fragmentation of the molecule into $O^{++}O^{++}$ show strongly peaked features and fewer low energy electrons when comparing the XFEL data to the synchrotron results. In particular, the main K-photoline is still present and two additional peaks at electron energy of approximately 30 eV and 95 eV appeared in the XFEL measurement. These two new peaks belong to the formation of single-site double core holes and the sequential multiple ionisation of the K-shell, as shown recently by Kastirke et al. [77].

The results for a break-up into $O^{+}O^{+++}$ confirm this finding. There the aforementioned peak at approximately 95 eV is even more pronounced and the K-photoline is still strongly visible, as well. Due to the nature of this breakup channel, which involves the local creation of a second K-hole at one of the two oxygen atoms in cases where the molecule already started to fragment, the sequential K-ionisation is dominant over double core-hole creation. The results for the $O^{++}O^{+++}$ channel depict a strong K-photoline and a broader peak located at approximately 80 eV. The latter was identified to be caused by a double ionisation by the absorption of a second photon, which yields a broadening decrease in energy of the sequential K-ionisation peak at 95 eV. More details on this have been reported in the paper [78].

These findings nicely demonstrate, that employing a free-electron laser laws enables the generation of high charge states in combination with the occurrence of distinct well-defined peaks in the electron spectrum. Such energetically well-defined electrons are suitable for performing electron diffraction imaging and even time-resolved processes can be recorded under the conditions available at X-ray free-electron laser [79].

Three more datasets were recorded at photon energies 653 eV, 638 eV, and 573 eV. The results for the first one are consistent with those obtained at 670 eV and the two latter ones are slightly different due to a small change in the magnetic field. The breakup channels inspected for the above measurements were in full consistency with the aforementioned channels. In figure 7.6, the results recorded at a photon energy of 653 eV are shown. At this photon energy, the K-photoelectron has kinetic energy of approximately 115 eV. The figures 7.7 and 7.8 show the results for the other photon energies. The energy of the photoelectron was expected to be at around 100 eV in the first case and 30 eV in the latter case. The results show the ejection of the photoelectron via the process of a photoionisation along with the secondary process of shake-off, because of the extra features at the electron maps, leading to a double ionised molecule. The extra charge on those channels is the Auger electron, which was not measured during the beamtime because of the low magnetic field.

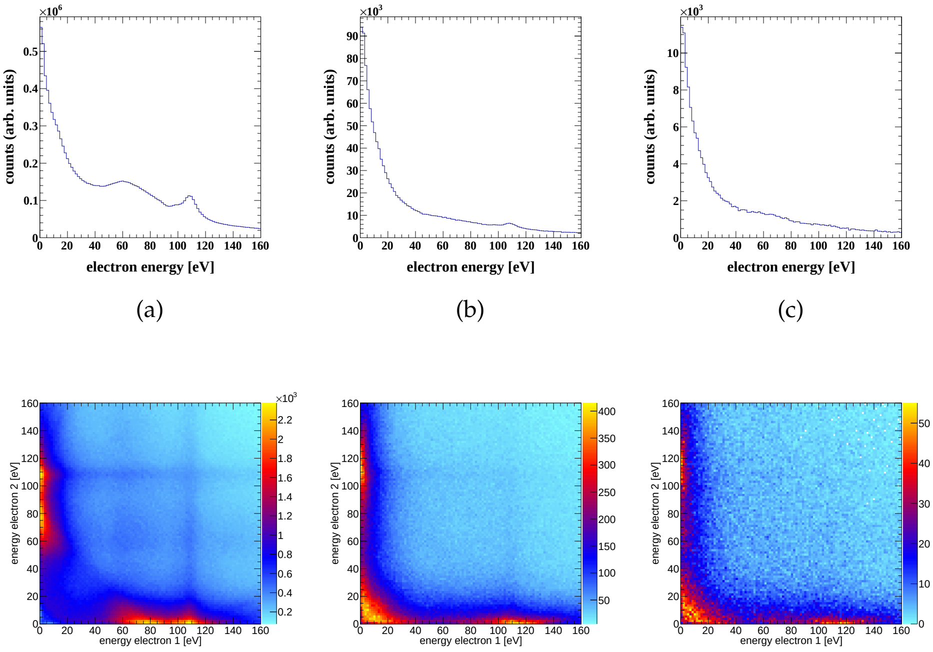

(a) (b) (c)

(d) (e) (f)

Figure 7.6: Results obtained at photon energy 653 eV focusing specifically on the electrons. The first row shows the electron energy spectra of $O^{+}O^{++}$ (left), $O^{++}O^{++}$ (centre), and $O^{+}O^{+++}$ (right) breakup channels, while the second row depicts the corresponding coincidence maps. The results are consistent with those obtained at a photon energy of 670 eV, while the breakup channel $O^{++}O^{+++}$ was excluded because of low statistics.

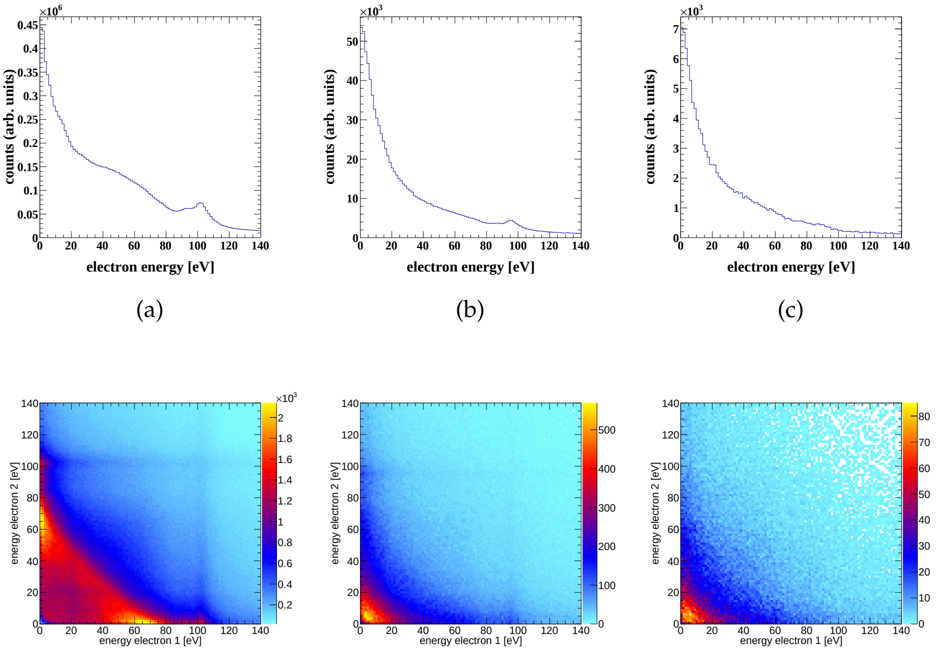

(a) (b) (c)

(d) (e) (f)

Figure 7.7: Results obtained at photon energy 638 eV focusing specifically on the electrons. The first row shows the electron energy spectra of $O^{+}O^{++}$ (left), $O^{++}O^{++}$ (centre), and $O^{+}O^{+++}$ (right) breakup channels, while the second row depicts the corresponding coincidence maps. The results are consistent with those obtained at photon energies of 670 eV and 653 eV, while the breakup channel $O^{++}O^{+++}$ was excluded because of low statistics.

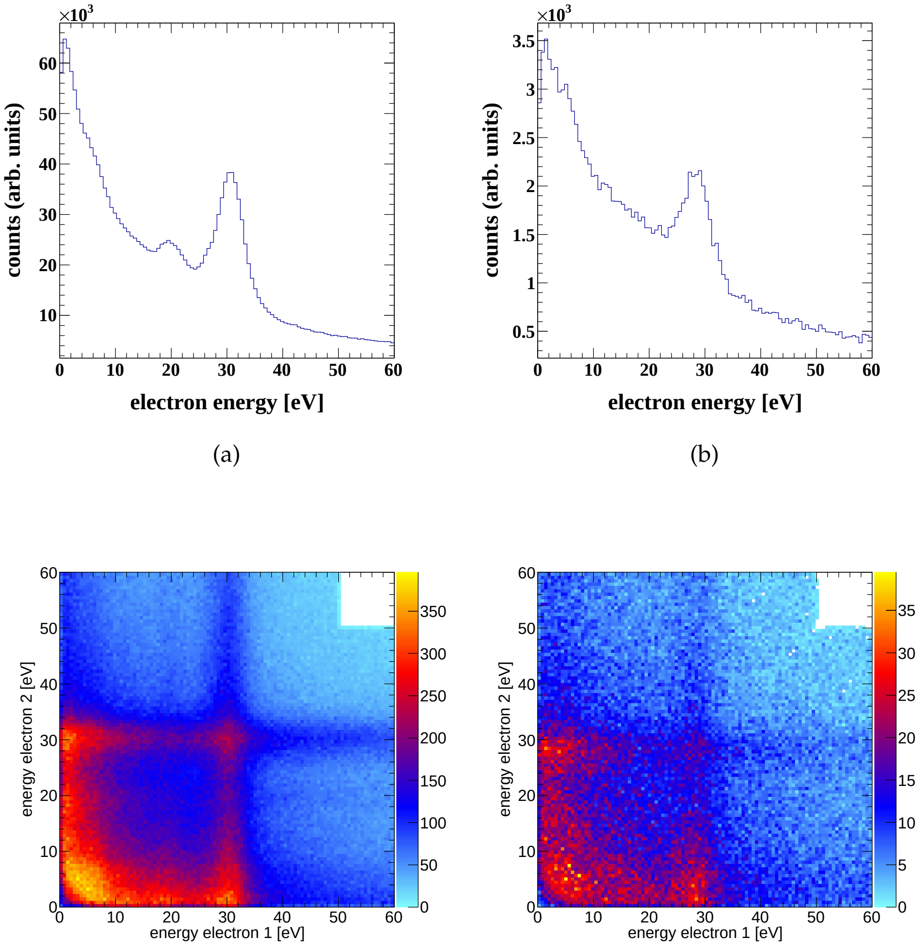

(a)

(b)

(c)

(d)

Figure 7.8: Results obtained at photon energy 573 eV focusing specifically on the electrons. The first row shows the electron energy spectra of $O^{+}O^{++}$ (left), and $O^{++}O^{++}$ (right) breakup channels, while the second row depicts the corresponding coincidence maps. The results are consistent with those obtained at photon energies of 670 eV, 653 eV and 638 eV, while the breakup channels $O^{+}O^{+++}$, and $O^{++}O^{+++}$ were excluded because of low statistics.

7.2 EXPERIMENTAL PARAMETERS OF OXYGEN MOLECULE

In this part, the basic parameters of the experimental setup are presented for convenience, based on the information in chapter 4, describing all the necessary parameters in the different experiments. The measurements were performed at the permanent COLTRIMS Endstation of beamline $P04$ of the PETRA III Synchrotron at DESY, Hamburg in April 2019 and August 2020. The synchrotron ring was operated in 40 bunch timing mode, which corresponds to a time spacing of 192 ns between photon bunches. The full information is presented in the following tables 7.1 and 7.2.

Spectrometer		
Electron arm	6.4cm	
Ion arm	17cm	
E-field	50 V/cm	
B-field	17.5 ns, 21.8 ns	
Voltages		
Electron Detector	-230V(front)	+2607V(anode)
Ion Detector	-2626V(front)	+174V(anode)
Spectrometer	-254V(electron side)	-1759V(ion side)
Detectors		
Electron	80mm	
Electron MCP	regular	
Ion	80mm	
Ion MCP	regular	
Rates		
Electron	14.5 kHz	
Ion	6 kHz	

Table 7.1: Experimental Setup April 2019 for the diatomic molecule O_2.

Spectrometer		
Electron arm	17cm	
Ion arm	4.5cm(acceleration) + 7.5cm(drift)	
E-field	50 V/cm	
B-field	42 G	
Voltages		
Electron Detector	+160V(front)	+2701V(anode)
Ion Detector	-2712V(front)	-303V(anode)
Spectrometer	+112V(electron side)	-1400V(ion side)
Detectors		
Electron	80mm	
Electron MCP	regular	
Ion	80mm	
Ion MCP	regular	
Rates		
Electron	35 kHz	
Ion	6.5 kHz	

Table 7.2: Experimental Setup August 2020 for the diatomic molecule O_2.

8

ELECTRON INTERACTIONS OF ISOPROPANOL

8.1 PHOTOIONISATION OF ISOPROPANOL MOLECULE

In this section, the aim is to expand the studies from the diatomic molecule oxygen to a bigger complex polyatomic molecule. For that purpose the molecule isopropanol was chosen. As in the case of the diatomic molecule oxygen, the idea was to measure low-energy electrons and high-energy electrons as well with the appropriate experimental configurations. Therefore, different settings concerning mainly the photon energy and the magnetic field were applied during the measurement. The structure of this molecule, isopropanol, is consisting of 3 carbons, 1 oxygen, and 8 protons. The geometry of this molecule is presented in the next figure 8.1.

In addition to extracting information on the ionization process of the molecule (after absorbing the synchrotron radiation) from the emitted electrons, details on the emitted ions are presented at the end of this chapter, as well. The latter provide insight into the fragmentation dynamics following the K-shell ionization. By exploring the powerful technique of Coulomb explosion Imaging (CEI), the results for two different breakup channels are presented.

We continue along the line of the previous chapter on oxygen and inspect emitted electrons of low- and high-energy. The parameters of the experiment to achieve this task are presented at the end of the chapter 8.3, including a comparison of the performed measurements. For the implementation of the measurements, magnetic fields of 13 Gauss and 42 Gauss were employed. The electrons of isopropanol can be ionised by using the proper photon energy, in order to to overcome the binding energy of the targeted shell. In the following table 8.1, the binding energies of the shells of the elements in the isopropanol molecule and the resulting electron kinetic energies are presented.

A first difficult part with respect to such a large molecule with many electrons is to identify the breakup channels and distinguish the generated fragment-ions in each break-up channel. This is particular demanding, as in many cases, the fragment-ions have a very similar mass-over-charge ratio. For example, they may differ only by a single proton. In the next figure 8.2, the PIPICO spectra are presented. In these spectra, a proper choice of possible candidates for two and three-body breakup channels appear. There are several fragmentation channels visible, but the idea was to

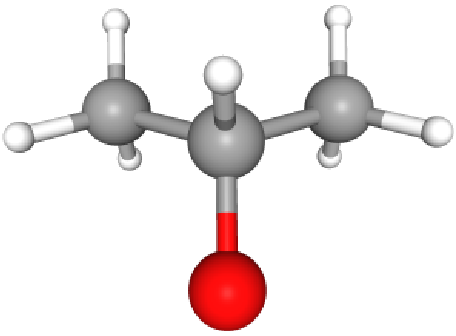

Figure 8.1: Depiction of the Isopropanol Conformer in a 3*D* representation. All the carbons with protons and oxygen are connected with single bonds among them. The mass of the molecule is 60 *gr*/*mol*.

electron state	Binding E[eV]	670.0 [eV]	600.0 [eV]	563.0 [eV]
O2s photoelectron	41.6	628.4	558.4	521.4
O1s Auger electron	-	500.0	500.0	500.0
C1s photoelectron	284.2	385.8	315.8	278.8
C1s Auger electron	-	250.0	250.0	250.0
O1s photoelectron	543.0	127.0	57.0	20.0

Table 8.1: Expected electron kinetic energies according to different electron orbitals and photon energies. The first column shows the targeted electron, the second column shows the binding energy of the desired orbital and the last three columns show the expected kinetic electron energies according to the specified photon energy.

choose the most promising ones, i.e., the ones with respect to good statistics.

An effort to extend the studies beyond three-body fragmentation was also performed. However, the statistics were very low, suggesting it is very unlikely to create (under the conditions of our experiment) very high charges in the molecule and corresponding fragmentation pathways. According to those plots, a clean identification of the mass and charge of the involved fragment-ions contributing to these channels is not possible. In many cases, the PIPICO spectra depict a concentration of several straight lines in certain region, which makes it hard to distinguish the individual break-up channels. This is a common feature occurring in studies of larger (and thus more complicated) molecules.

The red rectangular boxes present the potential two body- and three body-breakup channels. For the process of the identification of every charged

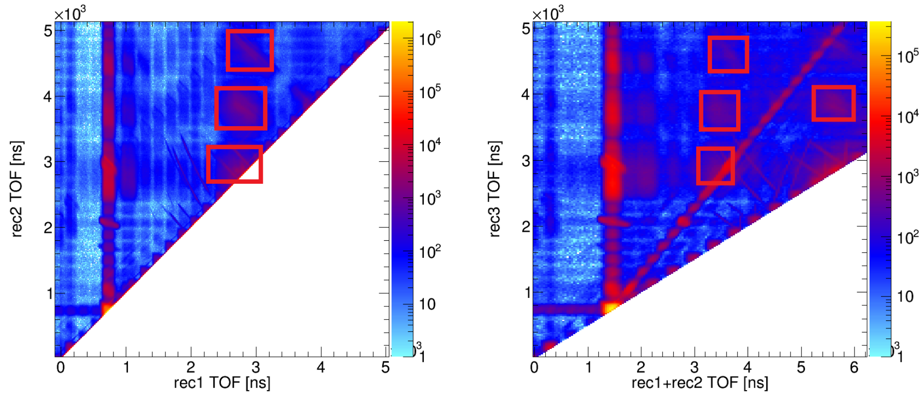

Figure 8.2: The pipico and the 3pico spectra employing the 670 eV photon energy (high $\vec{B}$) for the measurement. The red rectangles define regions of interest, in which the occurring fragment-ions have been identified and examined in more detail. All these breakup channels are incomplete ones, meaning that some parts of the molecule have not been detected in our experiment.

particle, a cross verification with the mass of each was performed. During that process, the calibration measurement provided a correlation between the mass and time-of-flight of every particle in order to acquire a better indication of the participating particles in the process.

The selected breakup channels of isopropanol are all incomplete ones. That means that in all cases some part of the fragmented molecule has not been detected. For that reason, the missing part of the molecule was assumed to be a neutral fragment in the analysis to construct the completed entity. In the left panel of the figure 8.2, the marked breakup channels have been identified as the $CH_3^+/CH_3^+/CH_2O$, at the bottom part of the plot, the $CH_3^+/C_2H_3^+/H_2O$, at the centre part of the plot, and the $O^+/C_3H_5^+/H_3$, at the top part of the plot. Furthermore in the right panel of the figure 8.2, the breakup channels are identified as $H^+/CH_3^+/CH_3^+/CHO$ at the bottom of the spectrum, as $H^+/CH_3^+/C_2H_3^+/OH$ at the middle left of the spectrum, as $H^+/O^+/C_3H_3^+/H_4$ at the top part of the spectrum, and as $CH_2^+/O^+/C_2H_4^+/H_2$ at the right centre of the spectrum.

The first part of the analysis is to produce the electron coincidence maps for the highest photon energy using the highest magnetic field, i.e., by employing a photon energy of 670 eV and a magnetic field close to 40 Gauss. In figure 8.3, the calibrated electron measurements are presented and in figure 8.4, the electron coincidence map is presented, showing the possible combinations of electrons emitted from the molecule. During the calibration, several breakup channels have been identified, keeping only those with the best statistics. The most promising breakup channels were the $CH_3^+/CH_3^+/CH_2O$ and $O^+/C_3H_3^+/H_5$, which resulted in using the latter one for simplicity and the fact that it includes all the heavy atoms of the molecule. In figure 8.3, the peaks in the electron energy spectrum, which is at the left panel of the figure, represent the main electrons, emerging from the different ionisation processes.

The first peak at energy 127 eV represents the photoelectron from the 1s orbital of Oxygen, the second peak in the row represents the K-Auger decay of Carbon, the third one shows the photoelectron from the 1s orbital of Carbon, and the last one the K-Auger decay of Oxygen. The middle and the right plot shows the measured electron energy in dependence of the azimuthal angle ϕ of the electrons in the laboratory frame and the polar angle $cos(\theta)$ of the electrons in the laboratory frame. In figure 8.4, the electron coincidence map of the corresponding breakup channel is shown, indicating which electrons are the main contribution to the ionisation process when employing a photon energy of 670 eV for the ionisation. The x-axis is the kinetic energy of first electron and the y-axis is that of second electron. The observable islands either strong or weak represent the possible ionisation pathways based on the measured electrons. In the electron map 8.4, a diagonal line shows with good resolution the main contribution in form of a combination of a photoelectron from K shell of oxygen with the K-Auger decay of oxygen, and the interaction between the photoelectron from the K shell of carbon with the K-Auger decay of carbon. Moreover, other possible electron combinations present, as well, such as the feature visible at electron energies 250 eV and 127 eV, corresponding to the photoelectron from the K shell of oxygen and the K-Auger decay of carbon. A less prominent feature appears at energies of 385 eV and 127 eV, belonging to the combination of photoelectrons from carbon and oxygen.

Expanding further the analysis, some other two body breakup channels are presented, using the same experimental settings like before. Another good statistics channel is that one with the identical ions CH_3^+ and CH_3^+, assuming a neutral part of CH_2O. The results for this fragmentation channel are presented in figure 8.5. The statistics in that channel is less as compared to that of the previously presented one. However, the electron coincidence map shows clean features, especially on the diagonal line. In this plot, several electron coincidence peaks are visible. Starting with the diagonal line, a signal appeared among the photoelectron from the K shell of oxygen at energy 127 eV, the K-Auger decay of carbon at energy 250 eV, the photoelectron from the K shell of carbon at energy 385 eV, and the K-Auger decay of oxygen at energy 500 eV. Thus, the diagonal line shows the combination of the photoelectron from K shell of carbon with the K-Auger decay of carbon, and the combination of the photoelectron from the K shell of oxygen with the K-Auger decay of oxygen. In addition to that, other signal combinations between the four above mentioned electrons can be observed. For example, the island at an energy of the

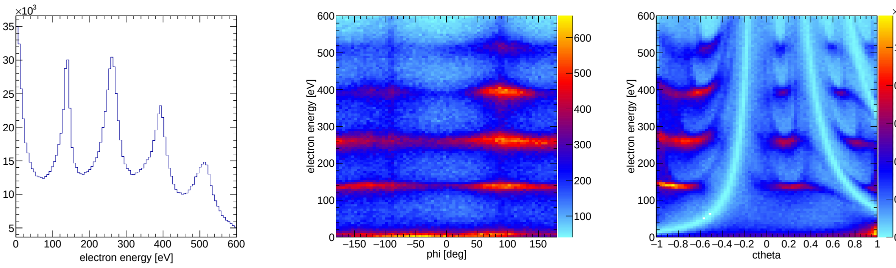

(a) (b) (c)

Figure 8.3: Calibrated Electron spectra in the case of using 670 eV photon energy and 40 Gauss magnetic field. The left panel depicts the electron energy spectrum, showing the photoelectron from Oxygen at 127 eV, the photoelectron from Carbon at 385 eV, the Auger 1*s* electron from Carbon at 250 eV and the Auger 1*s* electron from Oxygen at 510 eV. In the central panel, the electron energy as a function of the angle ϕ is presented and in the right panel the electron energy as a function of $cos(\theta)$ is shown up. The inspected incomplete breakup channel consists of O^+ and $C_3H_5^+$.

first electron of 250 eV and an energy of 127 eV for the second electron belongs to a coincident detection of the K-Auger electron of carbon with the photoelectron of K-shell oxygen.

Last but not least, the work presents three charged molecular fragments that have been detected in coincidence. Therefore, some configurations have been inspected, such as $H^+/CH_2^+/CH_2^+/CH_3O$, $H^+/CH_2^+/C_2H_2^+/H_2OH$, $H^+/O^+/C_3H_3^+/H_4$ and $CH_2^+/O^+/C_2H_4^+/H_2$. The last one was chosen as the most suitable one to produce the necessary results concerning the electron coincidence features, based on statistics efficiency. Thus, in the next figure 8.6, the electron coincidence map for this four body breakup channel is presented. The characteristics observed in the electron coincidence plots along the diagonal line are still obvious, as already explained in connection with the previous three body breakup channels. Nevertheless, the statistics in the four body breakup channels are limited, which is a common characteristic to all four body breakup channels.

In line with the measurement strategy employed already for the studies on O_2, additional measurements using a lowered B-field have been performed, as well. These measurements allow for a more detailed inspection of low energy electrons and may provide further details on the charge-up processes. Using the same breakup channels as in the case of the high magnetic field, the results are presented in the following diagrams. The photon energy remains at 670 eV. The calibrated electron measurements are presented in the next figure 8.7 for the channel with the best statistics.

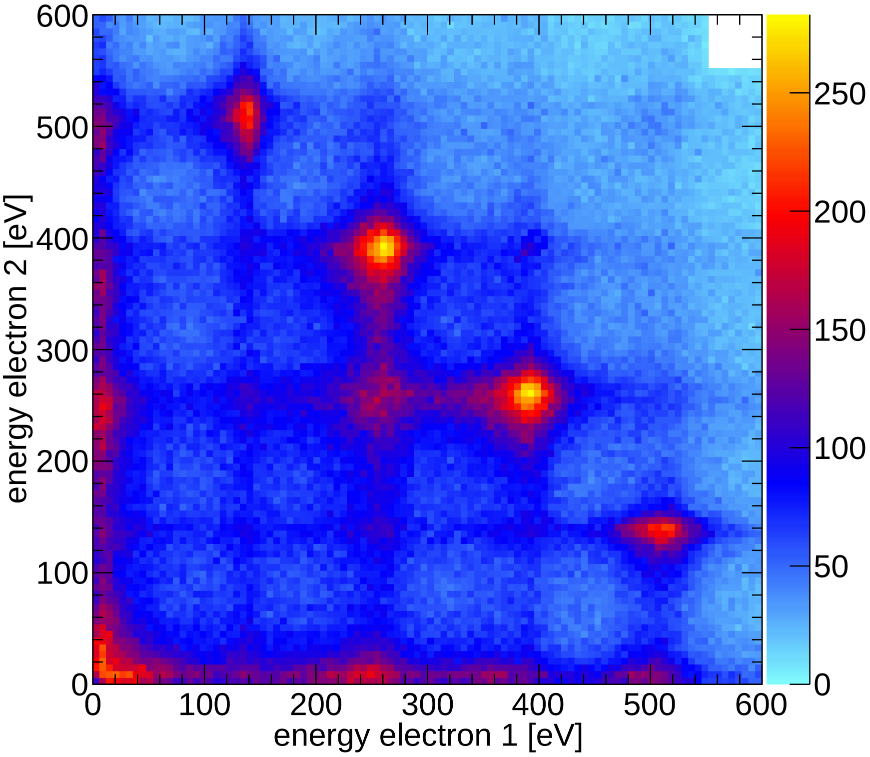

Figure 8.4: The electron coincidence map recorded employing a high magnetic field and photon energy at 670 eV and restricting the dataset to the breakup channel consisting of O^+ and of $C_3H_5^+$ (assuming three neutral hydrogen atoms which were not detected). The diagonal line shows the strong electron electron correlations. The rest of the islands shows other possible combinations of electrons which are less prominent.

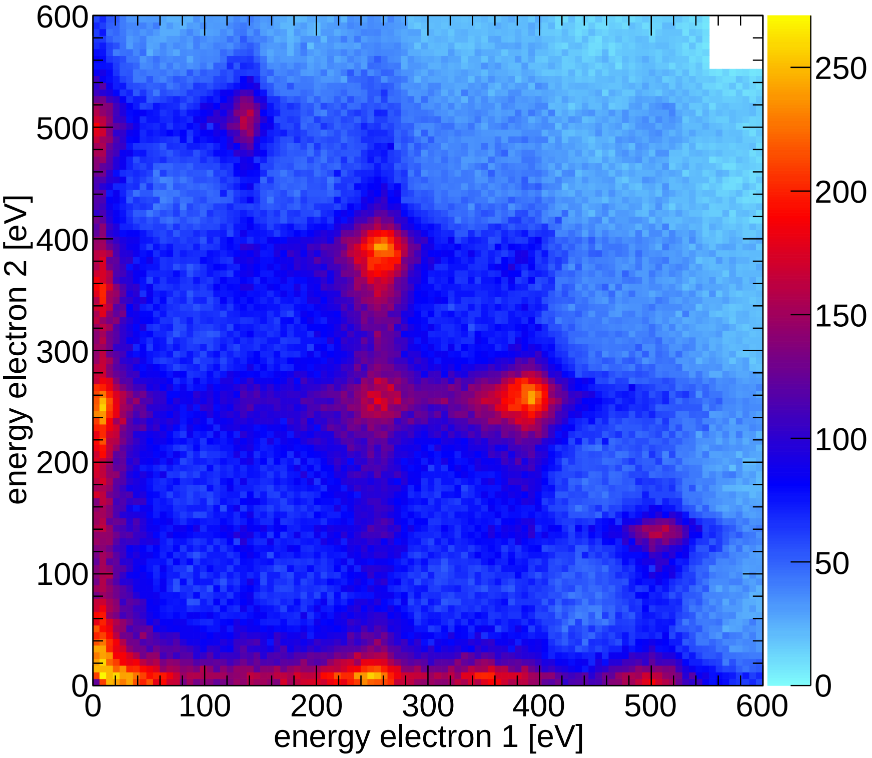

Figure 8.5: The electron coincidence map obtained using high magnetic field and photon energy of 670 eV. The inspected breakup channel consists of CH_3^+, CH_3^+, and a CH_2O fragment that has not been detected (and thus been assumed uncharged). The diagonal line shows features belonging to photoelectrons and their respective Auger electrons. The rest of the islands show other possible combinations of electrons with less intensity.

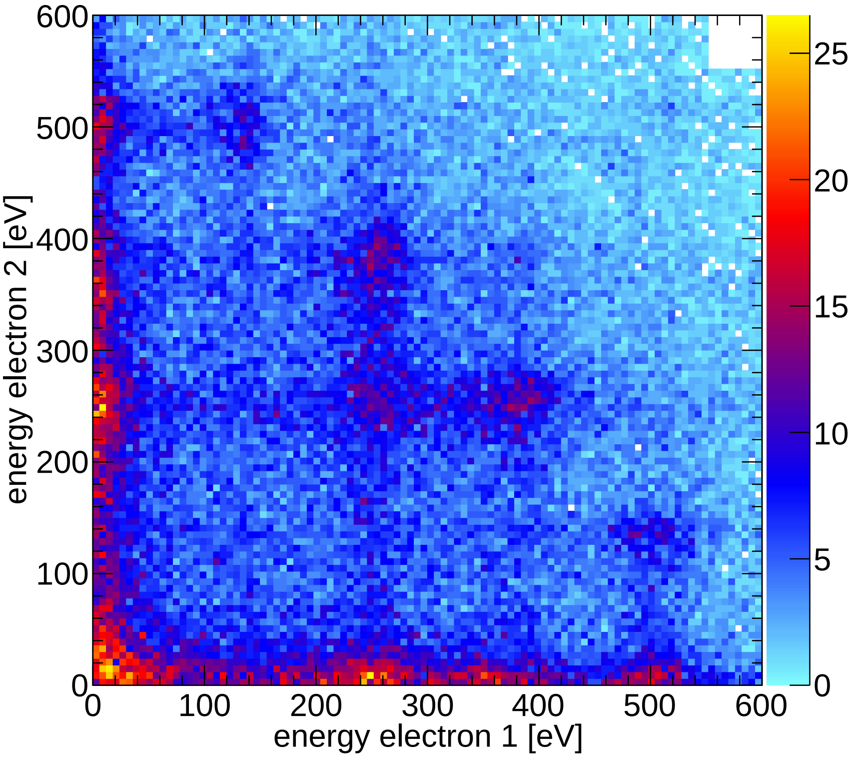

Figure 8.6: Electron coincidence map recorded at $\gamma = 670$ eV restricting the dataset to the fragmentation channel $CH_2^+/O^+/C_2H_4^+$. Two hydrogen atoms have not been detected in this fragmentation channel. Due to the three-particle coincidence the recorded statistics are comparably low.

The peaks visible in the energy spectra indicate the exact same physics which has been observed using the high magnetic field. In the next figure 8.8, the electron islands confirm the physics observed with the high magnetic field, although the statistics in this case is better for low energy electrons. In the electron coincidence maps, the electrons appearing at an energy of 127 eV, correspond to the photoelectron from the K shell of oxygen, at energy 250 eV, to K-Auger decay of carbon, at energy 385 eV, to photoelectron from the K shell of carbon, and at energy 500 eV, to the K-Auger decay of oxygen.

The figure shows much more clearly as compared to the corresponding plot using the high magnetic field a triangular feature which was observable for higher charge states in case of employing O_2 as a target for the study. This feature was identified there to belong to cases of a direct double ionization of the molecule. Accordingly, it seems that the isopropanol molecule is ionized, as well, via direct double ionization in some cases. It is a little surprising to find the traces of this process in a doubly charged break-up channel, as a subsequent Auger decay should be a common decay route after the double ionization involving the K-shell of the molecule. I can therefore be assumed that (at least some part of) the fragment that has not been detected is actually charged.

Another breakup channel was chosen in the case of the low magnetic field for a further comparison of the low magnetic field measurement with the previously presented high magnetic field measurement, as shown in the figure 8.9. The breakup channel is defined as : $CH_3^+/C_2H_3^+/H_2O$. The observed island in the electrons coincidence spectra are in agreement with not only with the previous breakup channel, but also with the physics in the case of the high energy electron measurements.

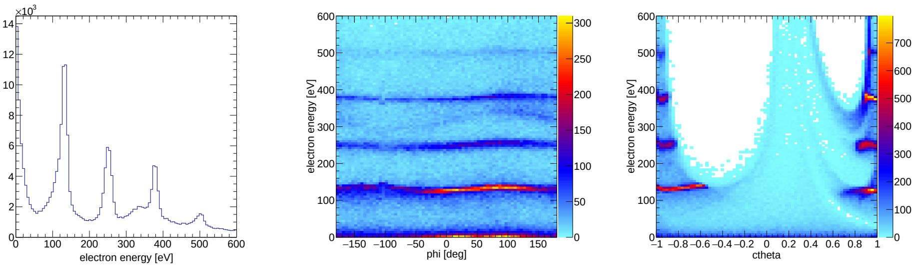

(a) (b) (c)

Figure 8.7: Calibrated electron spectra employing 670 eV photons and a 15 Gauss magnetic field. In the left panel is the electron energy spectrum, showing the photoelectron(1s) of oxygen at 127 eV, the photoelectron(1s) of carbon at 385 eV, the K-Auger decay of carbon at 250 eV and the K-Auger decay of oxygen at 500 eV. The central panel shows the electron energy as a function of angle ϕ and the right panel shows the electron energy as a function of $cos(\theta)$. The breakup channel $O^+/C_3H_5^+/H_3$.

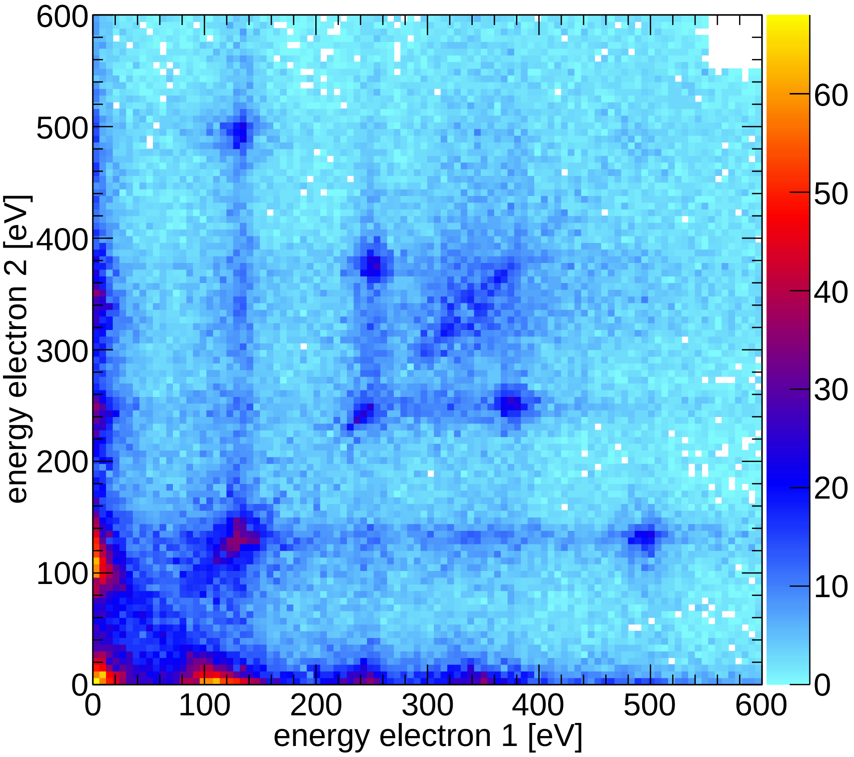

Figure 8.8: Electron coincidence map recorded with a lowered magnetic field and photon energy of 670 eV. The breakup channel is $O^{+}/C_3H_5^{+}/H_3$. The diagonal line shows the aforementioned combinations of photo- and Auger electrons. At lower energies a triangular feature indicates the occurrence of a direct double ionization involving the O-K-shell.

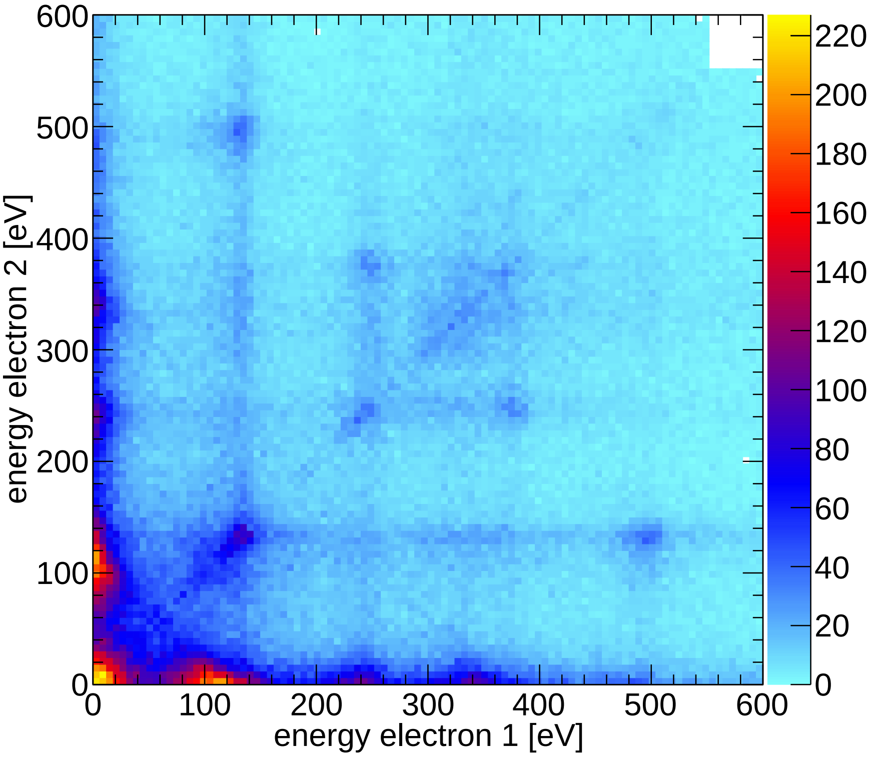

Figure 8.9: The same electron coincidence map as shown in Fig. 8.8, after selecting the fragmentation channel $CH_3^+/C_2H_3^+/H_2O$. Similar feature are observable, the direct double ionization seems to be more attributed.

Further measurements have been performed at a photon energy 600 eV, cover high- and low energy electrons using two different B-field settings. As a result, the magnetic field remained at 40 Gauss in the first case and 15 Gauss in the second case. Reducing the photon energy, however, yields a shift of the photoelectron lines, which resulted in a partial overlapping of the carbon photo- and Auger electrons when using the high B-field setting. The breakup channels for this analysis were chosen in accordance with the case of 670 eV photon energy, to maintain consistency and make easier the comparison even between the two different photon energy measurements.

In the next figure 8.10, the calibrated electron measurements are presented. The measurements were done using the high magnetic field, the results shown were recorded at $hv = 600$ eV. The high magnetic field allows to detect electrons of higher kinetic energy and thus well-suited to obtain an overview of the different types of emitted electrons (Auger and photoelectrons). It is less suited to resolve finer details. However, as the electron coincidence map in Fig. 8.11 shows, the features belonging to the $1s$ C-photoelectron and its corresponding Auger electron both are visible even when using the high B-field. In both figures, the channel with the highest statistics was chosen, which consists of O^+ and $C_3H_5^+$, accompanied by three hydrogen atoms which were not detected.

Figure 8.10 shows the spectra of electron at the left panel of the figure along with the kinetic energy of the electrons as a function of the azimuthal and the polar angle, at the centre and the right panel of the figure, respectively. According to the electron energy spectra, the photoelectron of the $1s$ state of oxygen is located (as expected) at 67 eV and the photoelectron of the $1s$ state of carbon at 315 eV. In addition to that, the Auger electron of the K shell of carbon at 250 eV and the Auger electron of the K shell of oxygen at 480 eV appear, as well.

Due to the high B-field, the separation of the electrons, especially between of the Auger electron of carbon and the photoelectron of oxygen is compromised. This is even more obvious in the electron coincidence map 8.11. The diagonal belongs to the coincident detection of the K-photoelectron of oxygen at electron energy 67 eV with the K Auger electron of oxygen at electron energy 480 eV as well as the combination of the K-photoelectron of carbon at electron energy 315 eV with the K Auger electron of carbon at electron energy 250 eV.
Further features are visible in the range of 220 eV and 350 eV for the first and the second electron, which shows apart from the combined detection of the photoelectron and the Auger electron from carbon, the coincidence between the photoelectron from carbon with itself and the Auger electron from carbon with itself, as well.

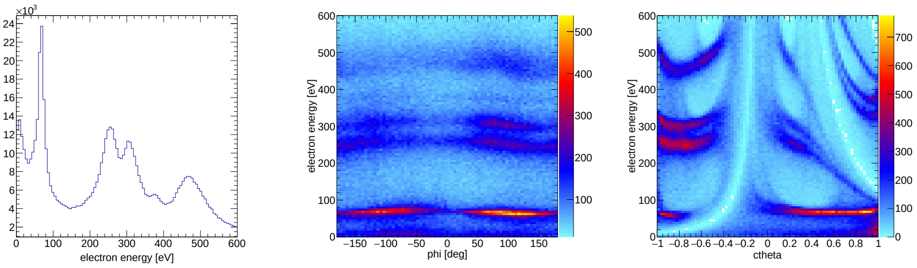

(a) (b) (c)

Figure 8.10: Calibrated Electron spectra at photon energy 600 eV and 40 Gauss B-field. Left panel: electron energy spectrum. Centre panel: electron energy as a function of the angle phi. Right panel: electron energy as a function of cosine angle theta. The breakup channel consists of two charges O^+ and $C_3H_5^+$, accompanied with 3 undetectable protons.

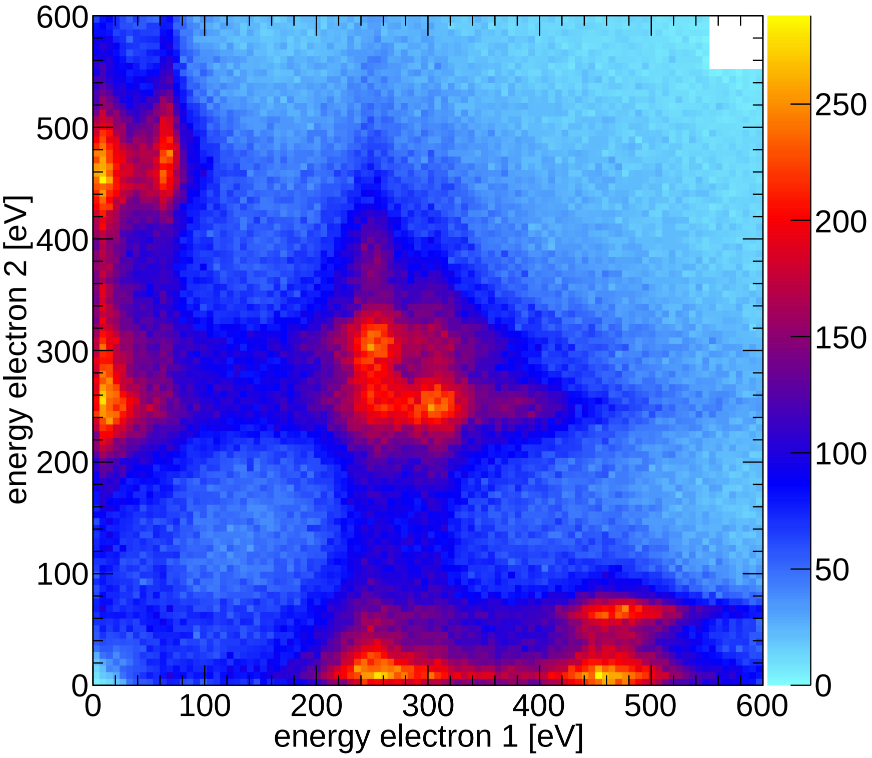

Figure 8.11: Electron coincidence map at photon energy 600 eV and high B-field in a three body breakup channel CH_3^+, CH_3^+, and an undetectable ion CH_2O.

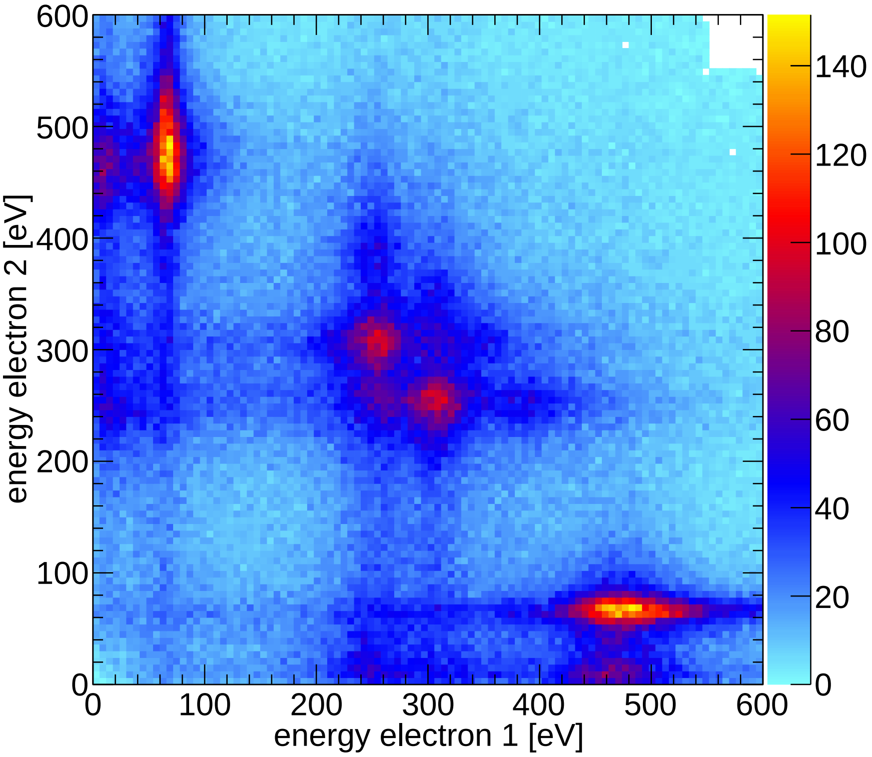

Figure 8.12: Electron coincidence map measured using high B-field and photon energy at 600 eV. The breakup channel consists of CH_3^+, $C_2H_3^+$, and H_2O.

In line with the results presented before, we expanded the analysis of the data beyond the breakup of the molecule into $O^+C_3H_5^+$. Figure 8.12 shows the breakup channel, consisting of the ion CH_3^+ and $C_2H_3^+$ with an undetectable water ion. In comparison with the electron coincidence map 8.11, the statistics is lower, especially for the part of the electron correlations between the 1s-photoelectron of carbon and the K-Auger electron of carbon. Figure 8.13 examines in addition a four-body breakup channel, consisted of the ions CH_2^+, O^+, $C_2H_4^+$ and two hydrogens H_2. The statistics decreased significantly in that case, but the features of every potential electron electron combination show up as well, especially the electron islands on the diagonal line. The electrons appear at the same kinetic energies as in the above presented electron maps 8.11.

Moreover, the analysis for the 600 eV photon energy was repeated while employing a low B-field at 15 Gauss. We inspect the same breakup channels like for the analysis using high B-field. First of all, the statistics in that

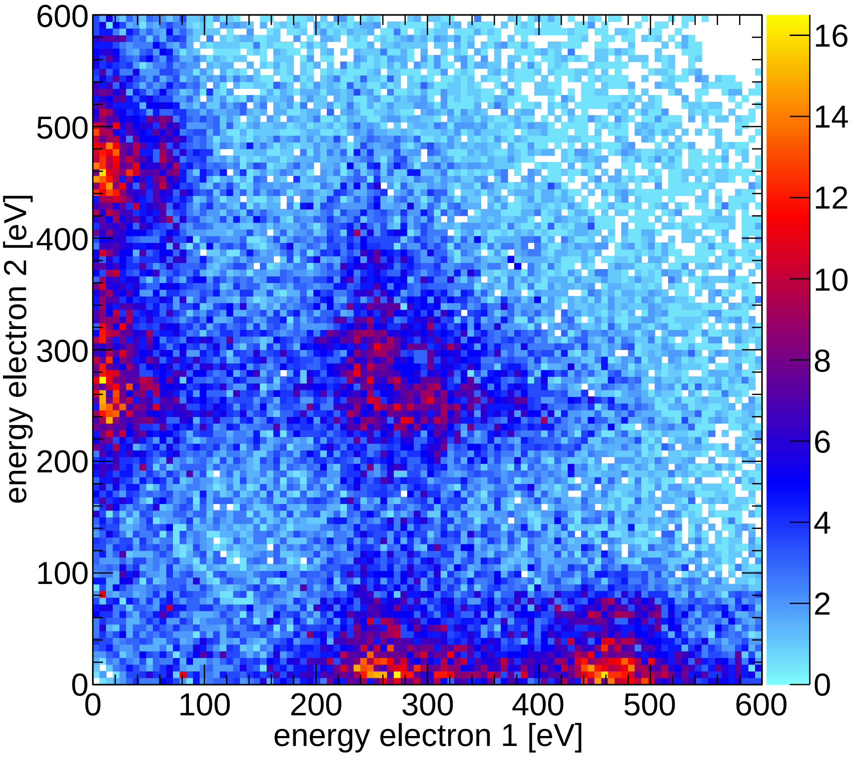

Figure 8.13: Electron coincidence map measured using high B-field and photon energy at 600 eV. The breakup channel consists of CH_2^+, O^+, $C_2H_4^+$, and 2 hydrogens.

case is lower than the statistics in the high B-field measurement. Second of all, the use of a low B-field made it harder to capture the Auger electrons. Accordingly, the features connected to these high energy electrons are strongly suppressed in the data.

Figures 8.14 and 8.15 present the electron coincidence maps, using a low B-field and 600 eV photon energy for the $O^{+}C_3H_5^{+}$ and the $CH_3^{+}C_2H_3^{+}$ breakup channels, respectively. Both of them include approximately the same statistics. With the given experimental parameters, the detection focuses much more on low energy electrons. In particular, the triangular feature, which appeared in the case of multiple ionization of the O_2 molecules presented earlier, becomes a dominant feature. It is surprising to see this feature appearing so strong despite the detected molecular fragments consist of only two charged entities. Either the assumption that the missing fragment is neutral is wrong, or the overall size of the molecule changes the probability of direct double ionization as compared to the much smaller oxygen molecule.

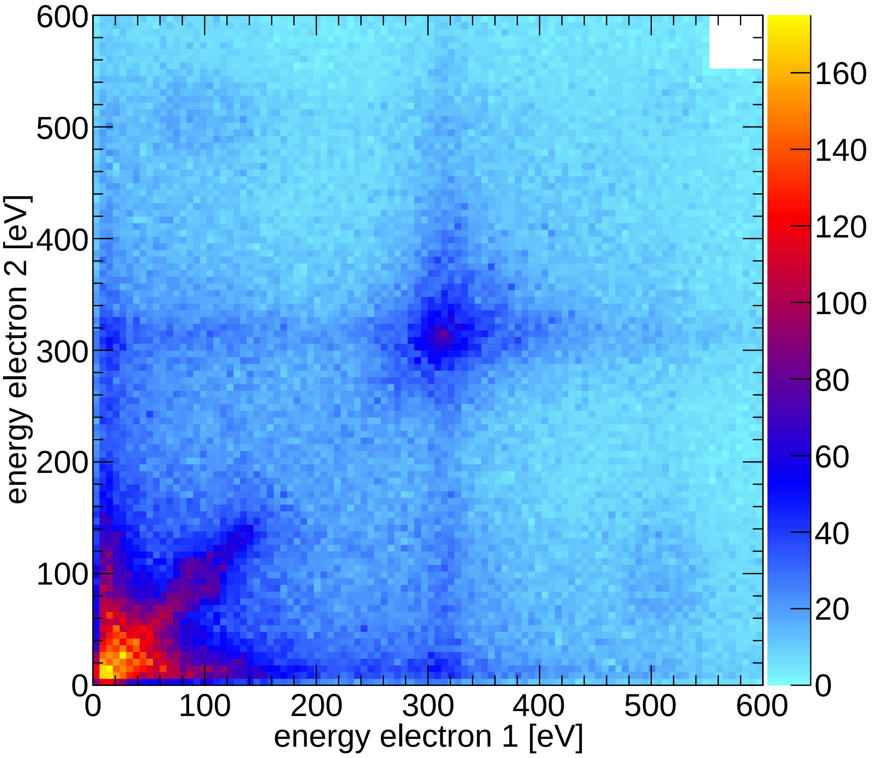

Figure 8.14: Electron coincidence map employing low B-field and photon energy at 600 eV. The three breakup channel consists of O^+, $C_3H_5^+$, and three hydrogens. The dominant feature is the low energy electrons measurements (triangular feature).

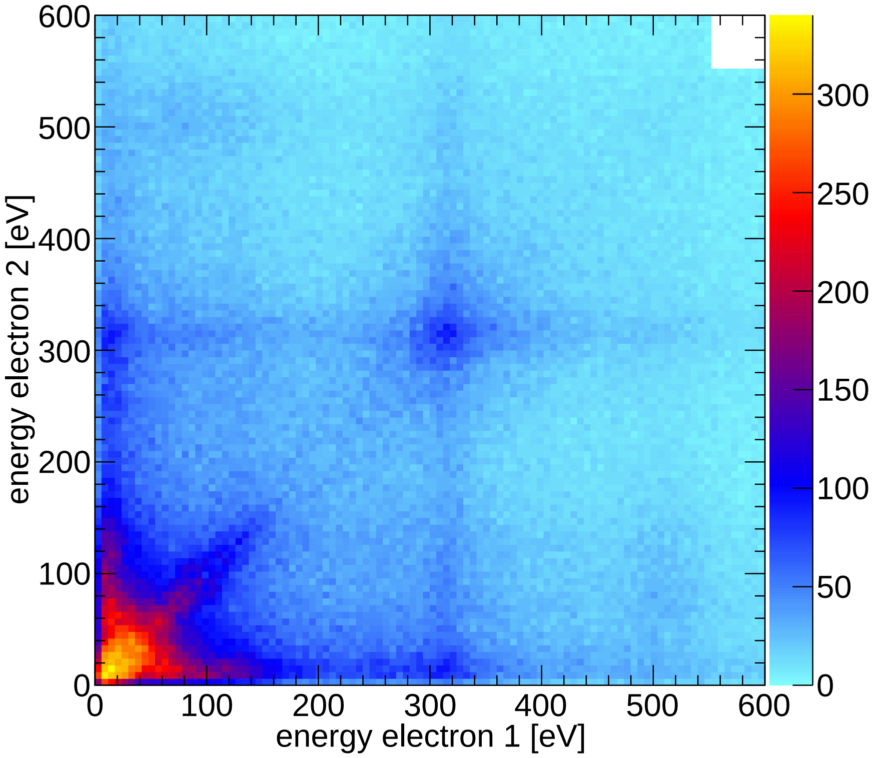

Figure 8.15: Electron coincidence map employing low B-field and photon energy at 600 eV. The three breakup channel consists of CH_3^+, $C_2H_3^+$, and H_2O. The dominant feature is the low energy electrons measurements (triangular feature).

Last but not least, we performed measurements using high B-field at photon energy of $h\nu = 563$ eV. The first noticeable effect is that the photoelectron from the $1s$ orbital of oxygen is emitted with a low kinetic energy of 20 eV. Moreover, the K-Auger electron of carbon, located at 250 eV, is overlapped by the photoelectron from $1s$ orbital of carbon, located at 278 eV, making the separation of both electrons highly unlikely, which is presented in figure 8.16. Finally, the K-Auger electron of oxygen at 505 eV is cleanly visible, because of the impact of the high magnetic field at 40 Gauss. For this analysis, the same breakup channels like before were used, and the $O^+C_3H_5^+H_3$ had the best statistic. The statistics for the four body breakup channels was low, made unavailable to offer any further important insights. Figure 8.17 presents the electron coincidence map, showing the overlap around 250 eV for the photoelectron from $1s$ orbital of carbon and the K-Auger electron of carbon. For a reason of completeness, another four body breakup channel is presented in figure 8.18. The channel consists of $CH_2^+O^+C_2H_4^+H_2$. The statistics are much lower as compared to the channel selected for Figure 8.17.

Another way to extract useful information about the structure and the dynamics of a molecule is the powerful experimental technique of Coulomb Explosion (CE). During that process, the molecule loses many electrons in a very short period of time resulting to break into parts or to explode. The positive charges on the molecule repel each other due to the strong forces from the Coulomb potential. This is exactly the process which is already employed in the case of formic acid and how to extract information about the molecular dynamics. In the case of isopropanol two different four-body breakup channels have been identified with respect to sufficient statistics and analyzed along the concepts of Coulomb explosion imaging. Figure 8.19 presents the $CH_2^+/O^+/C_2H^+$ breakup channel and figure 8.20 presents the $H^+/O^+/C_3^+$ breakup channel. In both cases different ions were chosen to define the molecular frame while the other two ions are plotted.

At the left panel of plot 8.19, the ion CH_2^+ defines the x axis and the oxygen is plotted at the top part of the plot and the C_2H^+ is plotted at the bottom part of the plot. The momentum-space data have been normalized such, that the momentum of the ion defining the x-axes equals always 1. In this so-called Newton diagram, the two latter ion fragments are located on a circle shifted to the left by about 0.5. This shifted circle is a clear proof of a two-step dissociation mechanism. In the first step, the molecule creates the first ion CH_2^+ and the combination of the other two ions together. Then after a delay, when the force of the first ion onto the combination fragment is negligible, the second step occurs: the combined $O^+C_2H^+$ ion, which is moving to the left, dissociates into an O^+ ion and a second C_2H^+ ion. The exact same picture with a different combination of the same breakup channel is presented at the right side of the same plot. In that case, the ion O^+ was chosen to define the x axis and the relative momentum vectors of

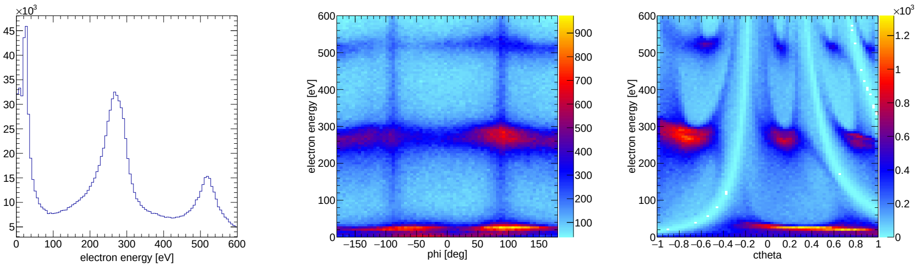

(a) (b) (c)

Figure 8.16: Calibrated Electron spectra in the case of 563 eV photon energy using 40 Gauss B-field. The left panel depicts the electron energy spectrum, showing the photoelectron from oxygen at 20 eV, the photoelectron from carbon at 278 eV and the K-Auger electron from carbon at 250 eV are overlapped, and the K-Auger electron from oxygen at 505 eV. The central panel shows the electron energy as a function of the angle ϕ. The right panel depicts the electron energy as a function of cosine angle θ. The breakup channel consists of the ions O^+, $C_3H_5^+$, and 3 hydrogens.

the C_2H^+ and CH_2^+ are mapped in the upper and lower half, respectively. As both plots look very similar, a concerted breakup of the molecule is a possible scenario, as well. In such a case, however, the momenta of the two plotted ions are typically more confined. Accordingly, the fragmentation dynamics are probably a mixture of the sequential and concerted case.

In a very analogous way, another breakup channel was chosen, consisting of the following ions H^+, O^+ and C_3^+, as shown in figure 8.20. The same situation is happening here with different participating ions within the breakup channel. At the left panel of the figure, the proton defines the x axis and the oxygen with the C_3 ion are mapped at the upper and the lower half, respectively. At the right part, the oxygen defines the x axis and the C_3 ion along with the proton are plotted at the upper and the lower half, respectively. In this particular case, the only problem which is arising, is the inability to infer which proton participates within this specific breakup channel from the isopropanol molecule. However, in the first case the combination of O^+ and C_3^+ ions is emitted back-to-back, resulting in two circles in the upper and lower half of the newton plot. The same situation becomes more obvious at the right part of the same plot since the proton is the particle that was ejected from the molecule and is represented as a circle in the lower half of the newton plot. The remaining C_3^+ is plotted in the upper half of the newton plot.

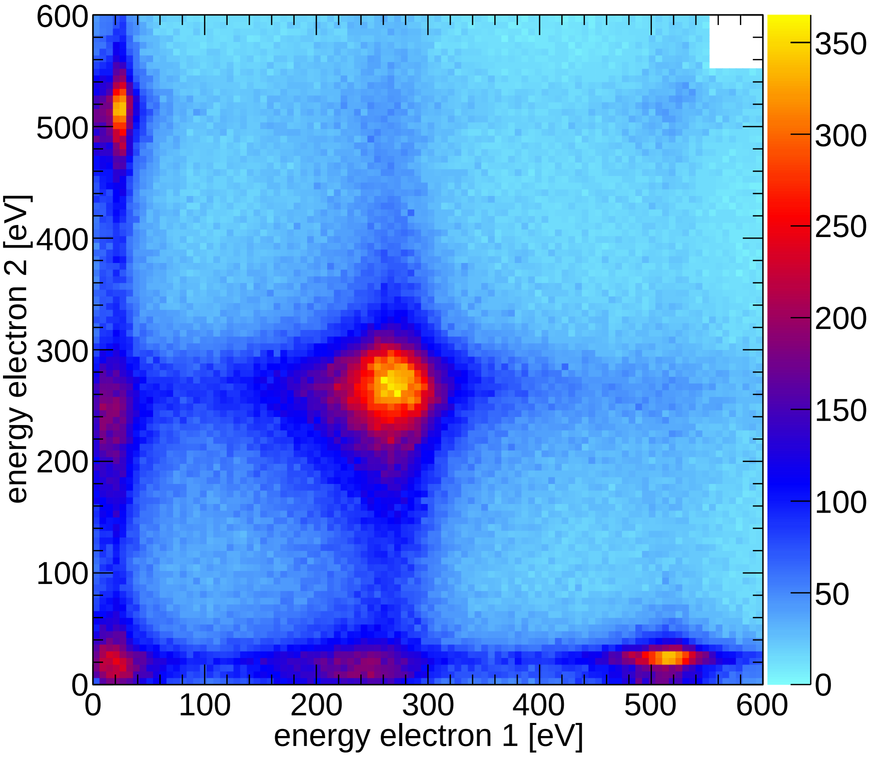

Figure 8.17: Electron coincidence map measured using a high B-field and photon energy at 563 eV. Three body breakup channel O^+, $C_3H_5^+$, and 3 hydrogens.

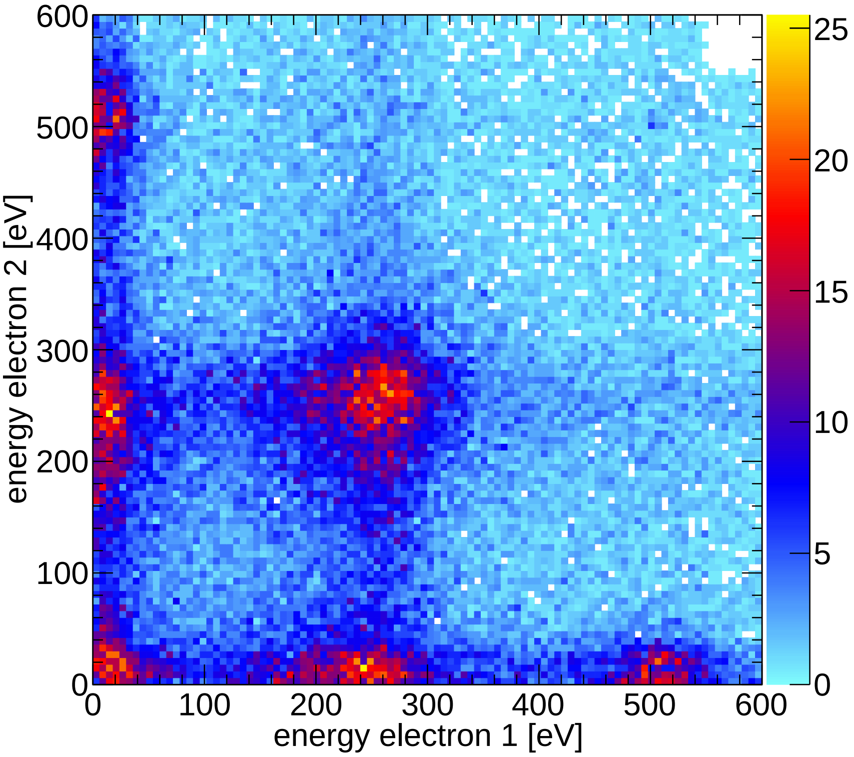

Figure 8.18: Electron coincidence map measured using a high B-field and photon energy at 563 eV. Four body breakup channel CH_2^+, O^+, $C_2H_4^+$, and 2 hydrogens.

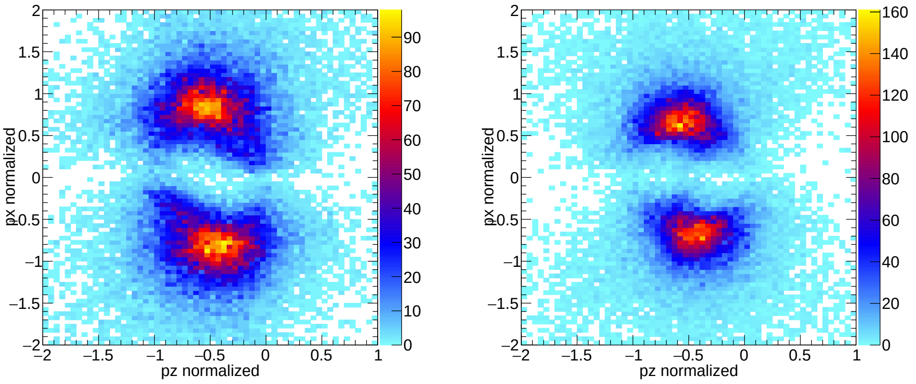

(a)

(b)

Figure 8.19: Newton diagram of the breakup channel defined as: $CH_2^+/O^+/C_2H^+$. Left side: Momentum vector of CH_2^+ defines the x axis, while the remaining momentum vectors of the O^+ and C_2H^+ are mapped in the upper and lower half, respectively. Right side: Momentum vector of O^+ defines the x axis, while the remaining momentum vectors of the C_2H^+ and the CH_2^+ are mapped in the upper and lower half, respectively.

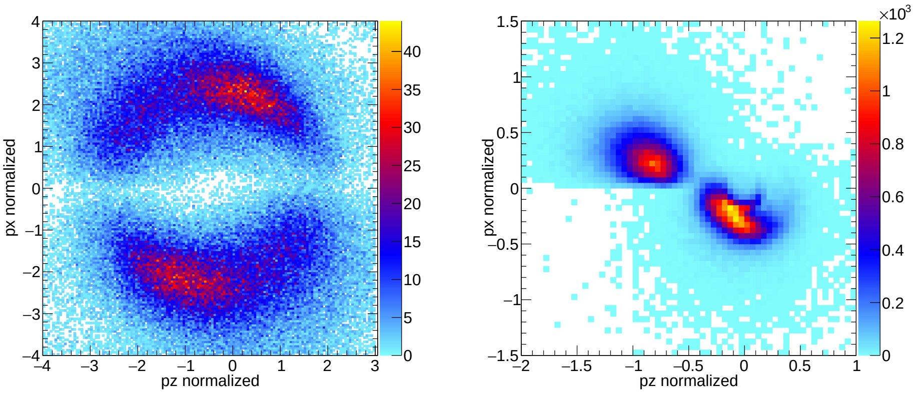

(a)

(b)

Figure 8.20: Newton diagram of the breakup channel defined as: $H^+/O^+/C_3^+$. Left side: Momentum vector of H^+ defines the x axis, while the remaining momentum vectors of the O^+ and C_3^+ are mapped in the upper and lower half, respectively. Right side: Momentum vector of O^+ defines the x axis, while the remaining momentum vectors of the C_3^+ and the H^+ are mapped in the upper and lower half, respectively.

8.2 CALIBRATION OF ISOPROPANOL

The analysis of the isopropanol was performed after the calibration with the use of N_2 molecule and Ar. In addition to that, the electric field and the detector calibration obtained from the N_2 molecule dataset. The process was a photoionisation with a photon energy 420.0 eV, as shown in equation 8.1. The calibration for the electrons are performed by using Argon atoms and different photon energies for the ionization in accordance with 8.2.

$$\gamma + N_2 \rightarrow N_2^{*+} \rightarrow N^+ + N^+ + e_\gamma^- \tag{8.1}$$

$$\gamma + Ar \rightarrow Ar^+ + e_\gamma^- \tag{8.2}$$

The binding energy of the $1s$ orbital of carbon is 410.0 eV, leads to a photoelectron of 10 eV. The calibrated spectra for the ions are shown in Figure 8.21. The corresponding spectra for the electrons, produced by the ionisation of the Argon, are shown in Figure 8.22, using 42 Gauss B-field and in Figure 8.23, employing 13 Gauss B-field. The time offset t_0 as well as the magnitude of the magnetic field were extracted by scanning over several gyration nodes, with the corresponding spectra shown in figure 8.24. The distance between two nodes provides the experimental value of the magnetic field.

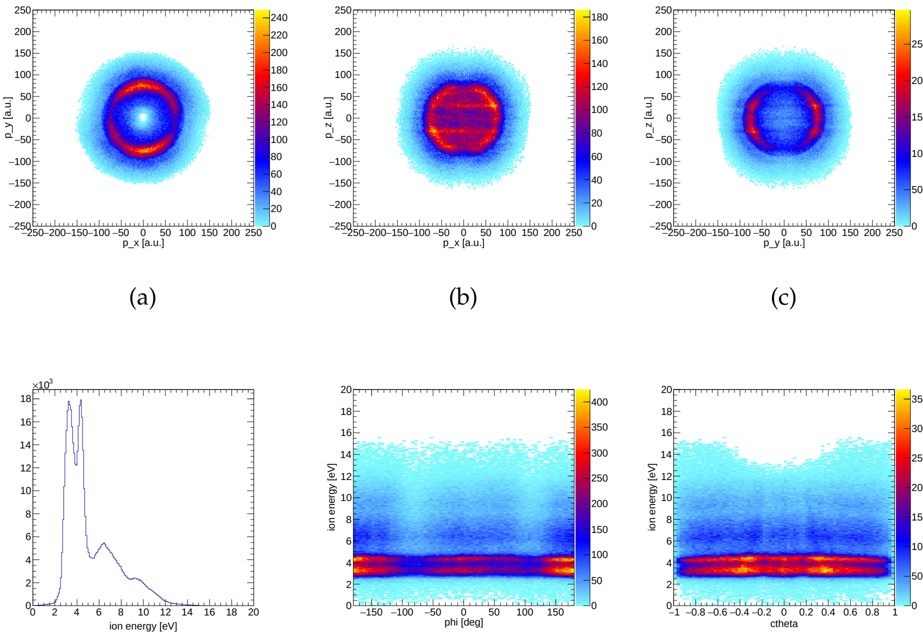

(a) (b) (c)

(d) (e) (f)

Figure 8.21: Ion spectra employed for the calibration of the ion arm of the spectrometer. Top row: momenta of the measured N^+ ions. Bottom row: ion kinetic energy (d) and its dependence on the ion emission angles (e,f).

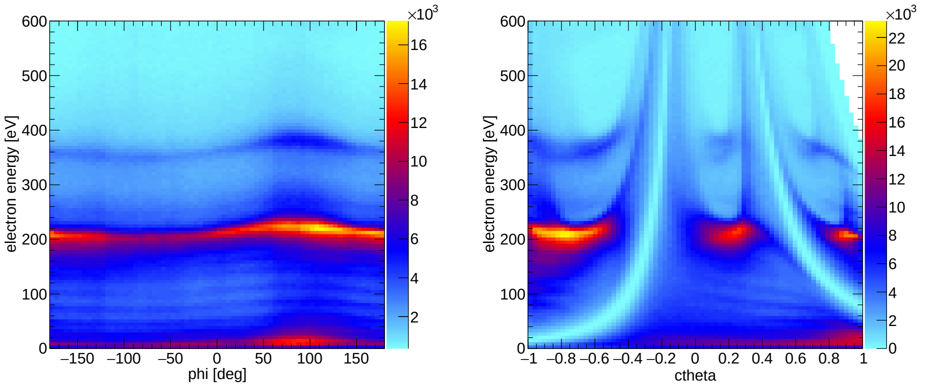

(a) (b)

Figure 8.22: Results of the calibration measurements conducted during Session 2 (studying photoionization of isopropanol): Photoionisation of Ar($2p$) electrons at photon energies of 260.0 eV, 280.0 eV, 300.0 eV, 325.0 eV, 350.0 eV, 380.0 eV, 400.0 eV, 450.0 eV, 500.0 eV and 600.0 eV. Electron kinetic energies as a function to angle ϕ (left)and as a function of the cosine of angle θ concerning the electric field of the spectrometer (right).

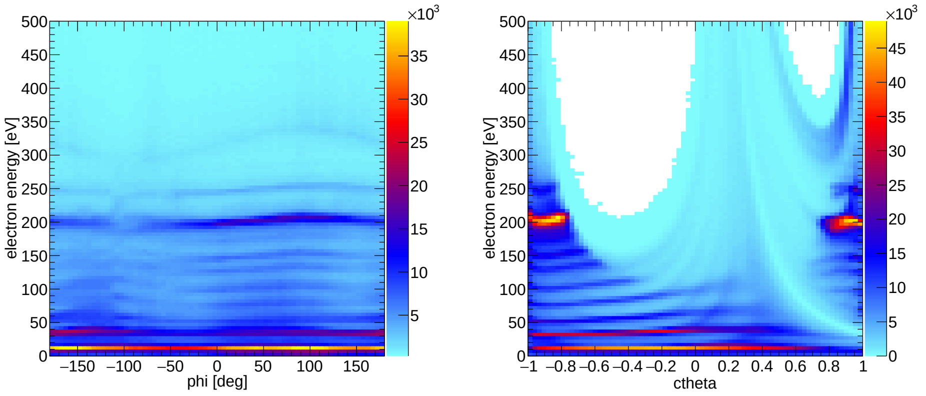

(a)

(b)

Figure 8.23: Results of the calibration measurements conducted during Session 2 (studying photoionization of isopropanol): Photoionisation of Ar($2p$) electrons at photon energies of 260.0 eV, 280.0 eV, 300.0 eV, 325.0 eV, 350.0 eV, 380.0 eV, 400.0 eV, 450.0 eV and 500.0 eV. Electron kinetic energies as a function to angle ϕ (left)and as a function of the cosine of angle θ concerning the electric field of the spectrometer (right).

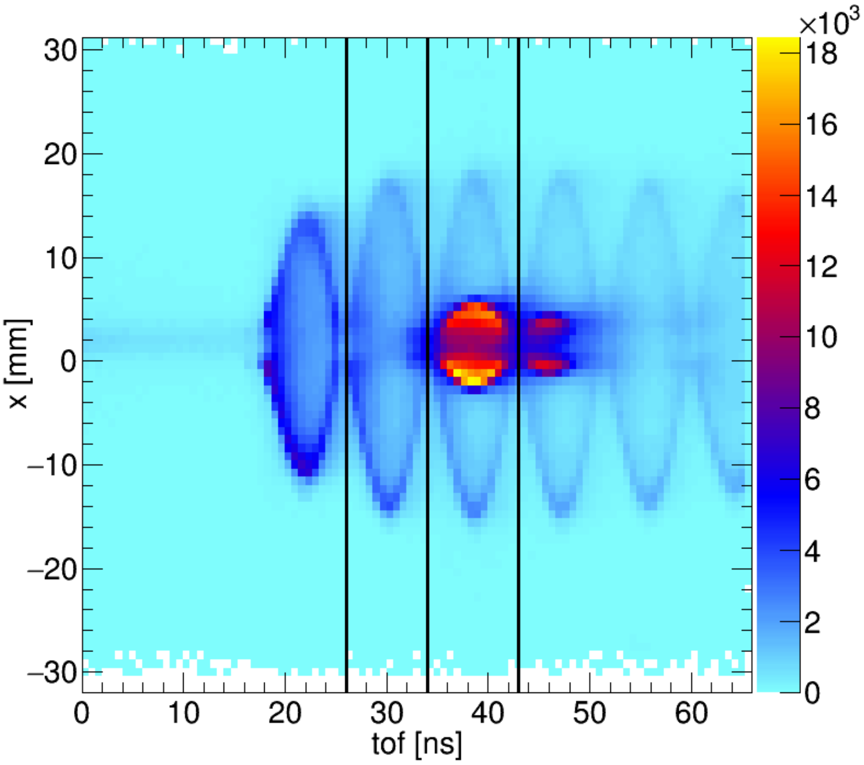

Figure 8.24: Time-of-flight versus detection (x-direction) position of electrons for t_0 measurement and magnetic field calibration. The black straight lines define different node positions in nanoseconds.

8.3 EXPERIMENTAL PARAMETERS OF ISOPROPANOL MOLECULE

In this part, the basic parameters of the experimental setup are presented for convenience, based on the information in chapter 4, describing all the necessary parameters in the different experiments. The measurements were performed at the permanent COLTRIMS Endstation of beamline *PO*4 of the PETRA *III* Synchrotron at DESY, Hamburg in August 2020. The synchrotron ring was operated in 40 bunch timing mode, which corresponds to a time spacing of 192 ns between photon bunches. The full information are presented in the following tables 8.2.

Spectrometer		
Electron arm	17cm	
Ion arm	4.5cm(acceleration) + 7.5cm(drift)	
E-field	50 V/cm	
B-field	42 G and 13 G	
Voltages		
Electron Detector	+160V(front)	+2701V(anode)
Ion Detector	-2712V(front)	-303V(anode)
Spectrometer	+112V(electron side)	-1400V(ion side)
Detectors		
Electron	80mm	
Electron MCP	regular	
Ion	80mm	
Ion MCP	regular	
Rates		
Electron	35 kHz	
Ion	6.5 kHz	

Table 8.2: Experimental Setup August 2020 for the polyatomic molecule C_3H_8O.

Part V

SUMMARY

9

SUMMARY AND OUTLOOK

To summarise, this work demonstrates the possibility for a molecule with a planar structure to elude potential chiral structures with a formation of two enantiomers under the interaction with light. We choose formic acid, as a small molecule with a comparably simple structure and explored two different technical approaches. Firstly, an excitation of an inner-shell electron to an excited state, such as π^* state was implemented. As a second approach we used photoionization accompanied by fragmentation of the molecule. We investigated the molecular frame photoelectron angular distributions. We found that those also showed a chirality of the molecule by performing a measurement at photon energy 305.5 eV.

In addition to the investigation centred on the achiral molecule formic acid, this study extended its scope by conducting two supplementary experiments. Drawing inspiration from the molecular dynamics of formic acid, the electron interactions in diatomic (oxygen) and polyatomic (isopropanol) molecules were explored.

All the experiments were performed using the permanent cold-target recoil-ion momentum spectroscopy (COLTRIMS) end station, installed at beamline *P*04 at PETRA III at DESY in Hamburg, Germany.

The first chapter (1) introduces molecular chirality and next chapter (2) mentions some technical approaches allowing for chiral discrimination.

The third chapter 3 describes the experimental setup. After a brief description of the light source, the main building blocks of the Coltrims Reaction microscope, namely the gas jet system, the spectrometer the detectors and the data acquisition are described. In chapter 4. the experimental parameters of the various experiments performed for this work are listed. Chapter 5 describes the data analysis and the calibration procedures.

The results of this research are in three distinct chapters. The first chapter 6 is the main work of this thesis, and discusses the examination of the formic acid molecule. The next chapter 7 presents the results of obtaining information for the molecular dynamics through electron interactions in the case of a diatomic molecule, like oxygen. The last chapter 8 extends the effort from a diatomic molecule to a polyatomic molecule, like isopropanol.

Chapter 6 presents the results of chiral signals for the formic acid molecule, which has a planar prochiral equilibrium structure. The experiments were performed in November 2020 and June 2021 at beamline $P04$ PETRA III of DESY, Hamburg. Possible excited states of an inner-shell electron from carbon or oxygen within the molecule were measured. We find for both excitation channels a non zero triple product of the momentum vectors of the carbon, the oxygen and the proton from the hydroxyl group. The measurements include a direct calculation of the handedness angle and the calculation of handedness regarding the different molecular orientations for both left- and right-handed circular polarised light.

$$\cos\alpha = ((\vec{k}_{O2+} \times \vec{k}_{C+}) \cdot \vec{k}_{H2+})/((|\vec{k}_{O2+} \times \vec{k}_{C+}|) \cdot |\vec{k}_{H2+}|) \tag{9.1}$$

To understand the physical mechanism of this enantioselection in the case of formic acid, a theoretical representation of the wave functions for the ground state and the potential excited state of $\pi^\star$ were presented. The $\pi^\star$ excited state is associated with a double-well potential, which indicates the left- and right-handed equilibrium positions. The transition matrix element $M(R, \vartheta, \phi)$ depends on the direction of the light polarisation in the molecular frame, i.e., on the angles θ, ϕ from which the light impinges onto the molecule. The physics behind the symmetry breaking employs for a given direction θ and ϕ, and this matrix element must be different for positive and negative R, resulting in populating left- or right-handed pyramidalised configurations.

Calculations performed by the collaborating theory group of Philipp Demekhin (Kassel) of the transition matrix element as a function of θ and ϕ for both cases of the enantiomers and the normalised differences between the two matrix elements, this reveals a strong correlation with experimental observations. The largest surplus of R enantiomer occurs at $\theta = 30$, $\phi = -30$ and equal population of both enantiomers at $\theta = 90$ and along lines $\phi = -110$ and $\phi = 70$. That leads to the fact that chiral selectivity in molecules like formic acid is primarily governed by the dipole matrix element between the transiently chiral ground state and the chiral excited state. This element's dependence on the polarisation direction within the molecular frame is key to understanding and predicting the chiral behaviour of molecules upon excitation.

In the same chapter, another experiment performed by searching for potential enantiomers in the case of photoionisation. During this experiment, a photon energy was set to produce a low energy photoelectron. Two different parameters for the photon energy were used, where the first one prioritises electron energy resolution by extracting a photoelectron with a kinetic energy 10 eV. The photoelectron offers the possibility of the method of Molecular Frame Photoelectron Angular Distribution (MFPAD), which takes a snapshot of the molecular structure at the instance of photoabsorption. This ionization step is followed after a few femtoseconds by an Auger cascade which then leads to the Coulomb explosion. Measuring the ionic momentum vectors from the coulomb explosion allows us to take a second, time-delayed snapshot of the molecular geometry. We find that both these probings of the structure yield the same handedness. Thus any real sample of formic acid consists of individual molecules which are chiral, despite the planar equilibrium structure of formic acid. Consecutive sensing of the this structure on the same individual molecules confirms that the handedness is a property of the individual particle and prevails at least on the timescale of femtoseconds.

Chapter 7 constitutes a comprehensive exploration of electron interactions within the diatomic oxygen molecule (O_2). The primary objective of this endeavour was the measurement of both low-energy and high-energy electrons. To achieve this, the same spectrometer settings were applied with two different magnetic field parameters, tailored on the detection of the respective electron energy. These experiments were performed at PETRA III synchrotron facility at DESY, Hamburg.

A noteworthy aspect of this work is also the comparison with data recorded from the X-ray Free Electron Laser facility (XFEL) in Hamburg. This comparative study employed identical breakup channels for both datasets, facilitating a comparison between the two different light sources. In case of Free Electron Laser (FEL), the intensity is so high that multi-photon absorption process occur. As the total charge increases, it becomes evident that these higher charge states are indeed a result of the absorption of multiple photons, as in the case of XFEL. This implies also the efficient method of XFEL in generation of higher charge states, which is further characterised by the appearance of distinct, well-defined peaks in the electron spectrum [79].

Chapter 8 presents the results of electron interactions in the case of isopropanol and substantially expands the previous idea of a diatomic molecule to a polyatomic molecule. The experiments also performed at the synchrotron facility of PETRA III, at DESY, Hamburg. The datasets were split in three different photon energies and two different magnetic fields by measuring low- or high-energy electrons. The photon energies were 670 eV, 600 eV, and 563 eV and the magnetic field were 42 Gauss and 14 Gauss. During the process, several breakup channels of the molecules are overlapped, leading to an increase of the uncertainty with regard to the participated ions within the breakup channels. The most important factor of the analysis was to identify the correct ions within a channel by applying strict momentum gates to the total sum momenta in our first guesses and looking at the individual ions as a second step. An extra gate was applied to the kinetic energy release of the molecule, which did not make any significant difference in the final results. Moreover, it seems that the three body breakup channels have a better resolution in the electron coincidence maps in comparison with the four body breakup channels.

In summary, this thesis introduces diverse formalisms applicable to synchrotron radiation, exhibiting their utility in extracting valuable insights into the molecular dynamics of various molecules, with a particular emphasis on the intricate nature of polyatomic molecules. One formalism explores the excitation of an inner shell electron, offering the potentiality to explore the chiral structure of a molecule. Another avenue is through the photoionisation processes, which leads to Coulomb explosion imaging. This can be achieved by either measuring or not measuring the photoelectron in the molecular frame.

In the latter case, the direct visualisation of positively charged ions, particularly when at least three charges are present, provides a unique perspective on potential dissociative channels within the molecule. Through the Coulomb explosion imaging technique, this approach facilitates a direct and insightful examination of the molecular dynamics under the influence of synchrotron radiation.

Part VI

APPENDIX

A

ATOMIC UNITS

Atomic units are supposed important constants of atomic physics to one another in such a way results a consistent and practicable system of units. In contrast to the representation in SI units, the corresponding numerical values are of the order of 1. The following table presents the definitions for 1 a.u. of the variables relevant to this dissertation and the respective conversion into SI units rounded to three decimal places:

Magnitude	Constant	Symbol	SI
Charge	charge of electrons	e	$1,602 \cdot 10^{-19}\,\mathrm{C}$
Mass	Rest mass of electrons	m_e	$9,109 \cdot 10^{-31}\,\mathrm{kg}$
Impact	Planck constant	$\hbar$	$1,055 \cdot 10^{-34}\,\mathrm{Js}$
Length	Bohr Radius	a_0	$5,292 \cdot 10^{-11}\,\mathrm{m}$
Energy	Hartree-Energy	$E_h = \frac{\hbar^2}{m_e a_0}$	$4,360 \cdot 10^{-18}\,\mathrm{J}$
Time	-	$\hbar/E_h$	$2,419 \cdot 10^{-17}\,\mathrm{s}$
Momentum	-	$\hbar/a_0$	$1,993 \cdot 10^{-24}\,\mathrm{kg\ m/s}$

Table A.1: Overview of the most important atomic physical quantities and constants in atomic units and the conversion factors in the SI system. Values rounded to three decimal places taken from [80].

BIBLIOGRAPHY

[1] Subrata Sen Gupta. *Basic Stereochemistry*. Vol. 2. Oxford University Press, 2018 (cit. on p. 1).

[2] Dennis A. Dougherty Eric V. Anslyn. *Modern Physical Organic Chemistry*. Vol. 6. University Science, 2005 (cit. on p. 1).

[3] Janice M. Hicks. „The Physical Chemistry of Chirality." In: *American Chemical Society* Ch. 1 (2002) (cit. on p. 1).

[4] Irving W. Wainer. „Three-dimensional view of pharmacology." In: *American Journal of Hospital Pharmacy* 49.9 (1992), S4–S8 (cit. on p. 1).

[5] Rajender Kumar Ravi Bhushan. „Enantioresolution of DL-Penicillamine." In: *Biomedical Chromatography* 24.1 (2009), pp. 66–82 (cit. on p. 1).

[6] Giammarco Nalin. „Molecular-frame differential photoelectron circular dichroism of O 1s-photoelectrons of trifluoromethyloxirane." In: *Physical Review Research* 5.013021 (2023) (cit. on p. 2).

[7] Giammarco Nalin. „Photoelectron circular dichroism of O 1s-photoelectrons of uniaxially oriented trifluoromethyloxirane: energy dependence and sensitivity to molecular configuration." In: *Royal Society of Chemistry* (2021) (cit. on pp. 2, 9).

[8] Volker Schmidt. *Electron Spectrometry of Atoms using Synchrotron Radiation*. Ed. by A. Dalgarno et al. Vol. 1, 5. Cambridge University Press, 1997.

[9] LibreTexts. *Chiral Molecules*. LibreTexts Chemistry (cit. on p. 7).

[10] et al. Ralph H. Pettrucci. *General Chemistry: Principles and Modern Applications*. 9th ed. Pearson College Div, 2006. URL: `https://www.khanacademy.org/science/organic-chemistry/stereochemistry-topic/optical-activity/v/optical-activity-new?modal=1` (cit. on p. 7).

[11] Elsevier Scientific Publishing Company. *Origins of Optical Activity in Nature*. Ed. by Walker D. C. Vol. 31. 3. BioScience, 1981 (cit. on pp. 7, 8).

[12] Burke Ritchie. „Theory of the angular distribution of photoelectron ejected from optically active molecules and molecular nagative ions." In: *Physical Review A* 13.1411 (1976) (cit. on p. 7).

[13] L. D. Barron. *Light Scattering and Optical Activity*. 2nd. Cambridge University Press, 2004 (cit. on p. 7).

[14] Ingo Dierking. „Chiral Liquid Crystals: Structures, Phases, Effects." In: *Symmetry* 6.2 (2014), pp. 444–472 (cit. on p. 7).

[15] P. Atkins; J. de Paula. *Elements of Physical Chemistry*. 4th. 978-0-7167-7329-0. Oxford University Press, 2005 (cit. on p. 8).

[16] Edward I. Solomon. *Inorganic electronic structure and spectroscopy*. 29 April 2011. 978-0-471-97124-5. Wiley-Interscience, 3 February 2006 (cit. on p. 8).

[17] David Park. *Introduction to Quantum Theory*. 2nd. Vol. 32. 2.2 (cit. on p. 8).

[18] Kōji Nakanishi; Nina Berova; Robert Woody. *Circular dichroism: principles and applications*. VCH-Wiley, 1994 (cit. on p. 8).

[19] R. W. Woody. *Circular-Dichroim*. Vol. 246. 34-71. Science Direct, 1995 (cit. on p. 8).

[20] Alison Rodger; Bengt Nordén. *Circular dichroism and linear dichroism*. Oxford University Press, 1997 (cit. on p. 9).

[21] Helmut Wiedemann. *Particle Accelerator Physics*. Ed. by Springer Berlin Heidelberg. Third. Vol. 6. 20. Springer, 2007 (cit. on p. 9).

[22] M.E.Couprie. „New generation of light sources: Present and future." In: *Journal of Electron Spectroscopy and Related Phenomena* 196 (Oct. 2014) (cit. on p. 9).

[23] Burke Ritchie. „Theory of the angular distribution of photoelectron ejected from optically active molecules and molecular nagative ions." In: *Physical Review A* 13.4 (April 1976) (cit. on p. 9).

[24] N.A. Cherepkov. „Circular dichroism of molecules in teh continuous absorption region." In: *Chemical Review Letters* 87.4 (April 1982) (cit. on p. 9).

[25] Burke Ritchie. „Theory of the angular distribution of photoelectron ejected from optically active molecules and molecular nagative ions." In: *Physical Review A* 14.1 (July 1976) (cit. on p. 9).

[26] S. Beaulieu et. al. „Universality of photoelectron circular dichroism in the photoionization of chiral molecules." In: *New J. Physics* 18 (2016) (cit. on p. 9).

[27] Böwering N. et al. „Asymmetry in Photoelectron Emission from Chiral Molecules Induced by Circularly Polarized Light." In: *Phys. Rev. Lett.* 86.7 (2001) (cit. on p. 9).

[28] Lux C. et al. „Circular dichroism in the photoelectron angular distributions of camphor and fenchone from multiphoton ionization with femtosecond laser pulses." In: *Angew, Chem* 51.20 (2012), pp. 5001–5005. DOI: `https://doi.org/10.1002/anie.201109035` (cit. on p. 9).

[29] S. Beaulieu et. al. „Multiphoton photoelectron circular dichroism of limonene with independent polarization state control of the bound-bound and bound-continuum transitions." In: *J. Chem. Phys* 149 (2018) (cit. on p. 9).

[30] Lux C. et al. „Photoelectron circular dichroism observed in the above-threshold ionization signal from chiral molecules with femtosecond laser pulses." In: *Journal of Physics B: Atomic, Molecular and Optical Physics* 49.2 (2015) (cit. on p. 9).

[31] Gustavo A. Garcia. „Circular dichroism in the photoe electron angular distribution from randomly oriented enantiomers of camphor." In: *J. Chem. Phys* 119 (2003) (cit. on p. 9).

[32] Laurent Nahon and Gustavo A. Garcia. „Determination of chiral asymmetries in the valence photoionization of camphor enatniomers by photoelectron imaginh using tunable circularly polarized light." In: *J. Chem. Phys* 125 (2006) (cit. on p. 9).

[33] Gustavo A. Garcia. „Chiral signatures in angle-resolved valence photoelectron sperctroscopy of pure glycidol enantiomers." In: *Physical Chemistry Chemical Physics* 10 (2008) (cit. on p. 9).

[34] Gustavo A. Garcia. „Photoelectron Circular Dichroism Spectroscopy in an Orbitally Congested System: The Terpene Endoborneol." In: *J. Chem. Phys* 114.2 (2009) (cit. on p. 9).

[35] Kilian Fehre et al. „Link between Photoelectron Circular Dichroism and Fragmentation Channel in Strong Field Ionization." In: *J. Phys. Chem. A* 123.30 (2019), pp. 6491–6495 (cit. on p. 9).

[36] Gustavo A. Garcia. „Photoelectron circular dichroism and spectorscopy of trifluoromethyl- and methyl-oxirane: a comparative study." In: *Physical Chemistry Chemical Physics* 16 (2014) (cit. on p. 9).

[37] Ivan Powis. „A Valence Photoelectron Imaging Investigation of Chiral Asymmetry in the photoionization of Fenchone and Camphor." In: *Chem Phys Chem* 9 (2008) (cit. on p. 9).

[38] Gustavo A. Garcia. „Vibrationally induced inversion of photoelectron forward-backward asymmetry in chiral molecule photoionization by circularly polarized light." In: *Nature Communications* 4 (2013) (cit. on p. 9).

[39] Laurent Nahon. „Determinatio of accurate electron chiral asymmetrues in fenchone and camphor in the VUV range: sensitivity to isomerism and enantiomeric purity." In: *PCCP - Physical Chemistry Chemical Physics* 18 (2016) (cit. on p. 9).

[40] Stefano Turchini. „Conformational Sensitivity in Photoelectron Circular Dichroism of 3-Methylcyclopentanone." In: *Chem Phys Chem* 14 (2013) (cit. on p. 9).

[41] Maurice Tia. „Chiral Asymmetry in the Photoionization of Gas-Phase Amino-Acid Alanine at Lyman-a Radiation Wavelength." In: *J. Phys. Chem. Letter* 16 (2013) (cit. on p. 9).

[42] Steven Daly. „Photoionization of epichlorohydrin enantiomers and clusters studied with circularly polarised vacuum ultraviolet radiation." In: *The Journal of Chemical Physics* 134 (2011) (cit. on p. 9).

[43] Samuel Beaulieu. „Probing ultrafast dynamics of chiral molecules using time-resolved photoelectron circular dichroism." In: *Faraday Discussions* 194 (2016) (cit. on p. 9).

[44] A. Comby. „Real-Time determination of enantiomeric and isomeric content using photoelectron elliptical dichroism.“ In: *Nature Communications* 9 (2018) (cit. on p. 9).

[45] Volker Ulrich. „Giant Chiral Asymmetry in the C 1s Core Level Phooemission from Randomly Oriented Fenchone Enantiomers.“ In: *J. Phys. Chem. A* 112 (2008) (cit. on p. 9).

[46] Martin Pitzer. „How to determine the handedness of single molecules using Coulomb explosion imaging.“ In: *Journal of Physics B: Atomic, Molecular and Optical Physics* 50 (2017) (cit. on p. 10).

[47] R. Dörner et al. „Cold Target Recoil Ion Momentum Spectroscopy: a momentum microscope.“ In: *Physics Reports* 330.2-3 (2000) (cit. on p. 14).

[48] T. Jahnke et al. „Vibrationally Resolved K-shell Photoionization of CO with Circularly Polarized Light.“ In: *Phys. Rev. Lett.* 93.8 (2004) (cit. on p. 14).

[49] Sven Grundmann. „Observation of Photoion Backward Emission in Photoionization of He and $N2$.“ In: *Phys. Rev. Lett.* 124.23 (2020) (cit. on p. 14).

[50] M. Spanner et al. „Coulomb asymmetry and sub-cycle electron dynamics in multiphoton multiple ionization of $H2$.“ In: *Journal of Physics B: Atomic, Molecular and Optical Physics* 45.19 (2012) (cit. on p. 14).

[51] Kilian Fehre et al. „Enantioselective fragmentation of an achiral molecule in a strong laser field.“ In: *Science Advances* 5 (2019) (cit. on pp. 14, 45, 50, 52, 64, 67, 68).

[52] G. Kastirke. „Nageregt und Abgefragt: Molekuele im Reaktionsmikroskop.“ PhD thesis. Goethe University of Frankfurt, 2020 (cit. on p. 15).

[53] John David Jackson. *Classical Electrodynamics*. Vol. 14. WILEY, 1998, p. 665 (cit. on p. 18).

[54] J. Viefhaus et al. „The Variable Polarization XUV Beamline P04 at PETRA III : Optics, mechanics and their performance.“ In: *Nucl. Instrum. Methods Phys. Res. A* 710 (2013) (cit. on p. 18).

[55] S. Lidia and R. Carr. „An Elliptically-Polarizing Undulator with Phase Adjustable Energy and Polarization.“ In: *Nucl. Instrum. Methods Phys. Res. A* 347 (1994) (cit. on p. 18).

[56] Till Jahnke. „Interatomic Coulombic Decay.“ PhD thesis. Goethe University of Frankfurt, 2005 (cit. on p. 19).

[57] Sven Grundmann. „Observation of the quadrupole contribution to photo-double-ionization of helium.“ MA thesis. Goethe University of Frankfurt, 2018 (cit. on p. 19).

[58] W. C. Wiley and I. H. McLaren. „Time-of-Flight Mass Spectrometer with Improved Resolution.“ In: *Rev. Sci. Instrum* 26 (1955) (cit. on p. 21).

[59] O. Jagutzki et al. „A broad-application microchannel-plate detector system for advanced particle or photon detection tasks: large are imaging, precise multi-hit timing information and high detecton rate.“ In: *Nucl. Instrum. Methods Phys. Res. A* 477.244-249 (2002) (cit. on pp. 21, 22).

[60] J. L. Wiza. „Microchannel plate detectors.“ In: *Nucl . Instrum. Meth* 162 (1979) (cit. on p. 21).

[61] O. Jagutzki et al. „Multiple hit readout of a microchannel plate detector with a three-layer delay-line anode.“ In: *IEEE Transactions on Nuclear Science* 49 (2002) (cit. on pp. 22, 27).

[62] Sven Grundmann. „Nondipolar photoionization of atoms and molecules.“ PhD thesis. Johann Wolfgang Goethe-University in Frankfurt am Main, 2022 (cit. on p. 22).

[63] RoentDek Handels GmbH. *CoboldPC User Manual*. 5th ed. RoentDek Handels GmbH. 2002 (cit. on p. 22).

[64] RoentDek Handels GmbH. *The RoentDek Constant Fraction Discriminators CFD8c, CFD7x, CFD4c, CFD1c and CFD1x*. RoentDek Handels GmbH. Im Vogelshaag 8 D-65779 Kelkheim-Ruppertshain Germany (cit. on p. 22).

[65] Markus S. Schöffler. „Grundzustandskorrelationen und dynamische Prozesse untersucht in Ion-Helium-Stoessen.“ PhD thesis. Frankfurt am Main: Fachbereich Physik der Johann Wolfgang Goethe-Universität, 2006 (cit. on p. 29).

[66] S. K. Semenov et al. „Auger decay of $1\sigma_g$ and $1\sigma_u$ hole states of the N_2 molecule: Disentangling decay routes from coincidence measurements.“ In: *Physical Review A* 81.4 (2010). DOI: `https://doi.org/10.1103/PhysRevA.81.043426` (cit. on p. 34).

[67] Till Jahnke et al. „Multicoincidence studies of photo and Auger electrons from fixed-in-space molecules using the COLTRIMS technique.“ In: *J. Electron Spectrosc. Relat. Phenom.* 141.2-3 (2004), pp. 229–238 (cit. on p. 33).

[68] Till Jahnke et al. „Circular dichroism in K-shell ionization from fixed-in-space *CO* and *N2* molecules.“ In: *Phys. Rev. Lett.* 88.7 (2002) (cit. on p. 33).

[69] I. Ishii and A. P. Hitchcock. „A quantitative experimental study of the core excited electronic states of formamide, formic acid and formyl fluoride.“ In: *The Journal of Chemical Physics* 87.2 (1987) (cit. on pp. 44, 49).

[70] C. Fridh. „Electronic Excitation of Formic Acid.“ In: *J. Chem. Soc. Faraday Trans.* 74.190-193 (1978) (cit. on p. 44).

[71] S. Bell T. L. Ng. „The $\pi\star \leftarrow$ n transition of formic acid.“ In: *J. Mol. Spectrosc.* 50.1 (1974), pp. 166–181. DOI: `https://doi.org/10.1016/0022-2852(74)90225-2` (cit. on p. 44).

[72] L. M. Beaty-Travis et al. „A conformational study of the S1(n,π∗) excited state of the formic acid.“ In: *J. Chem. Phys* 117.4831-4838 (2002) (cit. on pp. 44, 50).

[73] M. Pitzer et al. „Coulomb explosion imaging as a tool to distinguish stereoisomers.“ In: *J. Vis. Exp.* 126 (2017) (cit. on p. 44).

[74] M. Pitzer et al. „Direct determination of absolute molecular stereochemistry in gas phase by Coulomb explosion imaging.“ In: *Science* 341.1096-1100 (2013) (cit. on p. 44).

[75] Guerra A. C. O et al. „Ionic fragmentation of C 1s excited and ionized formic acid.“ In: *Chemical Physics* 326.2-3 (2006), pp. 589–599 (cit. on pp. 49, 60).

[76] T. Kitamura et al. „Direct observation of dynamic chirality by Coulomb explosion imaging.“ In: *The Journal of Chemical Physics* 115.1 (2001). DOI: `https://doi.org/10.1063/1.1383793` (cit. on p. 57).

[77] G. Kastirke et al. „Double Core-Hole Generation in O_2 Molecules using an X-Ray Free-Electron Laser: Molecular-Frame Photoelectron Angular Distributions.“ In: *Phys. Rev. Lett.* 125.163201 (2020). DOI: `https://doi.org/10.1103/PhysRevLett.125.163201` (cit. on p. 87).

[78] G. Kastirke et al. „Investigating charge-up and fragmentation dynamics of oxygen molecules after interaction with strong X-ray free-electron laser pulses.“ In: *PCCP - Physical Chemistry Chemical Physics* 24.27121 (2022), pp. 27121–27127. DOI: `10.1039/d2cp02408j` (cit. on p. 87).

[79] G. Kastirke. „Photoelectron Diffraction Imaging of a Molecular Breakup Using an X-Ray Free-Electron Laser.“ In: *Phys. Rev. X* 10.021052 (2020). DOI: `10.1103/PhysRevX.10.021052` (cit. on pp. 87, 125).

[80] Eite Tiesinga et al. „CODATA recommended values of the fundamental physical constants.“ In: *Rev. Mod. Phys.* 93 (2021) (cit. on p. 128).

DEUTSCHE ZUSAMMENFASSUNG

Diese Dissertation widmet sich dem Thema Chiralität, Enantiomere, Anregung von Elektronen der inneren Schalen und Photoionisation. Die Arbeit beleuchtet die Wechselwirkungen und Auswirkungen dieser Phänomene auf molekulare Strukturen. Die Erforschung der Photoionisation beziehungsweise der Anregung und ihres Zusammenspiels mit der Chiralität hat zu bahnbrechenden Erkenntnissen geführt. Weiter wurden die Winkelverteilungen von K-Schalen Photoelektronen von Ameisensäure, Sauerstoff und Isopropanol in einem molekülfesten Bezugssystem untersucht.

Das Hauptaugenmerk dieser Dissertation ist es herauszufinden, inwiefern ein achirales Molekül wie Ameisensäure (HCOOH), das planar und ohne chirales Zentrum ist, unter speziellen Bedingungen zwei Enantiomere erzeugen kann. Deshalb wurden zwei verschiedene Arten von Experimenten durchgeführt. Das erste Experiment von Ameinsensäure konzentrierte sich auf die die Anregung des Moleküls in die Zustände π^* und σ^*. Anschließend zerfällt das Molekül. Aus den Zerfallsprodukten der Reaktion lässt sich die absolute Konfiguration des Moleküls zum Zerfallszeitpunkt bestimmen. Dieses Verfahren ist in der Literatur als *Coulomb Explosion Imaging* (CEI) bekannt. Im zweiten Experiment mit Ameisensäure wurde das Molekül direkt photoionisiert. Die Winkelverteilung im molekülfesten System gibt ebenfalls Aufschluß darüber ob das Molekül chirale Eigenschaften zum Zeitpunkt der Ionisation hatte. Anders als im ersten Experiment jedoch wird hier der Chiralitätsgrad des Moleküls im Grundzustand abgefragt. Es stellt sich heraus, dass Ameisensäure selbst im Grundzustand chirale Eigenschaften hat. Dass heißt, dass der Grundzustand nur im Mittel planar ist.

Letzteres Experiment zu Ameisensäure erfordert, dass man Emissionswinkelverteilungen von Photoelektronen aus inneren Schalen in einem molekülfesten System bestimmen kann. Dadurch motiviert wurden im Rahmen dieser Arbeit zwei explorative Experimente durchgeführt, um zu untersuchen, inwiefern die verwendeten Techniken in der Lage sind, Elektron- und Moleküldynamik zu untersuchen. Zum einen wurde Sauerstoff, ein diatomares Molekül, zum anderen Isopropanol [$(CH_3)_2CHOH$] untersucht.

Kapitel 2 dieser Arbeit stellt die theoretischen Grundlagen von Chiralität vor. Dies beinhaltet insbesondere den chiralen Dichroismus (CD) und den photoelektrischen circularen Dichroismus (englisch *Photoelectron Circular Dichroism*, PECD). Außerdem wird vorgestellt, wie man die absolute Konfiguration polyatomarer Moleküle bestimmen kann.

Alle erwähnten Experimente wurden mittels der COLTRIMS-Experimentiertechnik durchgeführt. Insbesondere wurde der permante Aufbau des P04-Strahlrohres vom PETRA III Synchrotron am DESY, Hamburg, genutzt. In Kapitel 3 dieser Arbeit wird die COLTRIMS-Technik eingeführt. Dies beinhaltet das verwendete Gas-System zur Erzeugung eines Überschall-Gasjets, das Spektrometer welches die Impulse der geladenen Reaktionsteilchen abdeckt, das orts- und zeitauflösende Detektorsystem, sowie die Elektronik zur Datenaufnahme. Für alle im Rahmen dieser Arbeit durchgeführten Experimente wurde Synchrotronstrahlung verwendet. Die Prinzipien dieser wird ebenfalls in Kapitel 3 vorgestellt.

Im Kapitel 4 sind die experimentellen Parameter der verschiedenen Experimente aufgelistet. Kapitel 5 behandelt die Datenanalyse und Kalibration.

Drei getrennte Kapitel beinhalten die Ergebnisse der Forschung. Kapitel 6 umfasst die Hauptarbeit und diskutiert die Untersuchung des Ameisensäure-Moleküls. Kapitel 7 präsentiert die Ergebnisse der Experimente am zweiatomigen, homonuclearen Molekül Sauerstoff. In Kapitel 8 wird die Methodik aus Kapitel 7 auf das mehratomiges Molekül Isopropanol übertragen.

Wie einleitend erwähnt, wurden zwei Experimente an Ameisensäure durchgeführt. Im ersten Experiment wird eine Photonenergie gewählt, die knapp unter der Ionisationsschwelle von Ameisensäure liegt. Dadurch wird das Molekül nicht direkt photoionisiert sondern zunächst angeregt. Das Photon war hierbei links- bzw. rechts-zirkular polarisiert. Diese Art von Spektrometrie (das Anregen von Innerschalen-Elektronen zur Untersuchung von Materie) ist angelehnt an die in der Literatur bekannte NEXFAS-Spektrometrie (aus dem englischen *X-ray absorption near edge structure* NEXAFS, zu deutsch etwa Röntgen-Nahkanten-Absorptions-Spektroskopie). Konkret wurden im Rahmen dieser die Anregungszustände π^* und σ^* untersucht. Die optimale Energie zur Anregung in diese Zustände wurde durch manuelles durchfahren der Photonenergie bestimmt. Nach der Anregung fragmentiert das Molekül in mehrere geladene Bruchstücke. Aufgrund der gleichen Ladung stoßen sich die Bruchstücke ab und es kommt zu einer Coulomb-Explosion. Anhand der finalen Impulse, die aus dieser Coulomb-Explosion entstehen, lässt sich die absoulte Konfiguration des Moleküls zum Fragmentationszeitpunkt bestimmen (diese Technik wird im englischen *Coulomb Explosion Imaging*, CEI, genannt).

Aus den Impulsen der Molekülfragmente lässt sich ein Maß für den Chiralitätsgrad des Moleküls definieren:

$$cos(\alpha) = (\vec{O}2 \times \vec{C}) \cdot \vec{H}2/(|\vec{O}2 \times \vec{C}| \cdot |\vec{H}2|) \tag{A.1}$$

(Für eine Definition der einzelnen Impulsvektoren, siehe Seite 44.) Eine Abweichung von $cos(\alpha)$ von Null bedeutet, dass das Molekül zum Fragmentationszeitpunkt eine chirale Struktur aufwies. Von den beiden untersuchten Anregungszuständen, $\pi^\star$ und $\sigma^\star$, weißt einer chirale Strukturen auf ($\pi^\star$), der andere nicht ($\sigma^\star$).

Die experimentellen Daten wurden mit Berechnungen der Theoriegruppe von Philipp Demekhin (Kassel) verglichen. Die experimentellen Daten haben eine gute Übereinstimmung mit der Theorie. Die theoretische Beschreibung basiert auf den Wellenfunktionen des Grundzustandes sowie der Anregungszustände $\pi^\star$ und $\sigma^\star$. Der angeregte $\pi^\star$ Zustand weißt ein Potential mit zwei Minima auf, d.h., es existiert ein Gleichgewichtszustand für links- und rechtshändige Konfigurationen. Das Übergangsmatrixelement $M(R, \vartheta, \phi)$ für den Übergang vom Grundzustand in den angeregten Zustand hängt der Richtung der Lichtpolarisation im molekularem Bezugssystem ab, d.h. unter welchem Winkeln ϑ und ϕ das Licht auf das Molekül trifft. Da $M(R, \vartheta, \phi)$ für positive und negative R unterschiedlich sein muss, ergeben sich die beobachteten links- und rechtshändigen pyramidalisierten Konfigurationen.

Das zweite Experiment mit Ameisensäure untersucht diese mittels direkter Photoionisation. Anhand molekülfester Emissionswinkelverteilungen des Photoelektrons (englisch *molecular frame photoelectron angular distributions*, MFPAD) lässt sich ein Abbild der molekularen Struktur zum Zeitpunkt der Photoabsorption bestimmen. Das Molekül wurde sozusagen mit dem Elektron von "innen-heraus" beleuchtet. Wenige Femtosekunden nachdem ein Innerschalen-Photoelektron emittiert wird kommt es zu einer Auger-Kaskade, wodurch es zu einer molekularen Fragmentation kommt. CEI ermöglicht dementsprechend erneut, Aufschluss auf die molekulare Konfiguration, jedoch zu einem verzögerten Zeitpunkt (nämlich nachdem es zum Auger-Zerfall kam), zu erhalten. Es zeigt sich, dass die Händigkeit dieser beiden Schnappschüsse (einer gegeben über das MFPADs, der andere durch die Coulomb-Explosion) identisch ist. Die Händigkeit (Chiralität) des Moleküls existierte schon zum Zeitpunkt der Photoabsorption und war dementsprechend schon eine Eigenschaft des Grundzustandes von Ameisensäure und das diese Händigkeit auf Femtosekunden-Zeitskalen bestehen bleibt.

Das zweite Experiment mit Ameisensäure basiert darauf, Photoelektronenemissionswinkel in molekülfesten Bezugssystemen zu bestimmen. Dafür ist es notwendig (a) ein Photoelektron welches das molekulare Potential abbildet und (b) einen molekularen Aufbruch, welcher ein hinreichend gutes molekülfestes Bezugssystem definiert, zu erzeugen. Nach K- Schalen-Ionisation kommt es generell zu einer Auger-Kaskade welche häufig in einen molekularen Aufbruch nach sich zieht. Weiter kann es zur Ein-Photon Doppelionisation kommen, in denen ein Photon zwei Elektronen auslöst (für hochenergetische Elektronen geschieht dies üblicherweise mittels des sogenannten *Shake-off* Mechanismus). Falls statt Synchrotronstrahlung das

Licht eines Freien-Elektronen-Lasers (FEL) verwendet wird, kann es ebenfalls zu Mehr-Photonen Mehrfachionisation kommen. Im Allgemeinen bedeuten die Anforderungen (a) *und* (b), dass mehrere Elektronen emittiert werden. Es stellt sich die Frage, ob die Existenz mehrer Elektronen (und dementsprechend die Existenz von Elektron-Elektron Korrelationen im Endzustand) die Fähigkeit einschränkt, das Molekülpotential über das Photoelektron abzubilden. Um diese Frage zu beantworten wurde eine Reihe von explorativen Experimenten durchgeführt.

Zum einen wurde die Photoionisation von Sauerstoff, einem diatomaren, homonuclearen Molekül untersucht. Es werden Daten eines Experimentes mit Synchrotronlicht (durchgeführt am P04 Strahlrohr, PETRA III, DESY) sowie eines mit FEL-Strahlung (durchgeführt am XFEL, Hamburg) verglichen. Diese Reihe von Experimenten beleuchtet den Unterschied zwischen Synchrotronstrahlung und FEL-Strahlung anhand einer verhältnismäßig einfachen molekularen Geometrie. Im Rahmen dieser Dissertation war es möglich, direkt die Photoionisation von Sauerstoff durch Synchrotronstrahlung und FEL-Strahlung zu vergleichen, da die gleichen Aufbruchskanäle (O^+/O^+, O^+/O^{++}, O^{++}/O^{++}, O^+/O^{+++}, O^{++}/O^{+++}) untersucht wurden. Aus dem Unterschied der beiden Messungen wird direkt ersichtlich, dass im Falle von FEL-Strahlung höhere Ladung tatsächlich durch Mehrphotonenprozesse enstehen.

Zum anderen wurde die Photoionisation von Isopropanol mittels Synchrotronstrahlung untersucht, um herausfzufinden, inwiefern sich die vorgestellte Technik auf größere Molekülstrukturen anwenden lässt. Es wurden drei Photonenenergien (670 eV, 600 eV und 563 eV) bei zwei Magnetfeldeinstellungen (42 Gs und 14 Gs) gemessen. Die unterschiedlichen Magnetfeldeinstellungen zielen erneut darauf ab, das Spektrometer auf niedrige beziehungsweise auf hohe Elektronenenergien zu optimieren. Bei größeren polyatomaren Molekülen ergibt sich die Schwierigkeit, Aufbruchskanäle erfolgreich zuzuordnen. Es wurden sechs Aufbruchskanäle untersucht.

$$CH_3^+/CH_3^+/CH_2O \tag{A.2}$$
$$CH_3^+/C_2H_3^+/H_2O \tag{A.3}$$
$$O^+/C_3H_5^+/H_3 \tag{A.4}$$
$$CH_2^+/O^+/C_2H_4^+/H_2 \tag{A.5}$$
$$CH_2^+O^+C_2H^+ \tag{A.6}$$
$$H^+O^+C_3^+ \tag{A.7}$$

Zusammenfassend konnte in dieser Arbeit gezeigt werden, dass ein planares, achirales Molekül wie Ameisensäure lediglich gemittelt keine Händigkeit aufweist, während jedoch jedes einzelne Molekül eine chirale Struktur besitzt. Dies wurde über verschiedene Ansätze gezeigt. Es wurde ein Verfahren analog zur NEXAFS-Spektrometrie verwendet, in dem das Molekül zunächst angeregt wird und anschließend durch Abregung auf einen

Coulomb-explodierenden Zustand fällt. Über CEI lässt sich dann die molekulare Konfiguration bestimmen. Außerdem ist es möglich, das molekulare Potential über MFPADs abzubilden. Dabei wurde jeweils die COLTRIMS-Technik verwendet. Um diese Anwendbarkeit dieser beiden Verfahren zu untersuchen, wurden mehrere explorative Experimente an Sauerstoff und Isopropanol durchgeführt.

PUBLICATIONS

Phys. Rev. Res., 5 (2023) 013021
Molecular-frame differential photoelectron circular dichroism of O 1s-photoelectrons of trifluoromethyloxirane
G. Nalin, N. M. Novikovskiy, K. Fehre, N. Anders, D. Trabert, S. Grundmann, M. Kircher, A. Khan, R. Tomar, M. Hofmann, M. Waitz, I. Vela-Perez, G. Kastirke, J. Siebert, D. Tsitsonis, C. Küstner-Wetekam, L. Marder, J. Viehmann, F. Trinter, H. Fukuzawa, K. Ueda, J. B. Williams, A. Knie, R. Dörner, M. S. Schöffler, T. Jahnke, Ph. V. Demekhin

Phys. Rev. Lett., 129 (2022) 253201
Observation of Nondipole-Induced Asymmetry in the Angular Emission Distribution of Photoelectrons from Fixed-in-Space CO Molecules
D.V. Rezvan, K. Klyssek, S. Grundmann, A. Pier, N. M. Novikovskiy, N. Strenger, D. Tsitsonis, M. Kircher, I. Vela-Peréz, K. Fehre, F. Trinter, M. S. Schöffler, T. Jahnke, R. Dörner, Ph. V. Demekhin

Phys. Chem. Chem. Phys., 24 (2022) 13597-13604
Influence of the emission site on the photoelectron circular dichroism in trifluoromethyloxirane
K. Fehre, F. Trinter, N. M. Novikovskiy, S. Grundmann, D. Tsitsonis, S. Eckart, L. Bauer, M. Hilzinger, T. Jahnke, R. Dörner, Ph. V. Demekhin, M. S. Schöffler

Nat. Commun., 12 (2021) 6657
Measuring the photoelectron emission delay in the molecular frame
J. Rist, K. Klyssek, N. M. Novikovskiy, M. Kircher, I. Vela-Perez, D. Trabert, S. Grundmann, D. Tsitsonis, J. Siebert, A. Geyer, N. Melzer, Ch. Schwarz, N. Anders, L. Kaiser, K. Fehre, A. Hartung, S. Eckart, L. Ph. H. Schmidt, M. S. Schöffler, V. T. Davis, J. B. Williams, F. Trinter, R. Dörner, Ph. V. Demekhin, T. Jahnke

Phys. Chem. Chem. Phys., 23 (2021) 17248
Photoelectron circular dichroism of O 1s-photoelectrons of uniaxially oriented trifluoromethyloxirane: energy dependence and sensitivity to molecular configuration
G. Nalin, K. Fehre, F. Trinter, N. M. Novikovskiy, N. Anders, D. Trabert, S. Grundmann, M. Kircher, A. Khan, R. Tomar, M. Hofmann, M. Waitz, I. Vela-Perez, G. Kastirke, J. Siebert, D. Tsitsonis, H. Fukuzawa, K. Ueda, J. B. Williams, D. Kargin, M. Maurer, C. Küstner-Wetekam, L. Marder, J. Viehmann, A. Knie, T. Jahnke, M. Ilchen, R. Dörner, R. Pietschnig, P. V.

Demekhin, M. S. Schöffler

Phys. Rev. Res., 2 (2020) 033209
Chiral photoelectron angular distributions from ionization of achiral atomic and molecular species
A. Pier, K. Fehre, S. Grundmann, I. Vela-Perez, N. Strenger, M Kircher, D. Tsitsonis, J.B. Williams, A. Senftleben, T. Baumert, M. S. Schöffler, P. Demekhin, F. Trinter, T. Jahnke, R. Dörner